The Dissertation Committee for Won Chang Choi certifies that this is the approved version of the following dissertation:

UNDERSTANDING THE CAPACITY FADE MECHANISMS OF SPINEL MANGANESE OXIDE CATHODES AND IMPROVING THEIR PERFORMANCE IN LITHIUM ION BATTERIES

Committee:

Arumugam Manthiram, Supervisor

John B. Goodenough

Harovel G. Wheat

Desiderio Kovar

Keith Stevenson

UNDERSTANDING THE CAPACITY FADE MECHANISMS OF SPINEL MANGANESE OXIDE CATHODES AND IMPROVING THEIR PERFORMANCE IN LITHIUM ION BATTERIES

by

Won Chang Choi, B.S., M.S.

Dissertation

Presented to the Faculty of the Graduate School of

the University of Texas at Austin

in Partial Fulfillment

of the Requirements

for the Degree of

Doctor of Philosophy

The University of Texas at Austin

May 2007

ACKNOWLEDGEMENTS

First of all, I would like to sincerely thank my supervisor, Professor Arumugam Manthiram, for his valuable guidance and continuous support through my research. I also thank my committee members, Drs. John B. Goodenough, Harovel G. Wheat, Desiderio Kovar, and Keith Stevenson for their helpful advice and review of my work.

I am grateful to the faculty, staff, and graduate students in the Materials Science and Engineering Program. Especially, I would like to appreciate all the past and present members in Prof. Manthiram group and all my Korean friends in Austin. It was a great pleasure to work and be with them. I also thank the Department of Energy for financial support.

Finally, I am so much obliged to my parents, brother, and fiancé, Joo Youn. Without them, it would not have been possible for me to finish my work successfully.

UNDERSTANDING THE CAPACITY FADE MECHANISMS OF SPINEL MANGANESE OXIDE CATHODES AND IMPROVING THEIR PERFORMANCE IN LITHIUM ION BATTERIES

Publication No. _______________

Won Chang Choi, Ph.D.

The University of Texas at Austin, 2007

Supervisor: Arumugam Manthiram

Lithium ion batteries have been successful in portable electronics market due to their high energy density, adopting the layered $LiCoO_2$ as the cathode material in commercial lithium ion cells. However, increasing interest in lithium ion batteries for electric vehicle and hybrid electric vehicle applications requires alternative cathode materials due to the high cost, toxicity, and limited power capability of the layered $LiCoO_2$ cathode. In this regard, spinel $LiMn_2O_4$ has become appealing as manganese is inexpensive and environmentally benign, but $LiMn_2O_4$ is plagued by severe capacity fade at elevated temperatures. This dissertation explores the factors that control and limit the electrochemical performance of spinel $LiMn_2O_4$ cathodes and focuses on improving the performance parameters such as the capacity, cyclability, and rate capability of various spinel cathodes derived from $LiMn_2O_4$.

From a systematic investigation of a number of cationic and anionic (fluorine) substituted spinel oxide compositions, the improvements in electrochemical properties and performances are found to be due to the reduced manganese dissolution and suppressed lattice parameter difference between the two cubic phases formed during the charge-discharge process.

Investigations focused on fluorine substitution reveal that spinel $LiMn_{2-y-z}Li_yZn_zO_{4-\eta}F_\eta$ oxyfluoride cathodes synthesized by solid-state reactions at 800 ^oC employing ZnF_2 as a raw material and spinel $LiMn_{2-y-z}Li_yNi_zO_{4-\eta}F_\eta$ oxyfluoride cathodes synthesized by firing the cation-substituted $LiMn_{2-y-z}Li_yNi_zO_4$ oxides with NH_4HF_2 at a moderate temperature of 450 ^oC show superior cyclability, increased capacity, reduced Mn dissolution, and excellent storage performance compared to the corresponding oxide analogs and the conventional $LiMn_2O_4$.

Spinel-layered composite cathodes are found to exhibit better electrochemical performance with graphite anode when charged to 4.7 V in the first cycle followed by cycling at 4.3–3.5 V compared to the normal cycling at 4.3 – 3.5 V. The improved performance is explained to be due to the trapping of trace amounts of protons that may be present in the electrolyte within the layered oxide lattice during the first charge to 4.7 V and the consequent reduction in Mn dissolution.

Electrochemical performances of 3 V spinel $Li_4Mn_5O_{12}$ cathodes are also improved by fluorine substitution due to the suppression of the disproportionation of $Li_4Mn_5O_{12}$ during synthesis and the formation of the Li_2MnO_3 phase.

TABLE OF CONTENTS

CHAPTER 1 *INTRODUCTION* 1

CHAPTER 2 *GENERAL EXPERIMENTAL TECHNIQUES* 28

CHAPTER 3 *FACTORS CONTROLLING THE ELECTROCHEMICAL PERFORMANCES OF 4 V SPINEL CATHODES* 34

LIST OF TABLES

LIST OF FIGURES

CHAPTER 1

INTRODUCTION

1.1 BATTERIES

A battery is defined as an electrochemical device that stores chemical energy and releases it in the form of electrical energy when needed. Batteries can be classified as primary batteries and secondary batteries based on the reversibility of the chemical reactions involved. While the reaction in a secondary battery is reversible, that in a primary battery is irreversible.[1,2]

1.1.1 Primary Batteries

The first true battery was invented by Alessandro Volta in 1800, which is known as a Voltaic Pile.[1] The Voltaic Pile included a pair of copper and zinc discs as well as a layer of cloth soaked in brine. Various systems such as the Daniell cell, Grove cell, Gravity cell, Leclanché, and zinc-carbon cell were then developed by the end of the 19th century. Practically, lithium manganese dioxide battery, alkaline battery, lithium primary battery, and zinc-air battery have been designed and commercialized,[2] and the cell components of primary batteries are shown in Table 1.1.

Table 1.1 Cell components of primary batteries.[2]

System	Anode	Cathode	Electrolyte
Zinc-carbon (Leclanché)	Zn	MnO_2	NH_4Cl and $ZnCl_2$ (aqueous solution)
Zinc-carbon (zinc chloride)	Zn	MnO_2	$ZnCl_2$ (aqueous solution)
Mg/MnO_2	Mg	MnO_2	$MgBr_2$ or $Mg(ClO_4)$ (aqueous solution)
Zn/Alk./MnO_2	Zn	MnO_2	KOH (aqueous solution)
Cd/HgO	Cd	HgO	KOH (aqueous solution)
Zn/Ag_2O		Ag_2O or AgO	KOH or NaOH (aqueous solution)
Zinc/air	Zn	O_2 (air)	KOH (aqueous solution)
Li/SO_2	Li	SO_2	Organic solvent, salt solution
Li/MnO_2	Li	MnO_2	Organic solvent, salt solution

1.1.2 Secondary Batteries

Lead-acid battery was the first rechargeable battery launched by Gaston Planté in 1860.[2] Planté's first model employed two lead sheets separated by rubber strips rolled into a spiral. Since then, lead-acid batteries have been developed and improved over one hundred years, succeeding in automobile and other applications with advantages of high rate and good low-temperature performances.

Alkaline secondary batteries have also been widely used because they contain an aqueous alkaline solution of KOH or NaOH as the electrolyte to give less reactivity between the electrode materials and alkaline electrolytes compared to the acid electrolyte.[2] Various commercialized alkaline batteries exist and some examples are nickel-cadmium batteries, nickel-iron batteries, silver-zinc batteries, and nickel-zinc batteries. The cell components of these batteries are given in Table 1.2. Among them, nickel-cadmium secondary battery is the most popular alkaline secondary battery with a wide range of applications such as in portable home appliances, diesel engine starters, aircrafts, and heavy-duty industrial equipment, despite its memory effect and environmentally harmful cadmium.[3]

In the late 1980's, the nickel metal hydride battery (Ni-MH battery) similar to the nickel-cadmium battery was developed, replacing the cadmium electrode with one made of a hydrogen-absorbing alloy.[4] It has been widely used for consumer electronics and portable devices as it does not suffer from memory effects and offers two or three times higher capacity with less toxic materials compared to the nickel-cadmium battery.

Table 1.2 Cell components of secondary batteries.[2]

System	Anode	Cathode	Electrolyte
Lead-acid	Pb	PbO_2	H_2SO_4 (aqueous solution)
Nickel-cadmium	Cd	NiOOH	KOH (aqueous solution)
Nickel-iron	Fe	NiOOH	KOH (aqueous solution)
Nickel-zinc	Zn	NiOOH	KOH (aqueous solution)
Silver-zinc	Zn	AgO	KOH (aqueous solution)
Silver-cadmium	Cd	AgO	KOH (aqueous solution)
Nickel-hydrogen	H_2	NiOOH	KOH (aqueous solution)
Nickel-metal hydride	Metal hydride	NiOOH	KOH (aqueous solution)
Zn/MnO_2	Zn	MnO_2	KOH (aqueous solution)
Lithium ion battery	C	$LiCoO_2$	Organic solvent

Recently, the Ni-MH battery has been investigated for HEV applications, and the first massive HEV automobiles adopting Ni-MH battery were produced by Toyota (sold in Japan since 1997 and worldwide since 2001).[5] Despite these advantages and commercial application of the Ni-MH battery, the lithium ion battery has been intensively investigated for HEV applications mainly due to the higher volumetric energy density of lithium ion batteries.

In 1991, Sony developed the first commercial lithium ion battery by adopting $LiCoO_2$ as the cathode material and carbon as the anode material.[6,7] The electrochemical extraction (charging) of lithium ions from layered $LiCoO_2$ was first identified by Goodenough's group in the early 1980's,[8] and the lithium insertion into graphite was investigated by Besenhard's group in 1976.[9] The electrochemical insertion of lithium into graphite and its use as an anode solved the safety problems associated with the formation of dendrites on the surface of lithium metal anode as encountered with the previously known MoS_2-Li battery.[10] Since then, extensive research to develop and improve the electrochemical performances in lithium ion batteries have been achieved, but the accomplishments so far are not enough to replace the commercial $LiCoO_2$-carbon lithium ion battery.

1.2 LITHIUM ION BATTERY

1.2.1 Principles of Operation

The lithium ion battery is composed of a cathode, anode, electrolyte, and separator. When the battery is charged, the lithium ions in the cathode material migrate through the separator to the anode with the flow of charging current through the external circuit as shown in Fig. 1.1. In an opposite way, the lithium ions in the anode migrate through the separator to the cathode material with the flow of discharging current through the external circuit. In order to achieve superior performance in lithium ion cells, the cell components have to satisfy several requirements given below.

- Cathode and anode materials should support a high degree of lithium insertion/extraction to maximize the energy density.
- Cathode material should have a low lithium chemical potential and anode material should have a high lithium chemical potential to maximize the cell voltage and thus the energy density.
- Voltage change in the cathode and anode materials during charge-discharge process should be small.
- Lithium diffusion coefficient should be large for high rate charge-discharge performance.
- Electrolyte, cathode, and anode material should be inexpensive and preferably environmentally benign.

Figure 1.2 shows the operating voltage of lithium insertion compounds with respect to lithium metal. Among these electrodes, $LiCoO_2$, $LiMn_2O_4$, and $LiFePO_4$ oxides have become attractive cathode materials, exhibiting a higher electrode potential of 3.5 - 4.0 V versus lithium metal.

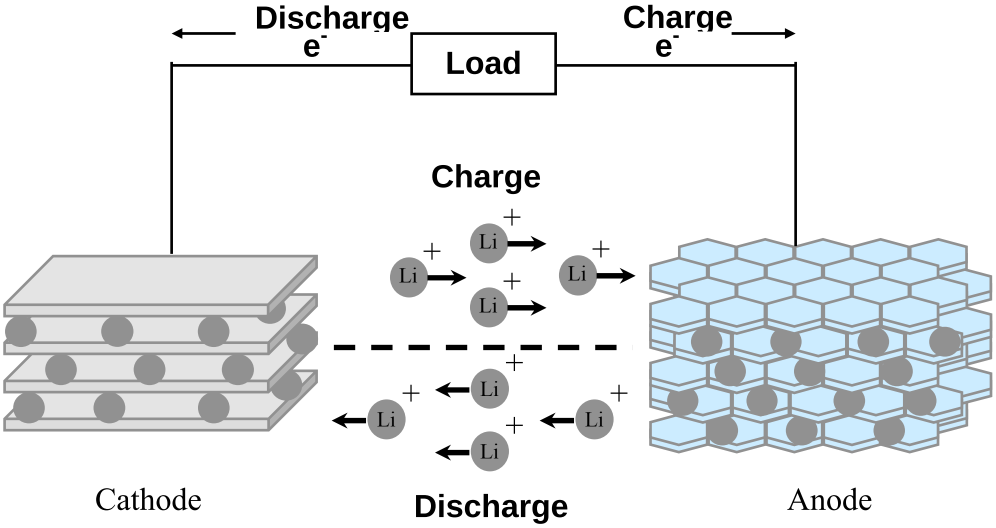

Cathode: $\mathbf{LiCoO_2} \leftrightarrow Li_{1-x}CoO_2 + x\,Li^+ + x\,e^-$
Anode: $\mathbf{C_6} + x\,Li^+ + x\,e^- \leftrightarrow Li_xC_6$

Figure 1.1 Schematic drawing of lithium ion battery during the charge-discharge process. The reactions shown refer to the charging process.

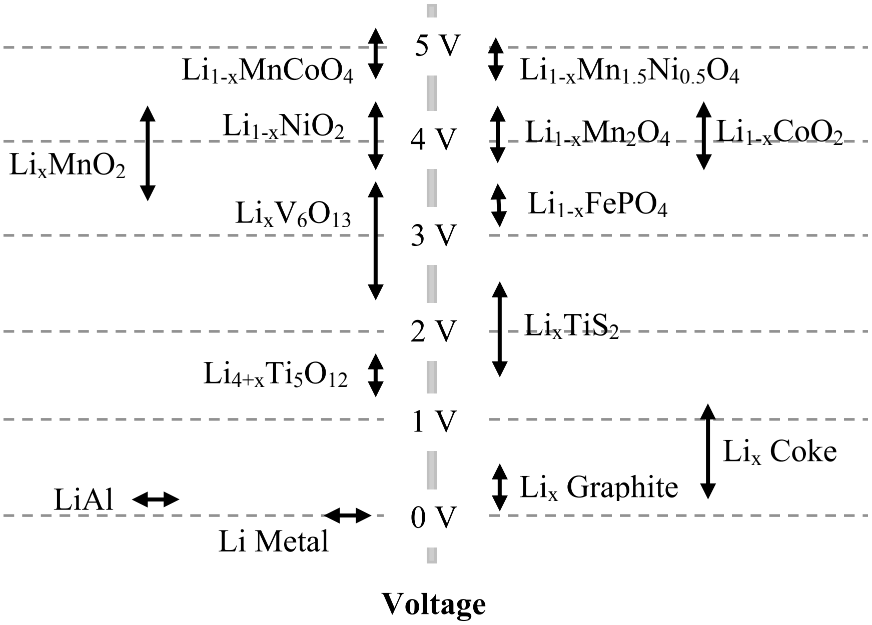

Figure 1.2 Electrochemical potential ranges of lithium insertion compounds with reference to lithium metal.[11,12]

1.2.2 Cell Components of Lithium Ion Battery

A lithium ion battery consists of a cathode, an anode, organic electrolyte, separator, and safety devices, and the schematic diagram of a commercial cylindrical lithium ion battery is shown in Fig. 1.3.

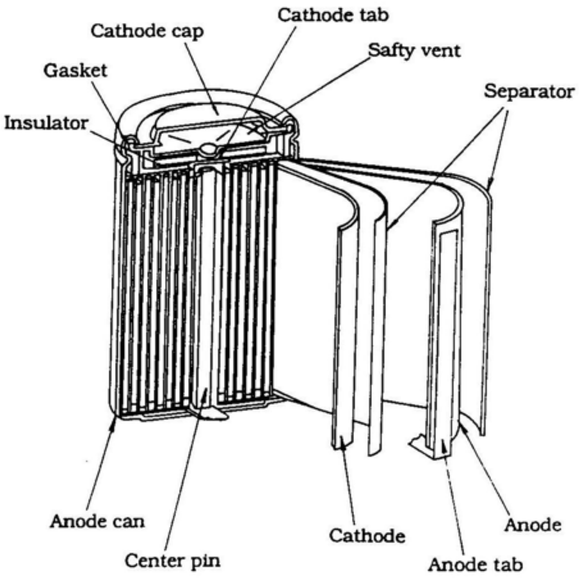

Figure 1.3 Schematic diagram of cylindrical lithium ion battery.[13]

1.2.2.1 Cathode Materials

Layered $LiCoO_2$ is widely used in most commercial lithium ion batteries due to its good cyclability, reasonable capacity, and easy synthesis. However, several issues associated with safety, cost, and the environmental hazard of cobalt have provoked the development of alternate cathodes. Several candidates with different compositions, metal ions, or crystal structures have been extensively investigated. Some examples are layered $LiNiO_2$,[14] $LiNi_{1-y}M_yO_2$ (M = transition metal),[15-22] olivine $LiFePO_4$,[23,24] and spinel $LiMn_2O_4$.[25,26]

Layered structure

Layered structures have the general formula $LiMO_2$ (M = V, Mn, Co, and Ni) in which Li^+ and M^{3+} ions occupy the octahedral sites in the alternate (111) planes of the rock salt lattice formed by a cubic close packing of oxide ions (Fig. 1.4)[1]

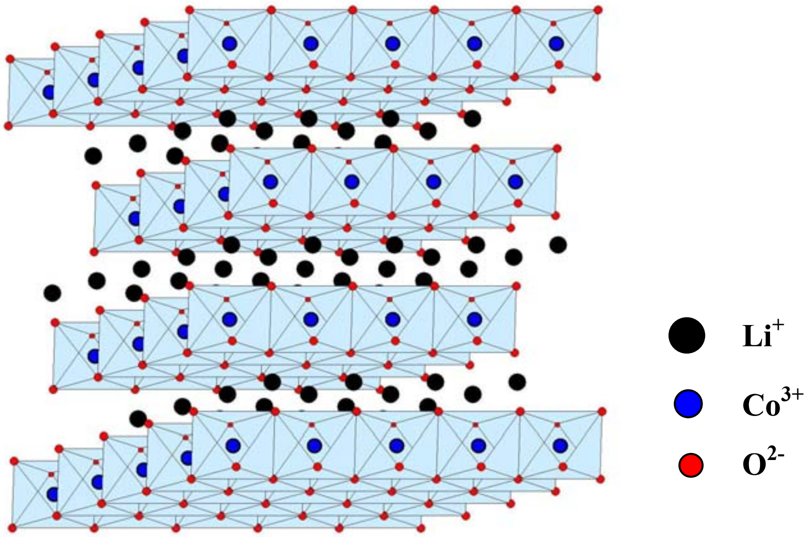

Figure 1.4 Structure of the layered $LiCoO_2$.

A two-dimensional layered crystal structure is formed due to the large ionic radius and charge differences between the Li^+ and M^{3+} ions, resulting in a trigonal symmetry with the space group ($R\bar{3}m$). However, cation disorder between the Li^+ and M^{3+} layers often tends to occur as the size and charge differences derease.[27]

Layered $LiCoO_2$ has well-defined two-dimensional Li^+ ion pathways due to the large difference in ionic radius between Li^+ and Co^{3+} ions and good electronic conductivity due to a direct Co-Co interaction in the edge-shared CoO_6 octahedra. Layered $LiCoO_2$ has been widely used in commercial lithium ion batteries mainly due to easy synthesis, reasonable capacity of around 140 mAh/g, and long cycle life. However, $LiCoO_2$ has some shortcomings such as toxicity, high cost, and limited utilization of the theoretical capacity (~ 50 %) due to the chemical instability at deep lithium extraction associated with the removal of electrons from the O^{2-}:2p band.[28-33]

The layered $LiNiO_2$ having the same structure as $LiCoO_2$ has been widely studied because it has a higher capacity of around 200 mAh/g compared to $LiCoO_2$. Since the location of the $Ni^{3+/4+}$:e_g band is above the O^{2-}:2p band, lithium extraction does not cause a significant removal of electrons from the O^{2-}:2p band, providing a greater utilization of lithium ions in $LiNiO_2$ compared to that in $LiCoO_2$.[31,34] However, $LiNiO_2$ experiences difficulties in synthesizing it as an ordered material, release of oxygen at elevated temperatures, and severe capacity fade originating from irreversible phase transitions during cycling. To improve the cyclability and solve the safety problems of $LiNiO_2$, cation-substituted $LiNi_{1-y}M_yO_2$ (M = Al, Mn, and Co) have been intensively studied.[15-22]

Olivine structure

Iron containing compounds including FeOCl,[35] $FePS_3$,[36] $KFeS_2$,[37] and FeS_2[38] have been pursued for cathode in lithium ion batteries because of the low cost and the non toxicity of Fe. Among these compounds, the olivine $LiFePO_4$ shown in Fig. 1.5

having a theoretical capacity as high as 170 mAh/g, a flat discharge voltage of around 3.4 V, and excellent safety characteristics has become attractive for commercial viability.[23] However, the olivine structure suffers from low electronic conductivity and lithium ion conductivity. To overcome this problem, coating with carbon or conducting polymer as well as making the powder in nanocrystalline form have been adopted.[39-41]

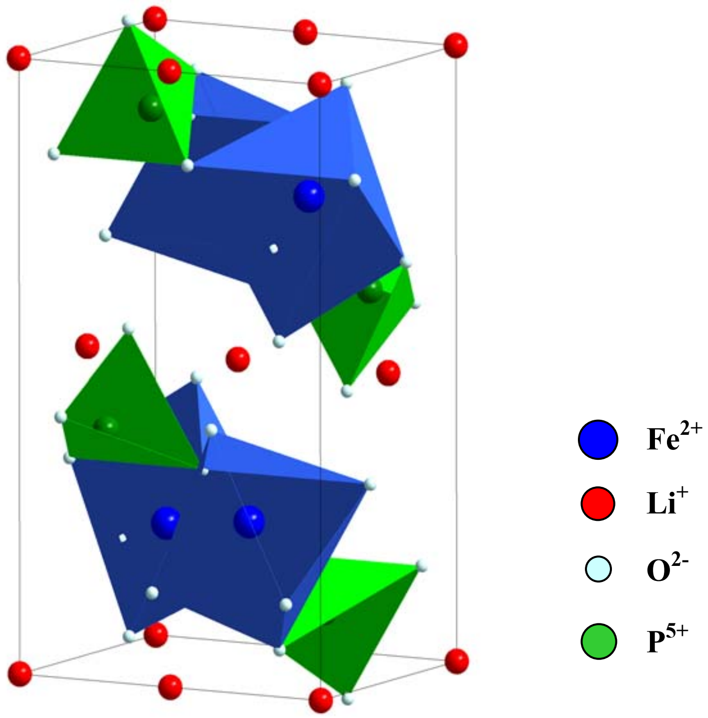

Figure 1.5 Structure of the olivine $LiFePO_4$.

Spinel structure

Electrochemical charging/discharging of spinel $LiMn_2O_4$ was first reported by Thackeray *et al.*[25] Since then, the spinel $LiMn_2O_4$ containing inexpensive and environmentally benign Mn has been studied extensively as a candidate material for the cathode in lithium ion batteries. However, spinel $LiMn_2O_4$ suffers from severe capacity fade, especially at elevated temperatures, and delivers a slightly lower capacity of around 120 mAh/g. Despite these problems, the inexpensive, nontoxic, and thermally stable $LiMn_2O_4$ has been appealing for HEV applications. The spinel $LiMn_2O_4$ cathodes are the topic of my dissertation and will be discussed in detail later.

1.2.2.2 Anode Materials

Carbon materials have been adopted as the anode in commercial lithium ion batteries because of their abundance, light weight, and safety compared to lithium metal. However, carbon materials lead to a significant irreversible capacity in initial cycles. This irreversible capacity in the first cycle is generally attributed to solid electrolyte interfacial (SEI) layer formation and side reactions of LiC_6.[1] In an effort to improve the electrochemical properties of carbon, structural modifications, texture control, surface modification by mild oxidation and incorporation of other elements have been investigated.[42] Other alternative anode materials such as $Li_4Ti_5O_{12}$,[43,44] tin oxides,[45] and metal alloys[46-49] have also been pursued (Table 1.3). However, the higher potential of $Li_4Ti_5O_{12}$ at around 1.5 V vs. lithium, the significant irreversible capacity of SnO_2, and the huge volume change of metal alloys are major issues to replace carbon materials by these anodes. Recently, Sony has adopted tin-based nanoparticles as the anode in lithium ion cells, delivering a much higher volumetric energy density than a carbon anode.[50]

Table 1.3 Anode materials of lithium ion batteries.[51]

Material	Lithiated anode material	Theoretical capacity (mAh/g)
Graphite	LiC_6	372
Coke	$Li_{0.5}C_6$	185
$Li_4Ti_5O_{12}$	$Li_7Ti_5O_{12}$	160
Al	LiAl	800
Sn	$Li_{4.4}Sn$	790
SnO	$Li_{4.4}Sn/Li_2O$	658
SnO_2	$Li_{4.4}Sn/Li_2O$	564
Sn_2Fe	$Li_{4.4}Sn/Fe$	666

1.2.2.3 Electrolytes

The lithium ion battery employs non-aqueous electrolytes because the working voltage of lithium ion cells requires a wider electrochemical stability window than that of water. The non-aqueous electrolytes should have high conductivity over a wide temperature range, a large electrochemical window of more than 4.5 V, low vapor pressure, low temperature coefficient of viscosity, low toxicity, and low cost for use in practical lithium ion batteries.

The ionic conductivity of the electrolytes in lithium ion batteries depends on the number of ionic carriers and on their mobility. Because the number of ionic carriers and mobility is related to the dielectric constant and viscosity of the solvent in the electrolyte, selection of the solvent plays an important role in the electrochemical performance of the battery,[1] and the physical properties of major solvents are given in Table 1.4. Ethylene carbonate (EC) based electrolytes containing $LiPF_6$ are stable over 5 V and widely used in lithium ion batteries. In many cases, EC is mixed with low viscosity solvents such as dimethyl carbonate (DMC) and diethyl carbonate (DEC) because EC exists as a solid at room temperature and is viscous.

1.2.2.4 Separators

In batteries, the separator is used to prevent direct electronic contact and allow ion transport between the cathode and anode.[1,2] Because of the low ionic conductivity arising from organic electrolytes, the separator in lithium ion batteries should satisfy several requirements such as micrometer-scale thickness, good mechanical strength after cell fabrication, and chemical and electrochemical stability against the electrolyte. Additionally, the separator in a lithium ion battery could also act as an important safety device by melting down and preventing the huge current flow in case of a external short circuit, overcharging, and overdischarging beyond the operating voltage. For those reasons, polyethylene (PE) or polypropylene (PP) films have been adopted as separators in commercial lithium ion batteries.

Table 1.4 Physical properties of solvents for lithium ion batteries.[1]

Solvent	Acronym	Melting point (°C)	Boiling point (°C)	Relative dielectric constant	Viscosity (cP)	Density (g/cm^3)
Diethyl carbonate	DEC	-43.0	126.8	2.806	0.753	0.970
Dimethoxyethane	DME	-58.0	84.5	7.075	0.407	0.861
Dimethyl carbonate	DMC	4.6	90	3.108	0.590	1.063
Ethylene carbonate	EC	36.5	238	90.36	1.9	1.321
Ethyl methyl carbonate	EMC			2.4	0.65	1.007
Dimethyl sulfoxide	DMSO	18.5	189	46.5	1.99	1.096
1,3-Dioxolane	DIOX	-97.2	76.5		0.6	1.065
2-methyltetrahydrofuran	2-Me-THF	-137.2	79.9	6.75		0.854
Sulfolane	TMS, SL	28.5	287.3	43.30	10.287	1.262

1.2.2.5 Safety Devices

Although the lithium ion battery is more stable than a conventional lithium battery having lithium metal as the anode, safety issues are still important due to the volatile organic electrolyte and the highly oxidized cathodes.[2,52] To prevent short circuit and thermal runway from excessive charging or discharging current, several built-in safety devices such as safety vent, a positive thermal coefficient (PTC) element, and external circuits are included in lithium ion batteries, increasing the cost of the battery. The role of safety vent is to disconnect the charging current by tearing itself off when unexpected internal gas pressure due to any excessive overcharging occurs inside the cell. PTC is a device that is controlled by temperature. When the battery temperature exceeds normal condition, the resistance of the PTC increases and prevents the current flow.

1.3 SPINEL LITHIUM MANGANESE OXIDES AS CATHODE MATERIALS

Since the layered $LiCoO_2$ cathode shows good capacity retention with a high reversible capacity of 140 mAh/g, most portable electronic devices have adopted $LiCoO_2$ as a cathode despite its high cost and toxicity. However, the requirements of hybrid electric vehicles (HEV) and electric vehicles (EV) could not be satisfied with the $LiCoO_2$ cathode, as they need low cost cathode materials with high rate (power) performance. In this regard, spinel $LiMn_2O_4$ has become appealing due to the inexpensive manganese and three dimensional lithium ion paths in the spinel structure.

Table 1.5 shows the requirements of a battery for HEV and 42 V vehicle systems. Although the nickel-metal hydride batteries are currently employed in most of the HEVs, intense research is being carried out to develop cathode materials for lithium ion batteries of interest for EV and HEV applications. In 2000, lithium ion batteries containing $LiMn_2O_4$ cathodes (Shin-Kobe Electric Machinery company) were employed for pilot production of vehicles in Nissan (Fig. 1.6), suggesting the feasibility of a lithium ion battery for EV and HEV applications.

Table 1.5 Energy storage targets for 42 V systems in HEV.[53]

Characteristics	Commercialization goals	
	Mild HEV	Power assist HEV
Discharge pulse power (kW)	13 (for 2 seconds)	18 (for 10 seconds)
Regenerative pulse power (kW)	8 (for 2 seconds)	18 (for 2 seconds)
Engine-off accessory load (kW)	3 for 5 minutes	3 for 5 minutes
Available energy (Wh @ 3 kW)	300	700
Recharge rate (kW)	2.6 kW	4.5 kW
Energy efficiency on load profile (%)	90	90
Cycle life, profiles	150 k	150 k
Cycle life and efficiency load profile	Partial power assist	Full power assist
Cold cranking power @ -30 °C	8 (21 V minimum)	8 (21 V minimum)
Calendar life (years)	15	15
Maximum system weight (kg)	25	35
Maximum system volume (liters)	20	28
Self discharge (Wh/day)	< 20	< 20
Maximum operating voltage (V dc)	48	48
Maximum open circuit voltage (V dc)	48 (after 1 sec.)	48 (after 1 sec.)
Minimum operating voltage (V dc)	27	27
Operating temperature range (°C)	-30 to 52	-30 to 52
Selling price ($/system @ 100-k units)	260	360

Cell specifications
Nominal voltage: 3.6 V
Rated capacity: 3.6 Ah
Dimensions: cylindrical 40D×108H (mm)
Weight: 300 g

Module specifications
Battery construction: 48 cylindrical cells in series
Nominal voltage: 170 V
Dimensions: 260W×540L×160H (mm)
Rated output power: 12.5 kW
Rated input power: 8 kW

Figure 1.6 Commercial lithium ion battery for HEV application.[54]

1.3.1 Spinel Structure

In the spinel $LiMn_2O_4$ structure, lithium ions occupy the 8a tetrahedral sites while manganese ions occupy the 16d octahedral sites of the cubic close-packed oxygen array, filling 1/8 of the tetrahedral sites with lithium ions and 1/2 of the octahedral sites with manganese ions as shown in Fig. 1.7. Spinel $LiMn_2O_4$ provides good lithium ion mobility and high rate capability because of the three dimensional lithium pathway through unoccupied 16c octahedral sites. Additionally, edge-shared MnO_6 octahedra with direct Mn-Mn interactions provide good electrical conductivity.[1]

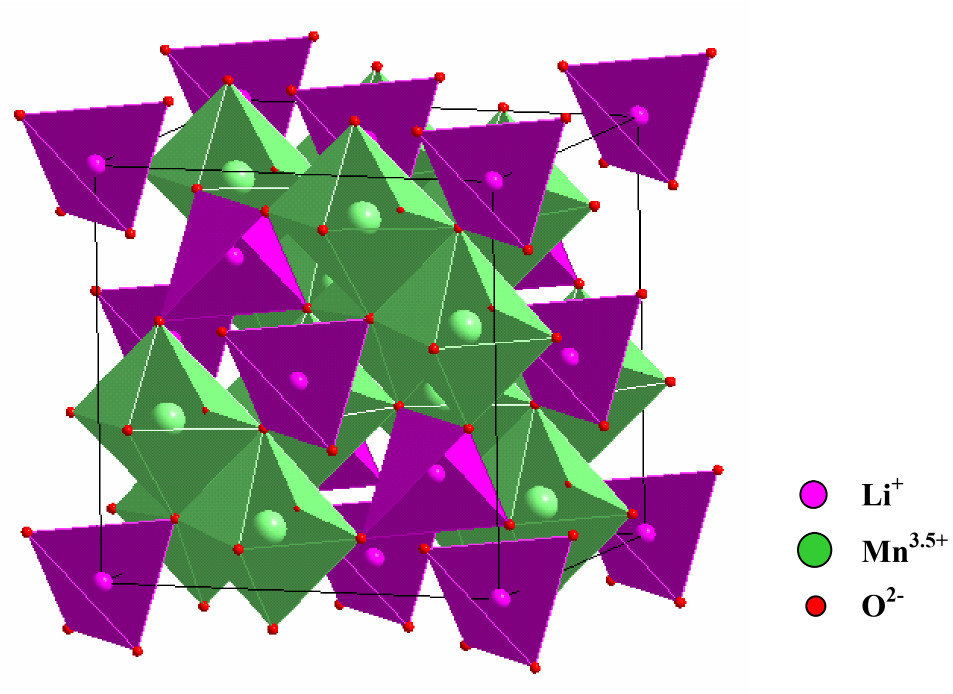

Figure 1.7 Structure of spinel $LiMn_2O_4$.

1.3.2 Spinel $LiMn_2O_4$

Spinel $LiMn_2O_4$ exhibits two distinct voltage plateaus, one around 3 V and the other around 4 V. When the lithium ions in the 8a tetrahedral sites are extracted from the structure, manganese ions in the spinel lattice oxidizes from Mn^{3+} to Mn^{4+}, exhibiting the voltage profile at around 4 V. If all the lithium ions are extracted from the 8a tetrahedral sites, it will give λ-MnO_2, maintaining the same spinel structure and reducing the lattice parameter value due to an oxidation of larger Mn^{3+} ions to smaller Mn^{4+} ions. In contrast, when an additional lithium ion is inserted into the $LiMn_2O_4$

spinel lattice, the inserted lithium ions occupy the empty 16c octahedral sites, resulting in a reduction of Mn^{4+} to Mn^{3+} ions and exhibiting the voltage profile around 3 V. The addition of lithium ions into the unoccupied 16c octahedral sites, however, causes the already existing lithium ions in the 8a tetrahedral sites to move to the 16c octahedral sites in order to minimize the electrostatic repulsion between the lithium ions in the 8a and 16c sites, resulting in a tetragonally distorted $[Li_2]_{16c}[Mn_2]_{16d}O_4$.[55-57] The tetragonal transformation from the cubic phase is attributed to the Jahn-Teller distortion associated with the high spin Mn^{3+}:$3d^4$ ion with a single electron in the e_g orbital. Although both the lithium extraction/insertion from/into the 8a tetrahedral and 16c octahedral sites involves the $Mn^{3+/4+}$couple, differences in site energies between the 8a tetrahedral and 16c octahedral sites cause 1 V difference.

1.3.3 Spinel $Li_2Mn_4O_9$ and $Li_4Mn_5O_{12}$

Oxygen contents in the spinel $LiMn_2O_{4\pm\delta}$ can be controlled by the precursor materials employed and the synthesis temperature and duration. The end member $Li_2Mn_4O_9$ (δ = 0.5) having an oxidation state of 4+ for manganese, in which the excess oxygen ions are accommodated by cation vacancies to give a cation-deficient spinel lithium manganese oxide, has been obtained by synthesizing at low temperatures.[58] Spinel $Li_4Mn_5O_{12}$ is also an end member of the lithium excess $Li_{1+x}Mn_{2-y}O_4$ spinel series (x = 0.33), containing all Mn^{4+} in the lattice.[59] Since both

$Li_2Mn_4O_9$ and $Li_4Mn_5O_{12}$ are difficult to synthesize by conventional high-temperature process, solid-state reactions and solution-based synthesis at moderate temperatures (< 500 ^oC) have been adopted to obtain them.[60,61]

In the spinel $Li_2Mn_4O_9$ and $Li_4Mn_5O_{12}$ systems containing only Mn^{4+} in the lattice, lithium ions cannot be extracted since it is difficult to oxidize Mn^{4+} to Mn^{5+}. However, insertion of lithium into the 16c octahedral sites could be accomplished, resulting in reversible capacity in the 3 V region. However, the cubic symmetry could be preserved only up to $x = 1.7$ in $Li_{2+x}Mn_4O_9$ and up to $x = 2.5$ in $Li_{4+x}Mn_5O_{12}$ during the discharge process[62,63] due to the occurrence of Jahn-Teller distortion at high concentrations of Mn^{3+} ions.

1.3.4 High Voltage Spinel $LiMn_{2-y}M_yO_4$

Substitution of manganese ions by other metal ions M^{n+} having lower oxidation states such as Cr^{3+}, Fe^{3+}, Co^{3+}, Ni^{2+}, and Cu^{2+} increases the average oxidation state of Mn in spinel $LiMn_{2-y}M_yO_4$ to maintain charge neutrality.[64-80] For example, $LiMn_{1.5}Ni_{0.5}O_4$, in which all the manganese ions are tetravalent, could be obtained by a replacement of 25 % of manganese ions ($Mn^{3.5+}$) by nickel ions (Ni^{2+}) in $LiMn_2O_4$. Unlike the Mn^{4+}-containing systems such as $Li_4Mn_5O_{12}$ and $Li_2Mn_4O_9$, lithium extraction from $LiMn_{1.5}Ni_{0.5}O_4$ (Mn^{4+}) occurs around 5 V involving the oxidation of Ni^{2+} to Ni^{3+} and Ni^{4+}.

1.3.5 Capacity Fading Mechanisms in 4 V $LiMn_2O_4$

Spinel $LiMn_2O_4$ undergoes severe capacity fade, especially at elevated temperatures. Several mechanisms have been suggested in the literature to explain the capacity fade in the 4 V $LiMn_2O_4$ system. Manganese dissolution from the cathode lattice is generally thought to be the most important factor,[26,81-94] which occurs due to the following disproportionation reaction.

$$2\ Mn^{3+}\ (\text{Solid}) \rightarrow\ Mn^{2+}\ (\text{Solution}) + Mn^{4+}\ (\text{Solid}) \qquad [1.1]$$

This disproportionation reaction is facilitated by trace amounts of HF generated by the trace amounts of water present in the electrolyte as shown in Equation 1.2.

$$LiPF_6 + H_2O \rightarrow LiF\ (\text{Solution}) + 2\ HF\ (\text{Solution}) + POF_3\ (\text{Solid}) \qquad [1.2]$$

The acidic environment generated by HF accelerates the disproportionation of Mn^{3+} to Mn^{2+} and Mn^{4+}, resulting in a loss of Mn^{2+} ions into the electrolyte and consequent capacity fade. Furthermore, it is known that the reduction of the dissolved manganese ions at the graphite/electrolyte interface results in an additional increase of charge-transfer impedance in lithium ion cells.

The Jahn-Teller distortion has also been ascribed to be one of the factors of capacity fade in spinel $LiMn_2O_4$.[95-99] Mn^{3+} having a high spin $3d^4$ configuration leads to a cooperative distortion of the MnO_6 octahedra due to a lowering of the energy in the tetragonal crystal field compared to that in the octahedral geometry (Fig. 1.8).

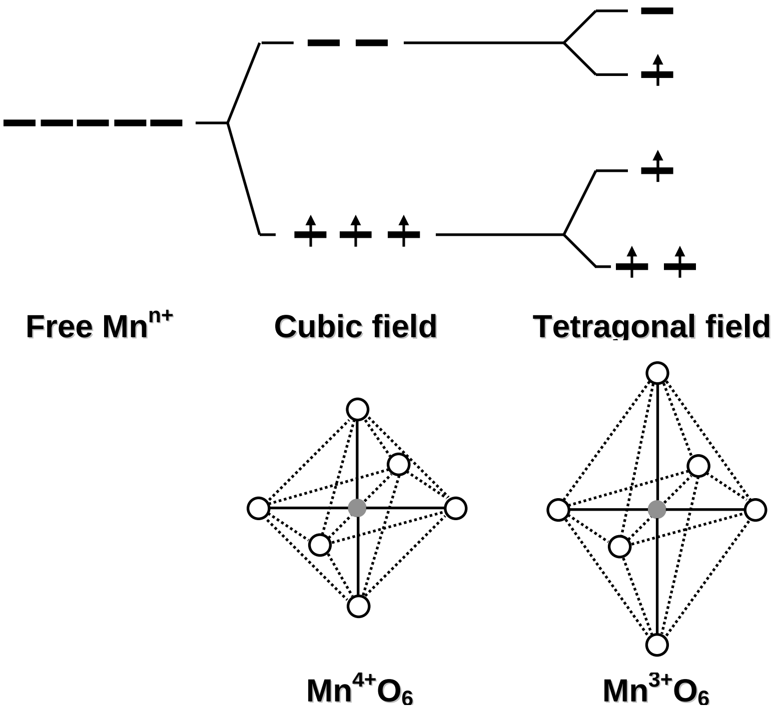

Figure 1.8 Illustration of the Jahn-Teller distortion in manganese oxides.

These transformations usually accompany a huge volume change of about 6.5 %, resulting in a loss of interparticle contact and an increase in impedance. Although the 4 V spinel oxides having an average oxidation state of Mn ≥ 3.5+ are not anticipated to give Jahn-Teller distortion in principle, the tetragonal phase has been observed on the surface of spinel particles under high rates of charge due to the inhomogeneity in lithium concentration between the surface and the bulk at the end of discharge. Also, loss of crystallinity,[100,101] formation of two cubic phases during the charge-discharge process,[102-105] instability of the two-phase structure in the charged state resulting in a loss of MnO to form a more stable single-phase structure,[82,106-108] and development of microstrain due to the difference in lattice parameter between the two cubic phases formed during cycling[102,104] have been suggested to be the source of capacity fade.

In order to suppress the capacity fade at elevated temperatures, several approaches such as cationic substitutions,[46,102-105,109-126] low temperature synthesis,[127-129] and surface modifications[81,130-134] have been pursed over the years in the literature. However, these modifications could not overcome the problems. Recently, in an effort to increase the reversible capacity of spinel cathodes, anionic substitutions have also been studied.[135-146]

1.4 OBJECTIVES

The objective of this dissertation is to develop a firm scientific understanding of the factors that control/influence the electrochemical performance of the spinel oxide cathodes and utilize the knowledge gained to design and develop high performance spinel manganese oxide compositions.

In this regard, the capacity fading mechanisms of spinel cathodes in the 4 V region are investigated by pursuing a variety of cationic substitutions for manganese and anionic substitutions for oxygen. The understanding obtained is then utilized to improve and optimize the cation- and anion-substituted spinel compositions. To improve the capacity retention of the cation- and anion-substituted spinel cathodes further, addition of small amounts of $LiMO_2$ layered oxide cathodes into spinel in order to trap the protons during the first charge to high voltages (~ 4.7 V) is also pursued.

Additionally, anionic substitutions in the 3 V spinel $Li_4Mn_5O_{12}$ oxide are investigated in order to extend the knowledge gained with the 4 V spinel systems. From the investigation, the factors influencing the electrochemical performances of 3 V spinel cathodes are discussed.

CHAPTER 2

GENERAL EXPERIMENTAL TECHNIQUES

2.1 MATERIALS SYNTHESIS

All the oxides investigated in this dissertation were prepared by conventional solid-state reaction or coprecipitation methods. Reagent grade commercial chemicals of transition metal oxides and lithium carbonate were used for solid-state reactions and transition metal acetates and lithium hydroxide were used for solution-based synthesis. In the case of fluorine substituted spinel samples, LiF, ZnF_2, or NH_4HF_2 were used for synthesis. The detailed synthesis conditions and procedures will be presented in the respective chapters.

2.2 CHEMICAL LITHIUM EXTRACTION

Chemical extraction of lithium was carried out by stirring the spinel powders in an acetonitrile solution of various quantities of NO_2BF_4 for 2 days under argon atmosphere by using a Schlenk line. The general reaction is given in Equation 2.1:

$$\mathrm{LiMn_{2-y-z}Li_yM_zO_{4-\eta}F_\eta} + x\,\mathrm{NO_2BF_4}$$

$$\rightarrow \quad \mathrm{Li_{1-x}Mn_{2-y-z}Li_yM_zO_{4-\eta}F_\eta} + x\,\mathrm{NO_2} + x\,\mathrm{LiBF_4} \qquad [2.1]$$

The reaction products were washed several times with acetonitrile under argon atmosphere to remove $LiBF_4$ and dried under vacuum at ambient temperature.

2.3 MANGANESE DISSOLUTION

The amount of manganese ions dissolved from the oxide powders into the electrolyte was measured with atomic absorption spectroscopy (AAS) after storing the spinel powders in 1 M $LiPF_6$ in ethylene carbonate (EC) and diethyl carbonate (DEC) electrolyte in a Teflon vessel at 55 ^{o}C for 7 days, collecting the electrolyte by filtration with a glass filter, and diluting with deionized water and nitric acid.[82,83,147]

Manganese dissolution was also measured with coin cells using AAS. After storing the coin cell at 60 ^{o}C, the cell was opened and the cell components (cathode, anode, and separator) were put into deionized water and propylene carbonate (PC) to collect the dissolved manganese ions. Nitric acid was then added to make a homogenous mixture of PC with the aqueous medium.[87]

2.4 MATERIALS CHARACTERIZATION

The materials synthesized were characterized by the following techniques. More specific procedures will be presented in the respective chapters.

2.4.1 X-ray Powder Diffraction (XRD)

X-ray powder diffraction data were collected with a Philips X-ray diffractometer with Cu Kα radiation to identify the phases in the samples. Diffraction patterns were recorded either at a fast scan rate of 0.05° per 2 seconds or at a slow scan rate of 0.02° per 5 seconds between 10 and 70°. The collected data were compared with the JCPDS files for phase identification. For more detailed structural analyses, Rietveld refinement method with DBWS-9411 program[148,149] and JADE software were employed.

2.4.2 Atomic Absorption Spectroscopy (AAS)

The lithium contents (1-x) in the chemically delithiated $Li_{1-x}Mn_{2-y-z}Li_yM_zO_{4-\eta}F_\eta$ samples as well as in the parent samples synthesized were determined with a Perkin-Elmer 1100 atomic absorption spectrometer. Sample solutions for AAS were prepared by adding approximately 50 mg of the samples into concentrated HCl and then heating around 60 °C for an hour to dissolve the samples completely, followed by diluting to the required concentrations with deionized water. Before the analysis of the sample solutions, the instrument was calibrated with a standard solution containing a known amount of the element being analyzed.

2.4.3 Redox Titration

The average oxidation state of manganese was determined by a redox titration with oxalate.[150] About 50 mg of sample was dissolved in a mixture of 20 ml of 0.05 N sodium oxalate ($Na_2C_2O_4$) and 20 ml of 4 N H_2SO_4 at around 65 ^oC. During this process, all Mn^{3+} and Mn^{4+} ions in the spinel are reduced to Mn^{2+} according to the reaction given in equation 2.2:

$$x\ C_2O_4{}^{2-} + 2Mn^{(2+x)+} \rightarrow 2Mn^{2+} + 2xCO_2 \qquad [2\text{-}2]$$

The remaining unreacted oxalate was then determined by titrating the warm solution (65 ^oC) with a 0.05 N potassium permanganate ($KMnO_4$) solution. During this reaction, the following reaction takes place.

$$5(C_2O_4)^{2-} + 2Mn^{7+} \rightarrow 2Mn^{2+} + 10CO_2 \qquad [2\text{-}3]$$

The end point of the reaction is the point at which the solution turns from colorless to pink. From the titration value and charge neutrality principle, the oxidation state of manganese and oxygen content were determined.

2.4.4 Scanning Electron Microscopy (SEM)

The morphology of the materials was investigated with a JEOL LSM-5610 scanning electron microscope.

2.4.5 Surface Area Measurement

The surface area of the materials was measured with a Quantachrome Autosorb-1 surface area analyzer using the Brunauer-Emmett-Teller (BET) method. After removing the pre-adsorbed gases in vacuum at 200 ^{o}C, the measurement was carried out with nitrogen gas as an adsorbate.

2.5 ELECTROCHEMICAL CHARACTERIZATION

The electrochemical performances of materials were evaluated with CR2032 coin cells consisting of cathode, anode, electrolyte, and polypropylene separator. The cathodes were prepared by mixing 75 wt. % cathode powder with 20 wt. % acetylene black and 5 wt. % polytetrafluoroethylene (PTFE) binder, rolling the mixture into a thin sheet and cutting into circular electrodes of 0.64 cm^2 area. Lithium metal or commercial carbon was used as the anode, and 1 M LiPF$_6$ in EC/DEC was employed as the electrolyte.

2.5.1 Cycling Performance and Rate Capability Evaluation

Cycling performances were carried out by repeating the charging and discharging process at C/5 rate up to 50 cycles in the appropriate voltage ranges depending on the samples. The rate capabilities were evaluated by first charging the cells at C/10 rate and then discharging at various rates from C/10 to 4C rate between 4.3 and 3.5 V.

2.5.2 Storage Test

The storage performances were carried out by subjecting the coin cells to one charge-discharge cycle at room temperature between 4.3 and 3.5 V followed by discharging to various depths of discharge (DOD) in the second cycle, storing at 60 ^{o}C for 7 days at various DOD, completing the second discharge cycle after cooling to ambient temperatures, and evaluating the full discharge capacity in the third cycle at room temperature.

CHAPTER 3

FACTORS CONTROLLING THE ELECTROCHEMICAL PERFORMANCES OF 4 V SPINEL CATHODES

3.1 INTRODUCTION

Lithium ion batteries have become attractive for portable electronic devices such as cell phones and laptop computers due to their higher energy density compared to other rechargeable systems. However, the high cost, toxicity, and safety issues associated with the currently used layered $LiCoO_2$ cathode remain as an impediment for employing the lithium ion battery technology for electric vehicles (EV) and hybrid electric vehicles (HEV). In this regard, spinel $LiMn_2O_4$ is appealing as Mn is inexpensive and environmentally benign and the $Mn^{3+/4+}$ couple is chemically more stable with good safety characteristics compared to the $Co^{3+/4+}$ couple. Also, the high rate capability of spinel oxides makes them attractive for EV and HEV applications.

However, $LiMn_2O_4$ is plagued by severe capacity fade at elevated temperatures. The capacity fade has been attributed to several mechanisms such as the formation of tetragonal $Li_2Mn_2O_4$ on the surface due to the Jahn-Teller distortion at the end of discharge,[55-57] electrochemical reaction with the electrolyte at high voltages,[151,152] loss of crystallinity during cycling,[100,101] cation mixing between the lithium and manganese sites in the spinel lattice,[153] formation of oxygen-deficiency,[154] formation of two cubic phases with a large difference in lattice parameter during the charge-discharge process,[102–105] instability of the two-phase structure in the charged state resulting in a loss of MnO to form a more stable single-phase structure,[82,106-108] and manganese dissolution from the lattice into the electrolyte due to the disproportionation of Mn^{3+} (into Mn^{2+} and Mn^{4+}) caused by trace amounts of HF present in the electrolyte.[26,81,83,85,109] Among them, manganese dissolution is generally thought to be the most important factor causing the capacity fade.

In this chapter, the transition metal ion dissolution from various cathode materials such as layered, orthorhombic $LiMnO_2$, 4 V spinel, 5 V spinel, and olivine oxides are compared with an aim to develop a better understanding of the influence of metal ion dissolution on electrochemical properties. Also, the dependence of manganese dissolution on Mn^{3+} vs Mn^{4+} content is investigated. Furthermore, from a systematic investigation of cationic and anionic substituted spinel oxides, a correlation of manganese dissolution to (i) the lattice parameter difference between the two cubic phases formed during the charge-discharge process and (ii) capacity retention is presented.

3.2 EXPERIMENTAL

$LiCoO_2$ was prepared by firing stoichiometric amounts of Li_2CO_3 and Co_3O_4 at 900 ^oC for 24 h in air. Layered $LiNi_{0.5-y}Mn_{0.5-y}Co_{2y}O_2$ ($0 \leq 2y \leq 0.58$) in which Ni, Mn, and Co exist as Ni^{2+}, Mn^{4+}, and Co^{3+} were synthesized by firing the coprecipitated hydroxides of Mn, Co, and Ni with lithium hydroxide at 900 ^oC for 24 h in air.[33] Orthorhombic $LiMnO_2$ and layered $LiMn_{0.8}Cr_{0.2}O_2$ (monoclinic) were synthesized by firing required amounts of Li_2CO_3, Mn_2O_3, and Cr_2O_3 at 1000 ^oC in N_2 atmosphere.[155] The 4 V spinel $LiMn_{2-y-z}Li_yM_zO_{4-\eta}F_\eta$ (M = Al, Ti, Ni, and Cu) oxides were synthesized by firing required amounts of Li_2CO_3, Mn_2O_3, Al_2O_3, TiO_2, NiO, CuO, and LiF at 800 ^oC for 48 h in air. The 5 V spinel $LiMn_{1.5}Ni_{0.5}O_4$ oxide and its derivatives in which manganese exists as Mn^{4+} were synthesized by firing the coprecipitated metal hydroxides with a required amount of lithium hydroxide at 900 ^oC for 12 h in air.[156] Olivine $LiFePO_4$ was prepared by firing required amounts of Li_2CO_3, $Fe(CH_3COO)_2$, and $NH_4H_2PO_4$ in N_2 atmosphere first at 320 ^oC for 3 h and then at 700 ^oC for 10 h with an intermittent grinding.

The fluorine contents in the synthesized samples were calculated based on the experimentally determined lithium contents and average oxidation state of the transition metal ions, employing the charge neutrality principle and assuming the total anion (O + F) content to be 4.0. The lithium contents were determined by atomic absorption spectroscopy (AAS) and the oxidation state was determined by a redox titration involving sodium oxalate and potassium permanganate as discussed in chapter 2. The error bars in the lithium contents and oxidation state values are, respectively, ±0.01 and ±0.02. The amount of dissolved metal ion was carried out by soaking the sample powders in the electrolyte at 55 ^oC for 7 days as described in chapter 2. Chemical extraction of lithium was carried out by stirring the $LiMn_{2-y-z}Li_yM_zO_{4-\eta}F_\eta$ powders with an acetonitrile solution of the oxidizer NO_2BF_4 for 2 days. Lattice parameters of the chemically delithiated spinel oxide compositions were determined by Rietveld analysis of the X-ray diffraction (XRD) data.[149] The cathodes for evaluating the electrochemical performances were prepared as described in chapter 2.

3.3 RESULTS AND DISCUSSION

3.3.1 Transition Metal Ion Dissolution from Various Cathodes

Table 3.1 compares the amount of transition metal ion (Mn, Co, Ni, and Fe) dissolution from layered, orthorhombic $LiMnO_2$, 4 V spinel, 5 V spinel, and olivine oxides. The amounts of each dissolved metal ion as well as the total amount of dissolved transition metal ions are expressed in % based on the sample weight. The error bar in the % Mn dissolution values is ±0.1 %. The layered $LiCoO_2$ that is currently used in lithium ion cells exhibits a low cobalt dissolution of 0.8 %. On the other hand, the layered $LiNi_{0.5-y}Mn_{0.5-y}Co_{2y}O_2$ oxides (samples 2-7 in Table 3.1) in which manganese exists as Mn^{4+} exhibit a total metal ion dissolution of 0.9 – 1.8 % and a manganese dissolution of < 0.4 %. With these low to moderate total metal ion dissolution, these layered oxides are known to exhibit good capacity retention.[33] In contrast, layered $LiMn_{0.8}Cr_{0.2}O_2$ (sample 8 in Table 3.1) and orthorhombic $LiMnO_2$ (sample 9 in Table 3.1) in which manganese exists as Mn^{3+} exhibit a high manganese dissolution of 2.6 – 3.2 %. Similarly, $LiMn_2O_4$ spinel (sample 10 in Table 3.1) in which manganese exists as $Mn^{3.5+}$ shows a high manganese dissolution of 3.2 %. Interestingly, the 5 V spinels based on $LiMn_{1.5}Ni_{0.5}O_4$ (samples 11 to 14 in Table 3.1) in which manganese exists as Mn^{4+} exhibit a much lower total metal ion dissolution of 0.3 – 0.7 % compared to $LiMn_2O_4$. The data reveal that the presence of Mn^{3+} leads to a significantly larger amount of manganese dissolution compared to Mn^{4+} due to the disproportionation of Mn^{3+} to Mn^{2+} and Mn^{4+}.[26] The data also confirm that the poor elevated temperature capacity retention of $LiMn_2O_4$ spinel compared to the 5 V spinels is due to the larger degree of manganese dissolution. For a comparison, the olivine $LiFePO_4$ also shows a low metal ion dissolution of 0.5 %.

Table 3.1 Comparison of transition metal ion dissolution from various lithium ion battery cathodes.

Sample number	Composition	Metal ion dissolution[a] (%)				
		Mn	Ni	Co	Fe	total
1	$LiCoO_2$			0.8		0.8
2	$LiNi_{0.5}Mn_{0.5}O_2$	0.4	0.7			1.1
3	$LiNi_{0.425}Mn_{0.425}Co_{0.15}O_2$	0.3	0.8			1.1
4	$LiNi_{0.33}Mn_{0.33}Co_{0.33}O_2$	0.2	0.4	0.3		0.9
5	$LiNi_{0.29}Mn_{0.29}Co_{0.42}O_2$	0.4	1.1	0.3		1.8
6	$LiNi_{0.25}Mn_{0.25}Co_{0.5}O_2$	0.4	0.9	0.5		1.8
7	$LiNi_{0.21}Mn_{0.21}Co_{0.58}O_2$	0.3	0.8	0.5		1.6
8	$LiMn_{0.8}Cr_{0.2}O_2$	2.6				2.6
9	$LiMnO_2$	3.2				3.2
10	$LiMn_2O_4$	3.2				3.2
11	$LiMn_{1.5}Ni_{0.5}O_4$	0.3	0.3			0.6
12	$Li_{1.05}Mn_{1.53}Ni_{0.42}O_4$	0.2	0.1			0.3
13	$LiMn_{1.5}Ni_{0.42}Zn_{0.08}O_4$	0.4	0.3			0.7
14	$LiMn_{1.42}Ni_{0.42}Co_{0.16}O_4$	0.3	0.3			0.6
15	$LiFePO_4$				0.5	0.5

a % dissolution based on sample weight.

3.3.2 Manganese Ion Dissolution from 4 V Spinel Cathodes

Recognizing that the larger manganese dissolution leads to poor capacity retention with the $LiMn_2O_4$ spinel oxide, the amount of manganese dissolution from several cation-substituted $LiMn_{2-y-z}Li_yM_zO_4$ oxides and fluorine-substituted $LiMn_{2-y-z}Li_yM_zO_{4-\eta}F_\eta$ oxyfluorides was investigated. Table 3.2 compares the % manganese dissolution based on both the sample weight and the Mn weight. While the unsubstituted $LiMn_2O_4$ exhibits a high manganese dissolution of 3.2 % (based on sample weight), cationic substitutions for Mn suppress the manganese dissolution. However, while certain cationic substitutions such as $LiMn_{1.95}Li_{0.05}O_4$ and $LiMn_{1.88}Al_{0.12}O_4$ suppress the manganese dissolution only moderately to ~ 2.7 % (based on sample weight), others such as $LiMn_{1.88}Li_{0.06}Ni_{0.03}Al_{0.03}O_4$ and $LiMn_{1.85}Li_{0.075}Ni_{0.075}O_4$ suppress it significantly to ~ 1.5 % (based on sample weight).

Interestingly, there is no clear correlation between the extent of cationic substitution and the % manganese dissolution. For example, $LiMn_{1.88}Al_{0.12}O_4$ and $LiMn_{1.88}Li_{0.06}Ni_{0.03}Al_{0.03}O_4$ having the same degree of cationic substitution (0.12 or $Mn_{1.88}M_{0.12}$) differ significantly in the amount of manganese dissolution (2.6 vs. 1.3 % based on sample weight). Furthermore, with a given cationic substitution, the anionic substitution of fluorine for oxygen decreases the amount of manganese dissolution further, possibly due to a more ionic, stronger Mn-F bond compared to the Mn-O bond and surface passivation by the fluoride ions. For example, $LiMn_{1.85}Li_{0.075}Ni_{0.075}O_4$ and $LiMn_{1.85}Li_{0.075}Ni_{0.075}O_{3.94}F_{0.06}$ exhibit manganese dissolutions of, respectively, 1.5 and 1.1 % (based on sample weight). The manganese dissolution based on Mn weight in Table 3.2 also shows a trend similar to that found based on sample weight. Although one may suspect the particle size and surface area to influence the manganese dissolution, all the spinel samples presented in Table 3.2 had similar morphology, particle size (2-6 μm), and crystallite size (60-85 nm) as indicated by scanning electron microscopy (SEM) and XRD data.

Table 3.2 Manganese dissolution and capacity fade data of spinel manganese oxide cathodes.

Sample number	Composition	25 °C		60 °C		Mn dissolution[b] (%)	Mn dissolution[c] (%)	Mn valence[d]
		Initial capacity (mAh/g)	Capacity loss[a] (%)	Initial capacity (mAh/g)	Capacity loss[a] (%)			
1	$LiMn_2O_4$	119.2	35.2	121.2	53.5	3.2	5.3	3.50
2	$LiMn_2O_{3.94}F_{0.06}$	120.1	29.4	119.7	44.1	2.9	4.8	3.47
3	$LiMn_{1.95}Li_{0.05}O_4$	120.8	17.0	119.1	26.1	2.7	4.4	3.56
4	$LiMn_{1.9}Ni_{0.1}O_4$	112.8	8.3	114.2	12.9	2.2	3.7	3.58
5	$LiMn_{1.9}Ni_{0.1}O_{3.94}F_{0.06}$	117.7	5.6	116.2	8.9	1.8	3.1	3.55
6	$LiMn_{1.9}Li_{0.05}Ti_{0.05}O_4$	121.4	6.7	120.1	13.8	2.2	3.8	3.55
7	$LiMn_{1.9}Li_{0.05}Ni_{0.05}O_4$	113.2	3.3	113.0	4.0	1.7	2.9	3.61
8	$LiMn_{1.9}Li_{0.05}Ni_{0.05}O_{3.95}F_{0.05}$	116.5	2.9	114.1	3.4	1.2	2.1	3.58
9	$LiMn_{1.88}Al_{0.12}O_4$	115.4	16.1	116.7	27.2	2.6	4.4	3.53
10	$LiMn_{1.88}Cu_{0.06}Al_{0.06}O_4$	111.3	9.6	110.2	18.3	2.5	4.3	3.56
11	$LiMn_{1.88}Li_{0.06}Al_{0.06}O_4$	108.4	2.9	106.6	4.8	2.0	3.4	3.60
12	$LiMn_{1.88}Li_{0.06}Cu_{0.06}O_4$	106.8	3.5	107.9	9.3	2.3	3.9	3.63
13	$LiMn_{1.88}Li_{0.06}Ni_{0.03}Al_{0.03}O_4$	106.2	1.9	107.4	3.6	1.3	2.3	3.61
14	$LiMn_{1.85}Li_{0.075}Ni_{0.04}Al_{0.035}O_4$	98.8	1.8	96.1	3.1	1.4	2.5	3.64
15	$LiMn_{1.85}Li_{0.075}Ni_{0.075}O_4$	93.4	2.1	92.5	3.2	1.5	2.6	3.66
16	$LiMn_{1.85}Li_{0.075}Ni_{0.075}O_{3.94}F_{0.06}$	100.7	1.2	101.2	2.4	1.1	1.9	3.63

[a] % capacity loss after 50 cycles.

[b] % dissolution based on sample weight.

[c] % dissolution based on Mn weight.

[d] Calculated by assuming Li^+, Al^{3+}, Ti^{4+}, Ni^{2+}, Cu^{2+}, and F^-.

3.3.3 Cycling Performance of Spinel Cathodes

Figure 3.1 compares the cyclability data at 25 and 60 ^{o}C of some selected spinel oxide and oxyfluoride samples, and Table 3.2 gives the % capacity loss after 50 cycles at 25 and 60 ^{o}C. The cationic substitutions in general improve the capacity retention, but some cationic substitutions are more effective than others. For example, with the same amount of cationic substitution (0.12), $LiMn_{1.88}Al_{0.12}O_4$, $LiMn_{1.88}Li_{0.06}Cu_{0.06}O_4$, and $LiMn_{1.88}Li_{0.06}Ni_{0.03}Al_{0.03}O_4$ exhibit capacity fades of, respectively, 27.2, 9.3, and 3.6 % in 50 cycles at 60 ^{o}C. Furthermore, with a given cationic substitution, the fluorine substitution offers further improvement in capacity retention. For example, $LiMn_{1.85}Li_{0.075}Ni_{0.075}O_4$ and $LiMn_{1.85}Li_{0.075}Ni_{0.075}O_{3.94}F_{0.06}$ exhibit capacity fades of, respectively, 3.2 and 2.4% in 50 cycles at 60 ^{o}C. Interestingly, the capacity fade bears a clear relationship to manganese dissolution (Table 3.2); it decreases with decreasing amount of manganese dissolution, confirming the widespread belief of manganese dissolution as a capacity fade mechanism in the literature.[26,81,83,85,109]

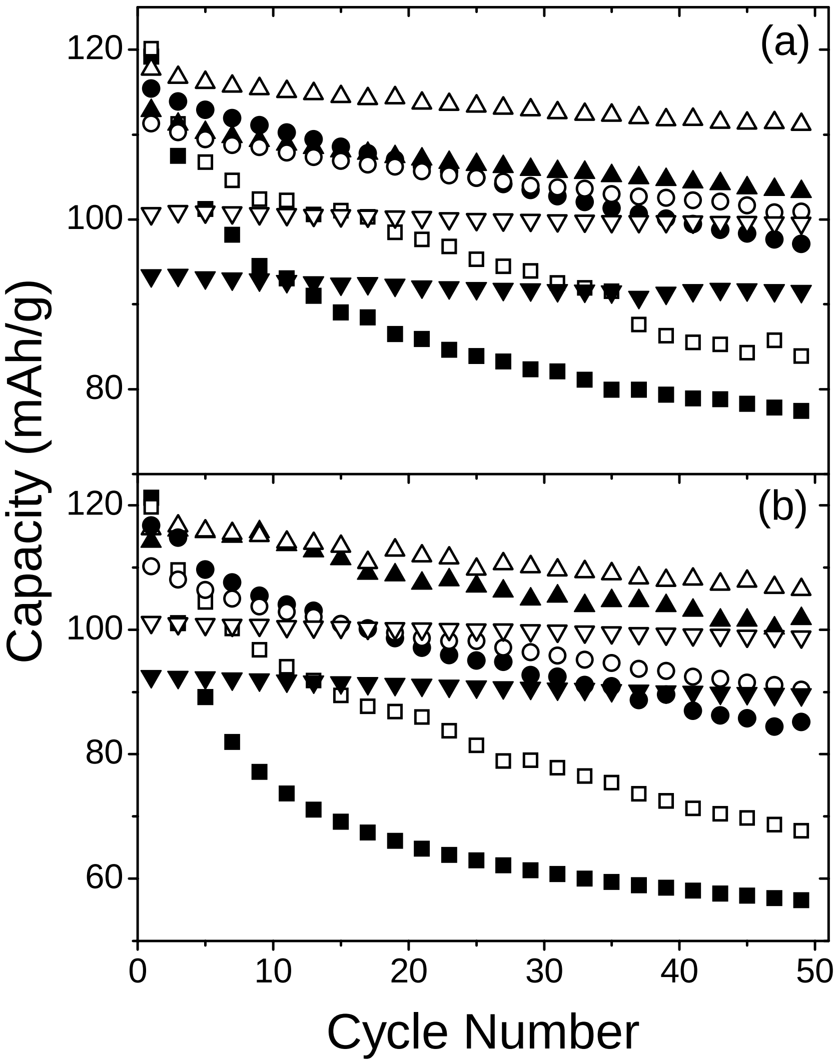

Figure 3.1 Comparison of the cycling performances of some selected spinel oxides and oxyfluorides at (a) 25 °C and (b) 60 °C at C/5 rate: (■) $LiMn_2O_4$, (□) $LiMn_2O_{3.94}F_{0.06}$, (▲) $LiMn_{1.9}Ni_{0.1}O_4$, (△) $LiMn_{1.9}Ni_{0.1}O_{3.94}F_{0.06}$, (●) $LiMn_{1.88}Al_{0.12}O_4$, (○) $LiMn_{1.88}Cu_{0.06}Al_{0.06}O_4$, (▼) $LiMn_{1.85}Li_{0.075}Ni_{0.075}O_4$, and (▽) $LiMn_{1.85}Li_{0.075}Ni_{0.075}O_{3.94}F_{0.06}$.

3.3.4 Initial Manganese Valence in Spinel Cathodes

In order to identify and understand the basic materials parameters and characteristics that may influence the degree of manganese dissolution and capacity fade, we first correlate in Fig. 3.2 the initial manganese valence in the samples to the capacity fade after 50 cycles at 60 ^{o}C, % manganese dissolution, and the lattice parameter difference Δa between the two cubic phases formed at (1-x) ≈ 0.3 to 0.5 in $Li_{1-x}Mn_{2-y-z}Li_yM_zO_{4-\eta}F_\eta$ during the charge-discharge process. It is known that the manganese spinel oxides encounter the formation of two cubic phases during the charge-discharge process[104,107,108,110] as indicated by a clear splitting of the reflections of, for example, $Li_{0.34}Mn_2O_4$ in Fig. 3.3. Although such a splitting decreases with cationic and anionic substitutions as seen in Fig. 3.3 for other compositions due to a smaller Δa, the broad peaks could be resolved by Rietveld analysis and the lattice parameters for the two cubic phases could be obtained. The Δa values thus obtained are plotted against the initial Mn valence in Fig. 3.2c. As seen in Fig. 3.2, the capacity fade, amount of manganese dissolution, and Δa show a relationship to the initial manganese valence, but with a significant scatter in the data points, suggesting that initial manganese valence may not be the only factor influencing the capacity retention. While samples with an initial manganese valence of > 3.6+ show a low and nearly constant capacity fade, manganese dissolution, and Δa, those with a manganese valence of < 3.6+ show an increase in capacity fade, manganese dissolution, and Δa with decreasing manganese valence, which is in accordance with the findings with some oxide compositions.[105]

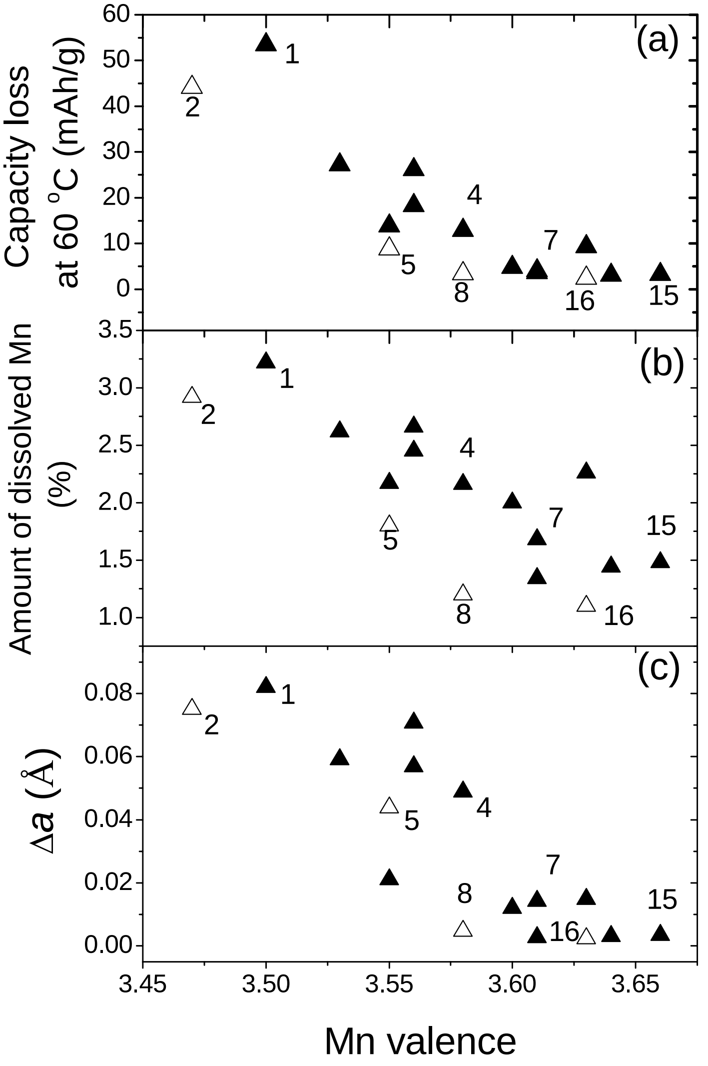

Figure 3.2 Correlation of the initial Mn valence to the (a) capacity loss after 50 cycles at 60 °C, (b) amount (%) of manganese dissolution, and (c) lattice parameter difference Δa between the two cubic phases formed during the charge-discharge process of the spinel cathodes. The closed and open triangles refer, respectively, to the oxide and oxyfluoride samples. The numbers refer to the sample numbers in Table 3.2.

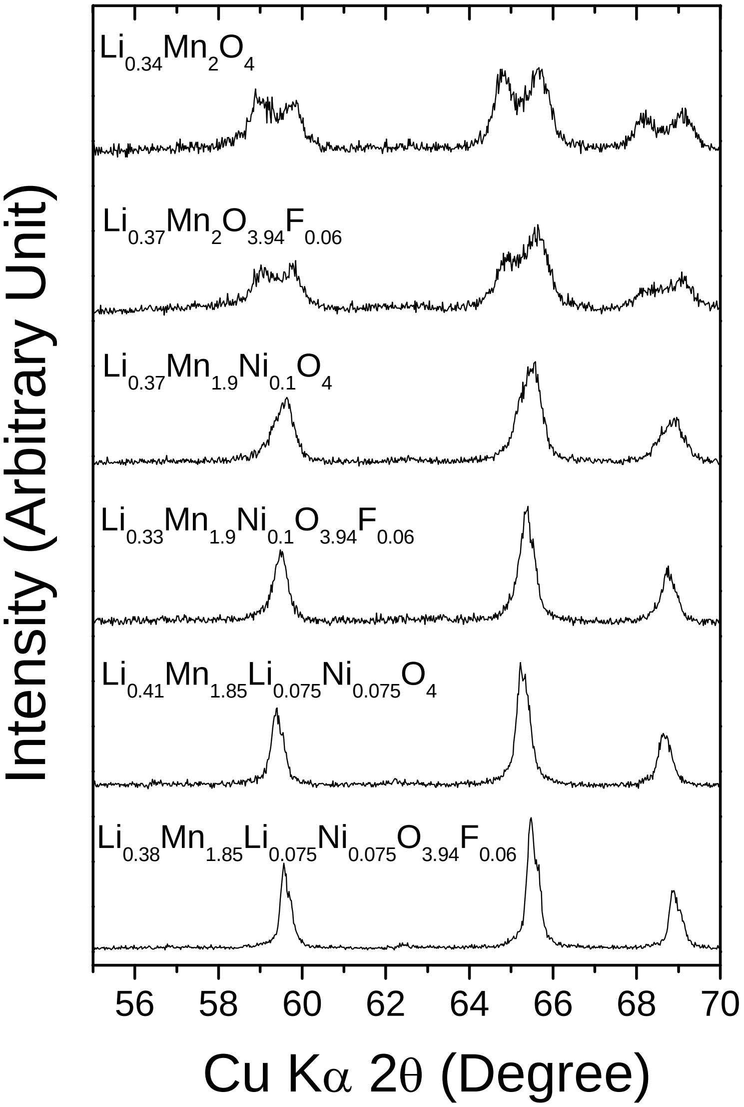

Figure 3.3 XRD patterns of chemically delithiated $Li_{1-x}Mn_{2-y-z}Li_yM_zO_{4-\eta}F_\eta$, illustrating the formation of two cubic phases.

3.3.5 Manganese Dissolution, Lattice Parameter Mismatch in the Two Phase Region, and Capacity Fade

To develop a further understanding, Fig. 3.4 relates the lattice parameter difference Δa between the two cubic phases formed during the charge-discharge process as well as the corresponding % volume change ΔV to the capacity fade after 50 cycles at 25 ^{o}C. Figure 3.4 also plots the lattice parameter difference Δa′ between the fully charged and discharged states. Clearly, the capacity fade decreases with decreasing Δa, ΔV, and Δa′. Figure 3.5 shows the correlation of capacity fade after 50 cycles at 60 ^{o}C to the lattice parameter difference Δa between the two cubic phases and the amount of manganese dissolution. The capacity fade decreases with decreasing Δa and manganese dissolution, suggesting a relationship between Δa and manganese dissolution. Figure 3.6 plots Δa versus manganese dissolution, and the samples with a smaller amount of manganese dissolution also exhibit a smaller Δa. This is consistent with a report by Xia et. al.[82] that the two-phase structure in the charged state results in the loss of MnO from the lattice. The results thus demonstrate that the capacity fade decreases with decreasing manganese dissolution, which in turn exhibits a clear relationship to Δa. In this regard, the Δa value may be used as a parameter to rapidly assess the capacity retention behavior and thereby screen the spinel oxide cathode compositions instead of carrying out the extensive, time consuming cycling tests.

An interesting aspect in Figs. 3.4-3.6 and in Table 3.2 is the influence of cationic and anionic substitutions in the $LiMn_2O_4$ spinel lattice. Some of the data points in Figs. 3.4-3.6 are numbered, which refer to the sample numbers in Table 3.2. While the unsubstituted $LiMn_2O_4$ exhibits a high Δa, manganese dissolution, and capacity fade, the cationic substitutions in general decrease them, with some substitutions much more effective than others. With a given cationic substitution, the anionic fluorine substitution decreases them further, resulting in a superior capacity retention for cation-substituted oxyfluorides.

However, the incorporated fluorine contents using LiF are only 25 % of the expected values due to the volatilization of fluorine at high temperatures, resulting in compositions such as $LiMn_2O_{3.94}F_{0.06}$, $LiMn_{1.9}Ni_{0.1}O_{3.94}F_{0.06}$, $LiMn_{1.9}Li_{0.05}Ni_{0.05}O_{3.95}F_{0.05}$, and $LiMn_{1.85}Li_{0.075}Ni_{0.075}O_{3.94}F_{0.06}$ compared to the theoretical composition of $LiMn_{2-y-z}Li_yNi_zO_{3.8}F_{0.2}$.

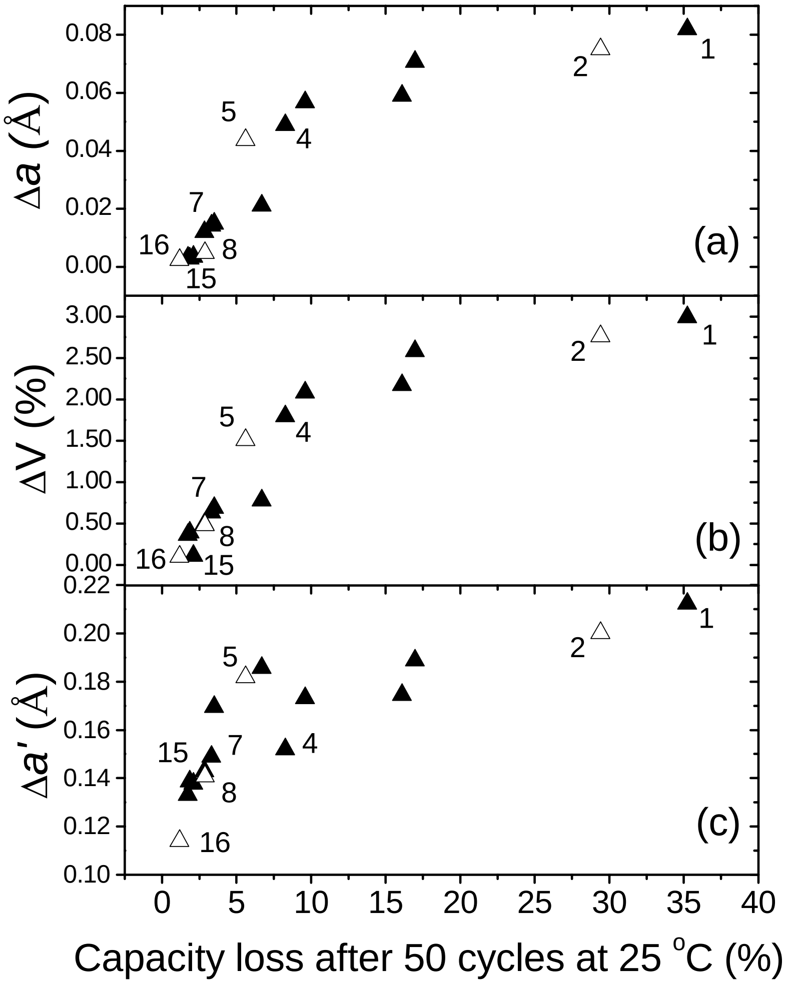

Figure 3.4 Correlation of the % capacity loss found after 50 cycles at room temperature to the lattice parameter differences (Δa and Δa′) and the volume change ΔV associated with the manganese spinel cathodes. Δa is the maximum lattice parameter difference between the two cubic phases formed at (1-x) ≈ 0.3 - 0.5 in $Li_{1-x}Mn_{2-y-z}Li_yM_zO_{4-\eta}F_\eta$, ΔV is the corresponding volume change calculated from Δa, and Δa′ is the lattice parameter difference between the fully discharged and charged states of $Li_{1-x}Mn_{2-y-z}Li_yM_zO_{4-\eta}F_\eta$. The closed and open triangles refer, respectively, to the oxide and oxyfluoride samples. The numbers refer to the sample numbers in Table 3.2.

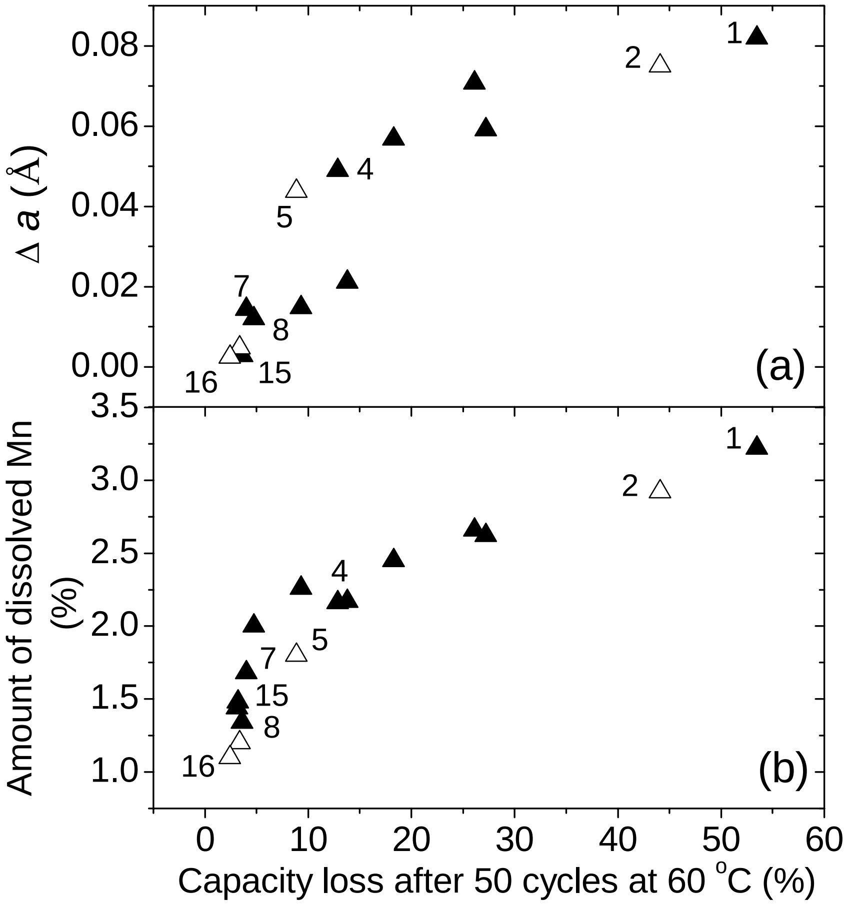

Figure 3.5 Correlation of the capacity loss after 50 cycles at 60 °C to the (a) lattice parameter difference Δa between the two cubic phases formed during the charge-discharge process and (b) amount of manganese dissolution for the spinel cathodes. The closed and open triangles refer, respectively, to the oxide and oxyfluoride spinel samples. The numbers refer to the sample numbers in Table 3.2.

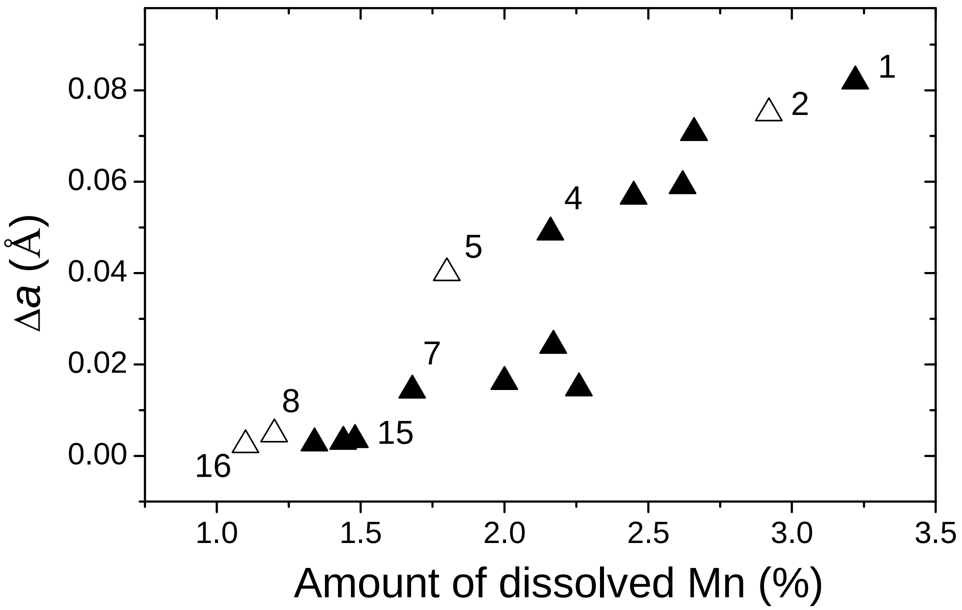

Figure 3.6 Correlation of the amount of manganese dissolution to the lattice parameter difference Δa between the two cubic phases formed during the charge-discharge process of the spinel cathodes. The closed and open triangles refer, respectively, to the oxide and oxyfluoride spinel samples. The numbers refer to the sample numbers in Table 3.2.

3.4 CONCLUSIONS

The transition metal ion dissolutions from layered, orthorhombic $LiMnO_2$, 4 V spinel, 5 V spinel, and olivine $LiFePO_4$ cathodes have been investigated systematically. The cathodes containing Mn^{3+} lead to a larger amount of manganese dissolution than the total metal ion dissolution found from cathodes containing Mn^{4+} or from $LiCoO_2$ and $LiFePO_4$. However, the amount of manganese dissolution from the Mn^{3+}-containing spinel cathodes could be reduced significantly through cationic and anionic substitutions. The reduction of manganese dissolution in such $LiMn_{2-y-z}Li_yM_zO_{4-\eta}F_\eta$ spinel is also accompanied by a much smaller lattice parameter difference Δa between the two cubic phases formed during the charge-discharge process. The reduced manganese dissolution leads to excellent capacity retention at elevated temperatures for cathode compositions such as $LiMn_{2-y-z}Li_yM_zO_{4-\eta}F_\eta$. Furthermore, the manganese dissolution bears a relationship to the lattice parameter difference Δa between the two cubic phases formed during the charge-discharge process. The reduction in the amount of manganese dissolution and a lowering of Δa by appropriate cationic and anionic substitutions may be an effective way to overcome the difficulties of employing the manganese spinel cathodes for EV and HEV applications. However, the volatilization of fluorine at high synthesis temperatures in the case of anionic substitutions employing LiF as a fluorine source necessitates a systematic investigation of other fluorine sources or lower temperature approaches, which will be the subject of investigation in the succeeding chapters.

CHAPTER 4

FLUORINE SUBSTITUTION USING ZnF_2 AND THE ELECTROCHEMICAL PERFORMANCE OF SPINEL $LiMn_{2-y-z}Li_yZn_zO_{4-\eta}F_\eta$ CATHODES

4.1 INTRODUCTION

As mentioned in the previous chapter, lithium manganese oxide crystallizing in the spinel structure has become appealing as manganese is inexpensive and environmentally benign while the presently used $LiCoO_2$ cathodes suffer from high cost, toxicity, and safety concerns. Although the spinel lithium manganese oxide cathodes exhibit severe capacity fade at elevated temperatures, several approaches such as cationic substitutions,[46,102-105,109-126] anionic substitutions,[135-146] and surface treatments[81,130-134] have been pursued over the years in the literature and found to suppress the capacity fade at elevated temperatures.

In chapter 3, improvements in the electrochemical performances of spinel cathodes through appropriate cationic and anionic substitutions, which were ascribed to the suppression of the lattice parameter mismatch between the two cubic phases formed and the reduction of manganese dissolution, were presented. Although anionic substitutions using LiF as a fluorine source offer improved electrochemical performance, controlled incorporation of fluorine into the spinel lattice was hard due to the volatilization of fluorine at high temperatures.

With an aim to control the fluorine contents incorporated and understand the factors that influence the electrochemical performance of anion-substituted spinel cathodes, the synthesis of a new series of spinel oxyfluorides $LiMn_{2-y-z}Li_yZn_zO_{4-\eta}F_\eta$ ($0 \leq y \leq 0.1$, $0 \leq z \leq 0.1$, and $0 \leq \eta \leq 0.18$) by utilizing ZnF_2 as a fluorine and zinc source and a comparison of the electrochemical properties with those of the analogous $LiMn_{2-y-z}Li_yZn_zO_4$ spinel oxides synthesized by utilizing ZnO as a zinc source are presented in this chapter.

4.2 EXPERIMENTAL

The fluorine-substituted spinel $LiMn_{2-y-z}Li_yZn_zO_{4-\eta}F_\eta$ ($0 \leq y \leq 0.1$, $0 \leq z \leq 0.1$, and $0 \leq \eta \leq 0.18$) were synthesized by firing required amounts of Li_2CO_3 and Mn_2O_3 with ZnF_2 at 800 °C for 48 h in air whereas the corresponding $LiMn_{2-y-z}Li_yZn_zO_4$ oxide analogs were synthesized by using ZnO instead of ZnF_2. The lithium contents in the products were analyzed by atomic absorption spectroscopy (AAS). The average oxidation state of manganese was determined by a redox titration involving sodium oxalate and potassium permanganate. Chemical extraction of lithium was carried out by stirring the $LiMn_{2-y-z}Li_yZn_zO_{4-\eta}F_\eta$ powder with an acetonitrile solution of the oxidizing agent NO_2BF_4 for 2 days under argon atmosphere, followed by washing the products with acetonitrile.[31]

All samples were characterized by X-ray diffraction, and the cation distributions as well as the lattice parameters of the parent samples, and the two cubic phases formed during chemical delithiation were determined by Rietveld analysis.[149] The degree of manganese dissolution was assessed by soaking the parent sample powders in the electrolyte containing 1 M $LiPF_6$ in 1:1 ethylene carbonate (EC) and diethyl carbonate (DEC) at 55 ^oC for 7 days and determining the amount of manganese in the electrolyte by AAS. The cathodes for evaluating the electrochemical performances were prepared as described in chapter 2, and the electrochemical performance evaluations were carried out with CR2032 coin cells.

4.3 RESULTS AND DISCUSSION

4.3.1 Crystal Chemistry

Table 4.1 gives the average oxidation state values of the manganese ions determined by the redox titration analysis. The oxidation state values of the $LiMn_{2-y-z}Li_yZn_zO_{4-\eta}F_\eta$ oxyfluoride samples are lower than those of the corresponding oxide analogs $LiMn_{2-y-z}Li_yZn_zO_4$ due to a replacement of the divalent O^{2-} ions by the monovalent F^- ions. The fluorine contents in the samples were calculated based on the lithium content and the average oxidation state value of manganese obtained from, respectively, the AAS and redox titration data, employing charge neutrality principle and assuming the total anion (O + F) content to be 4.0. As seen in Table 4.1, fluorine contents of up to $\eta = 0.18$ was incorporated into the $LiMn_{1.8}Li_{0.1}Zn_{0.1}O_{3.82}F_{0.18}$ spinel lattice, suggesting that ZnF_2 could be utilized as an effective fluorine source compared to the common use of LiF in the literature,[137,138,140,] as the latter could be more prone to volatilization at the elevated synthesis temperatures of ~ 800 ^oC. Also, the amount of fluorine that could be incorporated tends to increase as the oxidation state of manganese in the oxide analog $LiMn_{2-y-z}Li_yZn_zO_4$ increases since it becomes difficult to lower the oxidation state of manganese in the spinel lattice through fluorine substitution below about 3.5+. For example, the increase in fluorine content on going from $LiMn_{1.9}Zn_{0.1}O_{3.87}F_{0.13}$ to $LiMn_{1.8}Li_{0.1}Zn_{0.1}O_{3.82}F_{0.18}$ is due to a higher manganese oxidation state of 3.72+ in the corresponding oxide analog $LiMn_{1.8}Li_{0.1}Zn_{0.1}O_4$ compared to 3.58+ in $LiMn_{1.9}Zn_{0.1}O_4$.

Figure 4.1 compares the XRD patterns of some of the $LiMn_{2-y-z}Li_yZn_zO_{4-\eta}F_\eta$ and $LiMn_{2-y-z}Li_yZn_zO_4$ samples. The data indicate that all the samples are single phase cubic spinel materials. The Rietveld refinement was carried out with a model in which the $Mn^{3+/4+}$ ions were constrained to the octahedral B sites while the Li^+ and Zn^{2+} ions were permitted to occupy both the octahedral B sites and the tetrahedral A sites. For all the $LiMn_{2-y-z}Li_yZn_zO_{4-\eta}F_\eta$ and $LiMn_{2-y-z}Li_yZn_zO_4$ samples, most of the Zn^{2+} ions were found to be located in the tetrahedral A sites. For example, $LiMn_{1.9}Zn_{0.1}O_4$ and $LiMn_{1.8}Li_{0.1}Zn_{0.1}O_4$ showed a tetrahedral A site occupancy of, respectively, 0.10(3) and 0.98(8) with an R_{wp} value of, respectively, 11.1 and 12.7. Table 4.1 gives the lattice parameter values of the $LiMn_{2-y-z}Li_yZn_zO_{4-\eta}F_\eta$ and $LiMn_{2-y-z}Li_yZn_zO_4$ samples. For a given cationic composition, the incorporation of fluorine results in an increase in the lattice parameter value due to a reduction of the smaller Mn^{4+} ions to larger Mn^{3+} ions, confirming the incorporation of fluorine into the spinel lattice and the assertions based on the chemical analysis data.

Table 4.1 Chemical, structural, and electrochemical characterization data of spinel manganese cathodes.

Sample number	Composition	Initial Capacity (mAh/g)	Capacity loss (%)		Lattice parameter (Å)	Initial Mn valence[a]	Mn dissolution[b] (%)	% Volume change in the two-phase region
			25 °C	60 °C				
1	$LiMn_2O_4$	119	25.7	41.1	8.2471	3.50	3.2	2.87
2	$LiMn_{1.9}Zn_{0.1}O_4$	115	12.1	22.9	8.2317	3.58	2.4	2.11
3	$LiMn_{1.9}Zn_{0.1}O_{3.87}F_{0.13}$	120	8.2	13.7	8.2403	3.51	1.9	1.72
4	$LiMn_{1.9}Li_{0.05}Zn_{0.05}O_4$	108	9.7	15.3	8.2182	3.61	1.9	1.76
5	$LiMn_{1.9}Li_{0.05}Zn_{0.05}O_{3.90}F_{0.10}$	113	6.9	10.4	8.2349	3.55	1.6	1.13
6	$LiMn_{1.85}Li_{0.075}Zn_{0.075}O_4$	97	5.8	9.6	8.2081	3.66	1.8	0.77
7	$LiMn_{1.85}Li_{0.075}Zn_{0.075}O_{3.85}F_{0.15}$	104	3.9	5.4	8.2294	3.58	1.4	0.41
8	$LiMn_{1.8}Li_{0.1}Zn_{0.1}O_4$	76	3.9	6.5	8.2068	3.72	1.3	0.38
9	$LiMn_{1.8}Li_{0.1}Zn_{0.1}O_{3.82}F_{0.18}$	86	2.7	3.3	8.2101	3.62	0.5	0.26

[a] Calculated by assuming Li^+, Zn^{2+}, and F^-.

[b] % dissolution based on sample weight.

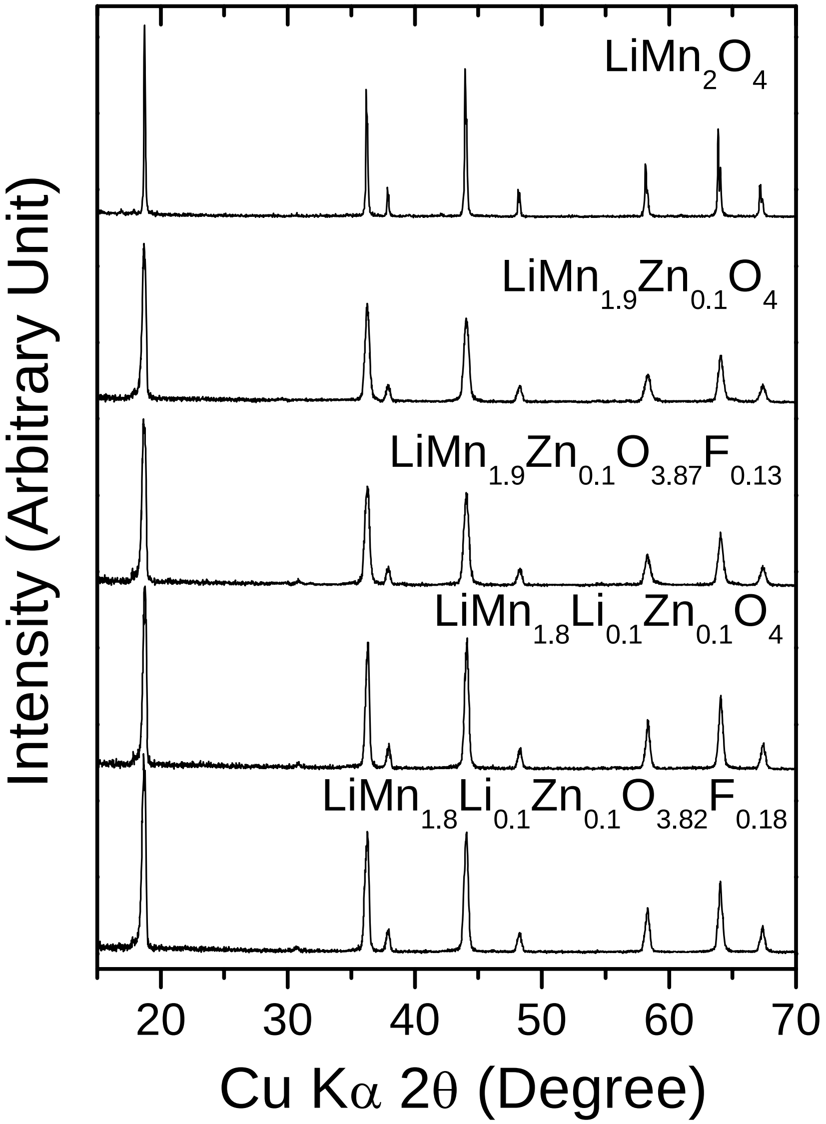

Figure 4.1 XRD patterns of selected $LiMn_{2-y-z}Li_yZn_zO_{4-\eta}F_\eta$ spinel cathodes synthesized by solid-state reactions at 800 °C.

4.3.2 Cycling Performance

Figure 4.2 compares the cycling performances of the $LiMn_{2-y-z}Li_yZn_zO_{4-\eta}F_\eta$ and $LiMn_{2-y-z}Li_yZn_zO_4$ cathodes at room temperature and 60 °C at C/5 rate while Table 4.1 gives the initial capacity values and the % capacity loss after 50 cycles at 25 and 60 °C. For the same degree of cationic substitution in $LiMn_{1.9}Zn_{0.1}O_4$ and $LiMn_{1.9}Li_{0.05}Zn_{0.05}O_4$, the doubly substituted $LiMn_{1.9}Li_{0.05}Zn_{0.05}O_4$ exhibits better capacity retention with a capacity fade of 15 % compared to the singly substituted $LiMn_{1.9}Zn_{0.1}O_4$ with a capacity fade of 23 % at 60 °C. This observation is consistent with previous findings that a co-substitution of small amounts of both Li and M (M = Ni and Al) for Mn to give $LiMn_{2-2y}Li_yM_yO_4$ ($0.05 \leq y \leq 0.1$) is more effective in improving the electrochemical properties compared to the single substitutions to give $LiMn_{2-y}M_yO_4$.[103,104] For a given cationic substitution, the oxyfluoride spinel compositions exhibit up to 10 mAh/g higher capacities than the corresponding oxide counterparts due to a lowering of the oxidation state of manganese. More importantly, the oxyfluoride cathodes exhibit an improvement in capacity retention especially at elevated temperatures. For example, $LiMn_{1.9}Zn_{0.1}O_{3.87}F_{0.13}$, $LiMn_{1.85}Li_{0.075}Zn_{0.075}O_{3.85}F_{0.15}$, and $LiMn_{1.8}Li_{0.1}Zn_{0.1}O_{3.82}F_{0.18}$ show capacity fades of 13.7, 5.4, and 3.3 %, respectively, after 50 cycles at 60 °C, while the corresponding oxide analogs exhibit capacity fades of, respectively, 22.9, 9.6, and 6.5 %. For a comparison, $LiMn_2O_4$ exhibits a much higher capacity fade of 41.1 %.

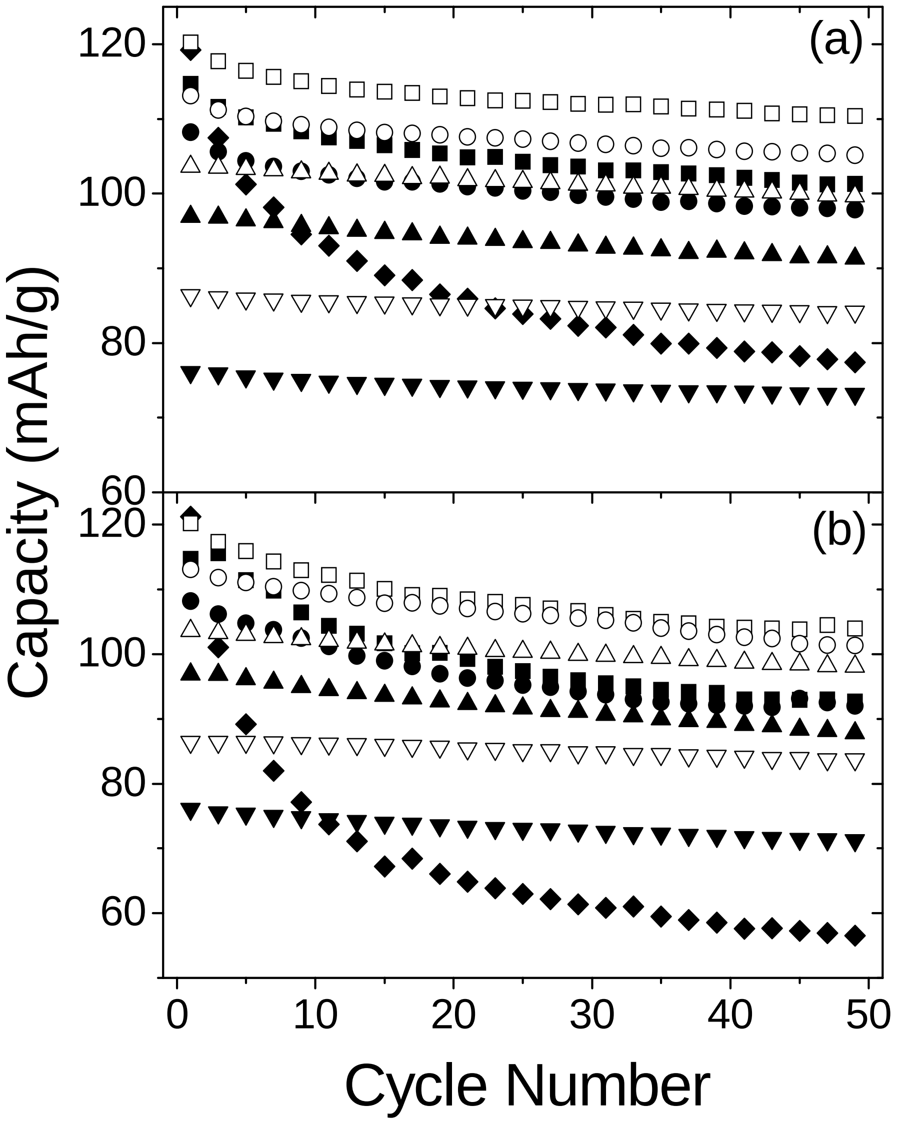

Figure 4.2 Comparison of the electrochemical cycling performances at (a) 25 °C and (b) 60 °C of $LiMn_{2-y-z}Li_yZn_zO_{4-\eta}F_\eta$: (◆) $LiMn_2O_4$, (■) $LiMn_{1.9}Zn_{0.1}O_4$, (□) $LiMn_{1.9}Zn_{0.1}O_{3.87}F_{0.13}$, (▲) $LiMn_{1.9}Li_{0.05}Zn_{0.05}O_4$, (△) $LiMn_{1.9}Li_{0.05}Zn_{0.05}O_{3.9}F_{0.1}$, (●) $LiMn_{1.85}Li_{0.075}Zn_{0.075}O_4$, (○) $LiMn_{1.85}Li_{0.075}Zn_{0.075}O_{3.85}F_{0.15}$, (▼) $LiMn_{1.8}Li_{0.1}Zn_{0.1}O_4$, and (▽) $LiMn_{1.8}Li_{0.1}Zn_{0.1}O_{3.82}F_{0.18}$.

4.3.3 Rate Capability

Figure 4.3 compares the rate capabilities of two selected $LiMn_{2-y-z}Li_yZn_zO_{4-\eta}F_\eta$ cathodes with those of $LiMn_2O_4$ and the analogous $LiMn_{2-y-z}Li_yNi_zO_4$. The data were collected at room temperature between 3.5 and 4.3 V by charging at the same rate of C/10 but with different discharge rates of C/10 to 4C. Both $LiMn_{1.85}Li_{0.075}Zn_{0.075}O_4$ and $LiMn_{1.85}Li_{0.075}Zn_{0.075}O_{3.85}F_{0.15}$ exhibit better rate capability with a retention of ~ 90 % of their capacities on going from C/10 to 4C rate compared to 46 % retention for $LiMn_2O_4$, which is in accordance with earlier findings that the cation-substituted samples generally exhibit better rate capabilities than $LiMn_2O_4$.[103,104] However, the Zn- and Li-substituted $LiMn_{1.85}Li_{0.075}Zn_{0.075}O_4$ and $LiMn_{1.85}Li_{0.075}Zn_{0.075}O_{3.85}F_{0.15}$ exhibit lower rate capabilities compared to the analogous Ni- and Li- substituted $LiMn_{1.8}Li_{0.1}Ni_{0.1}O_4$ and $LiMn_{1.8}Li_{0.1}Ni_{0.1}O_{3.8}F_{0.2}$ due to the blocking of Li^+ ion diffusion pathways by the Zn^{2+} ions present in the tetrahedral sites as indicated by the Rietveld analysis.

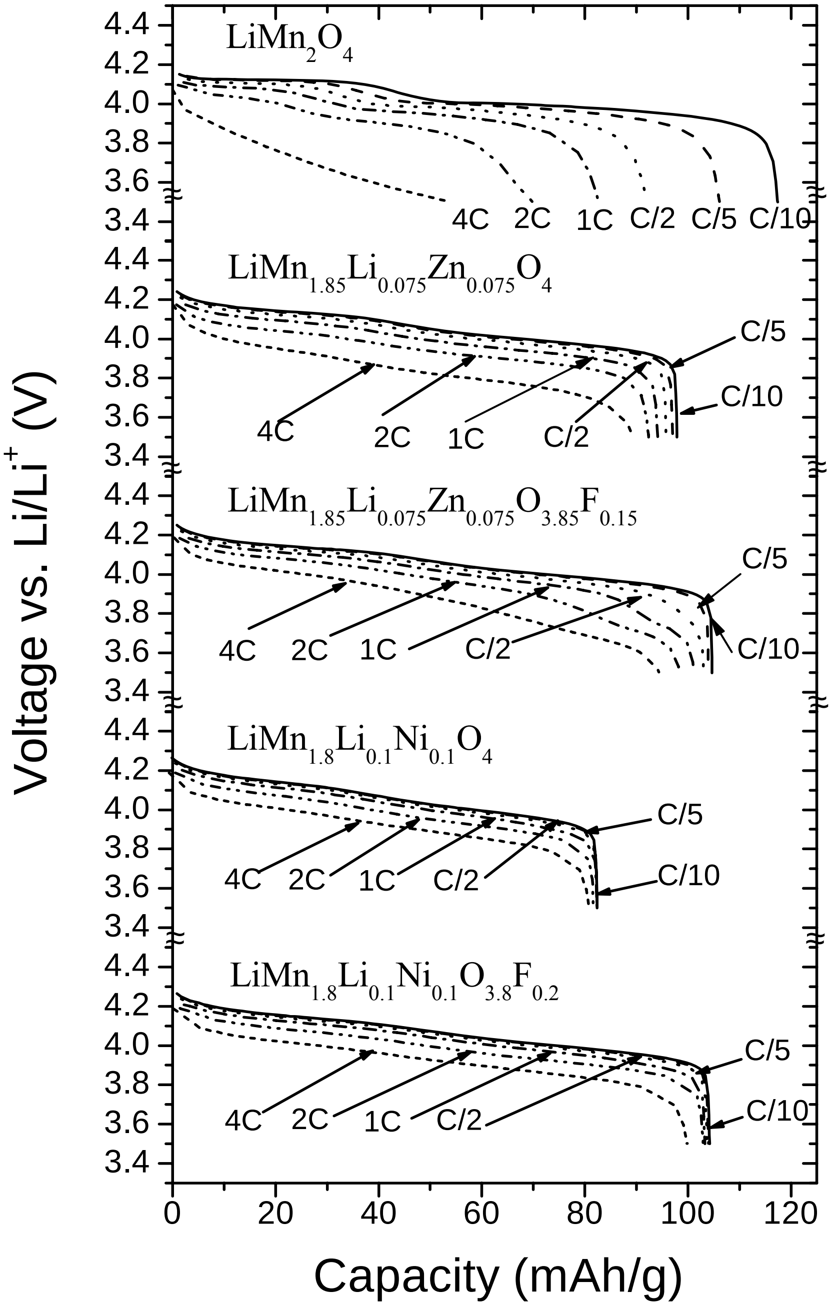

Figure 4.3 Comparison of the discharge profiles at various C rates, illustrating the rate capabilities of $LiMn_{2-y-z}Li_yZn_zO_{4-\eta}F_\eta$.

4.3.4 Manganese Dissolution, Lattice Parameter Mismatch in the Two Phase Region, and Capacity Fade

The Mn dissolution and cubic to cubic phase transition that occurs around (1-x) ≈ 0.30 to 0.45 in $LiMn_{2-y-z}Li_yZn_zO_{4-\eta}F_\eta$ during the charge-discharge process of the cathodes were investigated. Mn dissolution was evaluated with AAS by soaking the parent cathode powders in the electrolyte at 55 ^{o}C for 7 days while the cubic to cubic transition was followed by determining the lattice parameter difference Δa between the two cubic phases formed during chemical delithiation with NO_2BF_4 as described in the experimental section. The % manganese dissolution and the % volume change obtained from the lattice parameter difference Δa between the cubic phases formed around (1-x) ≈ 0.30 to 0.45 are given in Table 4.1. Both the cation substituted oxides and oxyfluorides show much lower manganese dissolution and instantaneous volume change compared to $LiMn_2O_4$ as has been found in the previous chapter.[157,158] Also, for a given cationic substitution, the fluorine substitution leads to a further decrease in both manganese dissolution and instantaneous volume change. Figure 4.4 shows the relationships among manganese dissolution, lattice parameter change Δa, and capacity fade. It is clear that the capacity fade decreases with both decreasing Δa and degree of manganese dissolution, suggesting that the reduced interfacial lattice strain due to the smaller Δa in the two-phase region as well as the suppressed manganese dissolution lead to improved capacity retention.[157]

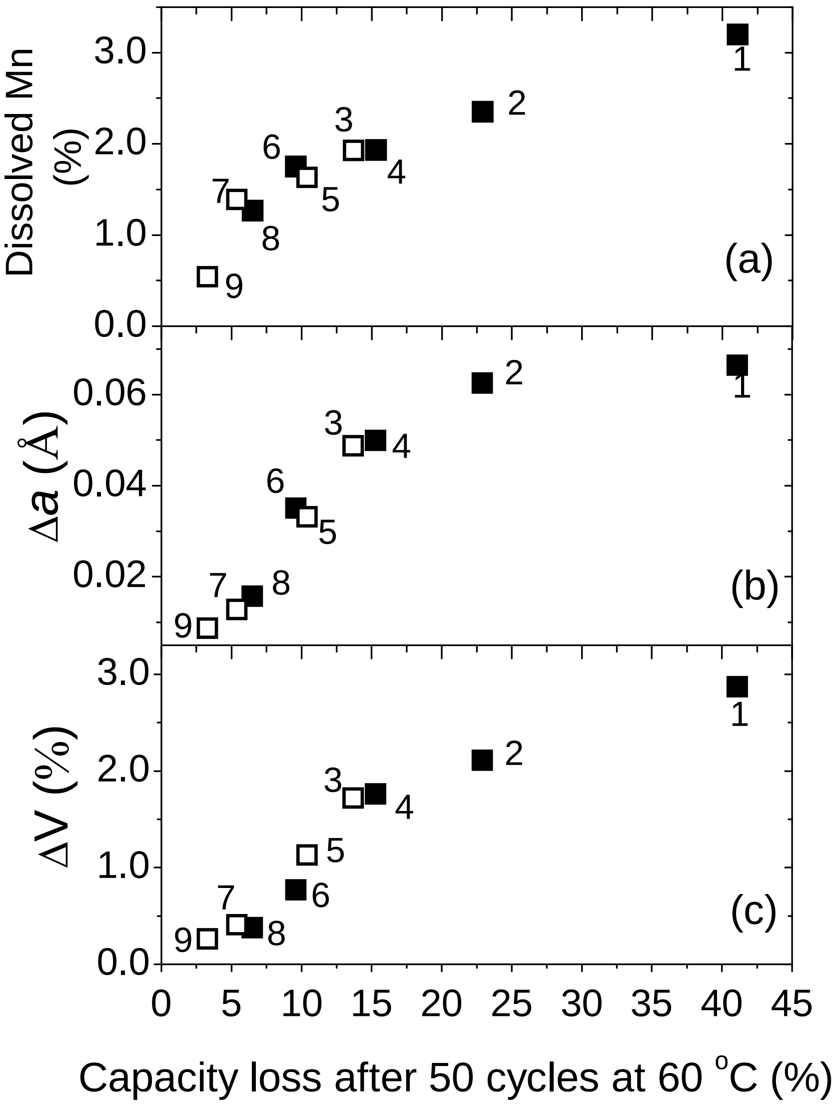

Figure 4.4 Correlation of the capacity fade in 50 cycles at 60 °C to the (a) degree of manganese dissolution, (b) lattice parameter difference Δa between the two cubic phases formed during the charge-discharge process, and (c) % volume change calculated from Δa. Closed and open squares refer, respectively, to the oxide and oxyfluoride cathodes. The numbers refer to the sample numbers in Table 4.1.

4.3.5 Microstrain Analysis

In general, several factors caused by instrument and sample could result in the broadening of peaks in X-ray diffraction.[149,159] For example, instrumental factors can influence the resolution and the incident X-ray wavelength while sample factors such as crystallite size and nonuniform microstrain can contribute to line broadening. The combined effect of crystallite size and microstrain on the full width at half maximum (FWHM) can be obtained by combining the Scherrer's equation for crystallite size effect and Bragg's law for diffraction to give

$$\beta \cos \theta = \lambda / \tau + k \varepsilon \sin \theta \qquad [4.1]$$

where β is the FWHM, λ is the incident X-ray wavelength, k is a constant, ε is the microstrain , and τ is crystallite size. The crystallite size and strain effects on line broadening can be separated by plotting $\beta \cos \theta$ versus $\sin \theta$, in which the slope $k\varepsilon$ is related to microstrain and the intercept λ/τ is related to the crystallite size.

Figure 4.5 compares the crystallite size and strain analyses of $Li_{1-x}Mn_2O_4$, $Li_{1-x}Mn_{1.85}Li_{0.075}Zn_{0.075}O_4$, and $Li_{1-x}Mn_{1.85}Li_{0.075}Zn_{0.075}O_{3.85}F_{0.15}$ before and after chemically extracting lithium or storing the parent or chemically delithiated samples in the electrolyte for 7 days at 55 °C. The nearly similar values of intercepts before and after the above treatments or processes for all the three systems shown in Fig. 4.5 indicate that the crystallite size of the spinel cathodes does not change significantly during such treatments. In contrast, the slope of the $Li_{1-x}Mn_2O_4$ system becomes steeper after such treatments compared to those of the cation-substituted spinel oxides and oxyfluorides $Li_{1-x}Mn_{1.85}Li_{0.075}Zn_{0.075}O_4$ and $Li_{1-x}Mn_{1.85}Li_{0.075}Zn_{0.075}O_{3.85}F_{0.15}$, suggesting that the $LiMn_2O_4$ system experiences a larger amount of microstrain during charging or storage in the electrolyte at elevated temperatures, which is consistent with earlier findings.[104] Both the larger lattice parameter difference between the two cubic phases formed during chemical delithiation and a larger manganese dissolution from the lattice lead to a larger microstrain. Moreover, for a given cationic substitution, the fluorine-substituted $LiMn_{1.85}Li_{0.075}Zn_{0.075}O_{3.85}F_{0.15}$ exhibits a smaller change in slope after the treatments compared to the oxide analog $LiMn_{1.85}Li_{0.075}Zn_{0.075}O_4$ due to both suppressed manganese dissolution and a smaller lattice parameter difference between the two cubic phases and the consequent lower microstrain.

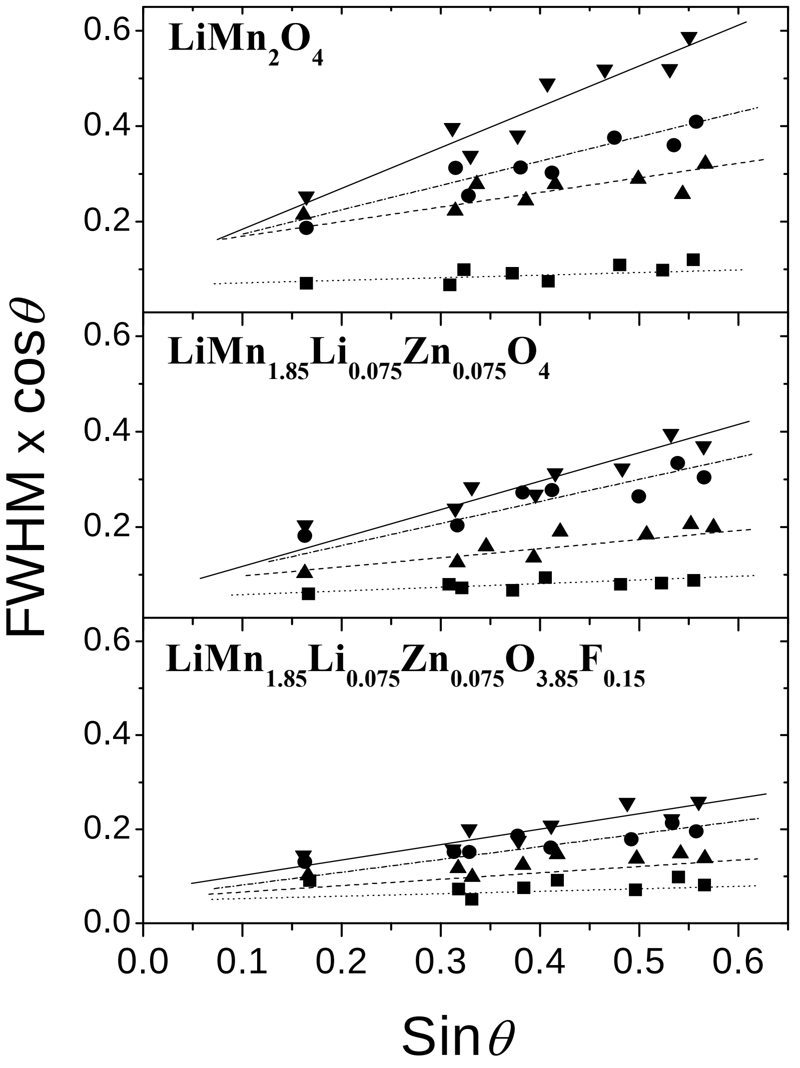

Figure 4.5 Crystallite size and strain analyses of $Li_{1-x}Mn_{2-y-z}Li_yZn_zO_{4-\eta}F_\eta$ spinel cathodes: (■) as-prepared samples before treatment, (▲) after chemical delithiation with NO_2BF_4, ($Li_{0.11}Mn_2O_4$, $Li_{0.38}Mn_{1.85}Li_{0.075}Zn_{0.075}O_4$, and $Li_{0.24}Mn_{1.85}Li_{0.075}Zn_{0.075}O_{3.85}F_{0.15}$), (●) after soaking the parent samples in the electrolyte at 55 °C for 7 days, and (▼) after soaking the chemically delithiated samples ($Li_{0.11}Mn_2O_4$, $Li_{0.38}Mn_{1.85}Li_{0.075}Zn_{0.075}O_4$, and $Li_{0.24}Mn_{1.85}Li_{0.075}Zn_{0.075}O_{3.85}F_{0.15}$) in the electrolyte at 55 °C for 7 days.

4.3.6 Loss of Crystallinity

Figure 4.6 compares the XRD patterns of $LiMn_2O_4$, $LiMn_{1.85}Li_{0.075}Zn_{0.075}O_4$, and $LiMn_{1.85}Li_{0.075}Zn_{0.075}O_{3.85}F_{0.15}$ electrodes after 50 cycles at 60 ^oC. While both the $LiMn_{1.85}Li_{0.075}Zn_{0.075}O_4$ and $LiMn_{1.85}Li_{0.075}Zn_{0.075}O_{3.85}F_{0.15}$ electrodes maintain good crystallinity, the $LiMn_2O_4$ electrode suffers from a significant loss in crystallinity on cycling at 60 ^oC. Also, for a given cationic substitution, the fluorine-substituted $LiMn_{1.85}Li_{0.075}Zn_{0.075}O_{3.85}F_{0.15}$ shows sharper diffraction peaks after cycling compared to the oxide analog $LiMn_{1.85}Li_{0.075}Zn_{0.075}O_4$ due to a reduced Δa and manganese dissolution. The loss of crystallinity on cycling may also perturb or hinder the three-dimensional diffusion of lithium ions in the spinel lattice and consequently lead to increased polarization losses and capacity fade arising from impedance growth.[100,130]

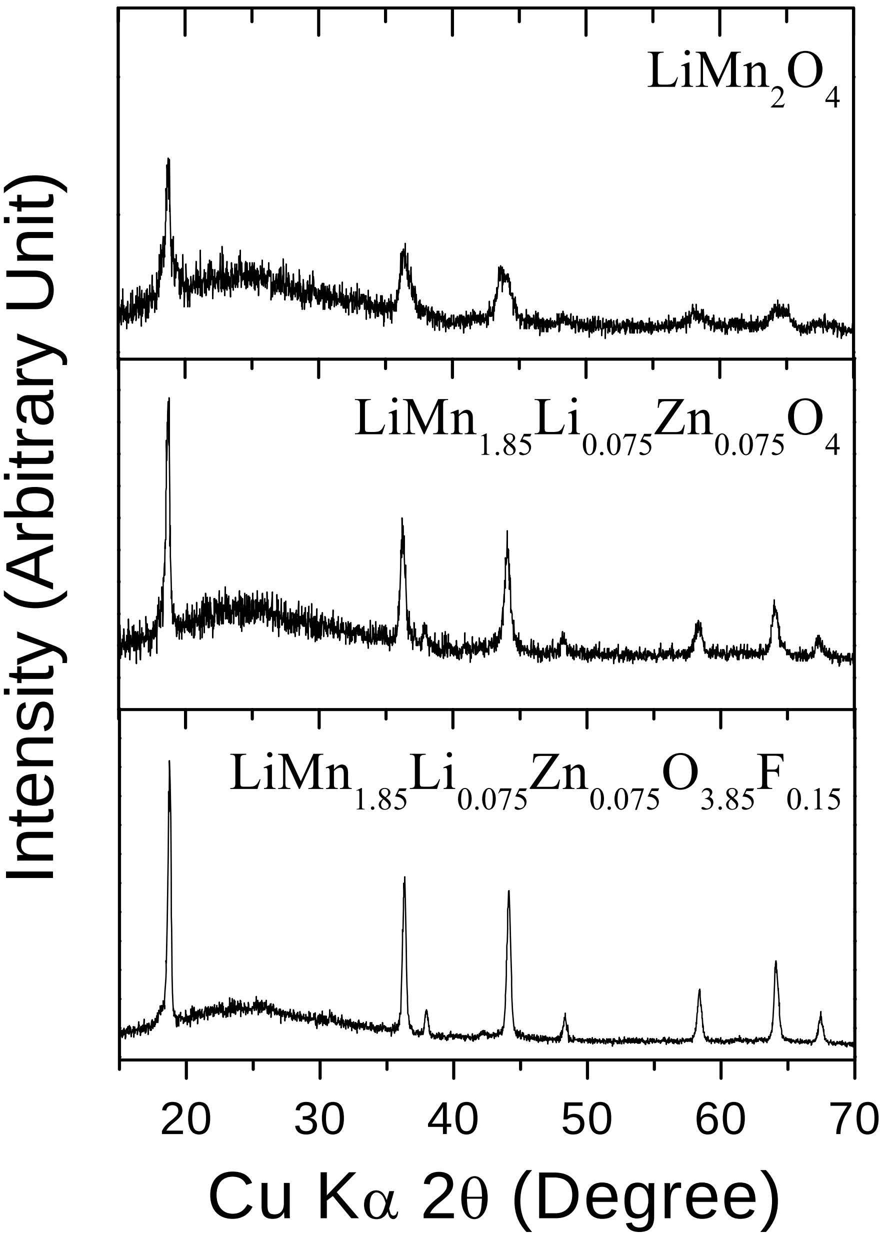

Figure 4.6 XRD patterns of $LiMn_{2-y-z}Li_yZn_zO_{4-\eta}F_\eta$ spinel cathodes after 50 cycles at 60 °C.

4.3.7 Area Specific Impedance Evaluation

To assess the impact of loss of crystallinity on electrochemical performance, the area specific impedance (ASI) of the $LiMn_2O_4$, $LiMn_{1.85}Li_{0.075}Zn_{0.075}O_4$, and $LiMn_{1.85}Li_{0.075}Zn_{0.075}O_{3.85}F_{0.15}$ cathodes was evaluated and compared before and after cycling at 60 °C, employing the PNGV L-HPPC test with an 18-s pulse discharge at 5C rate and 2-s pulse charge at 3.75C rate at room temperature as a function of the depths of discharge (DOD).[160] Although all the three samples have a similar ASI value of 25-35 $\Omega\cdot cm^2$ at 50 % DOD before cycling, the ASI value increases to 120, 94, and 82 $\Omega\cdot cm^2$, respectively, for $LiMn_2O_4$, $LiMn_{1.85}Li_{0.075}Zn_{0.075}O_4$, and $LiMn_{1.85}Li_{0.075}Zn_{0.075}O_{3.85}F_{0.15}$ after cycling at 60 °C, possibly due to changes in electrode kinetics, lithium ion diffusion, and ohmic drop (Fig. 4.7).[161] A smaller rise in ASI for the cation-substituted spinel oxide and oxyfluoride translates into better electrochemical performances compared to that of $LiMn_2O_4$. Amine *et al*[162] have recently suggested that the reduction of the dissolved manganese ions at the graphite/electrolyte interface results in the increase of charge-transfer impedance in lithium ion cell. However, the data in Fig. 4.7 suggest that the loss of crystallinity, microstrain, and manganese dissolution at the cathode could also contribute to the impedance growth in addition to the reduction of manganese ions at the carbon anode.

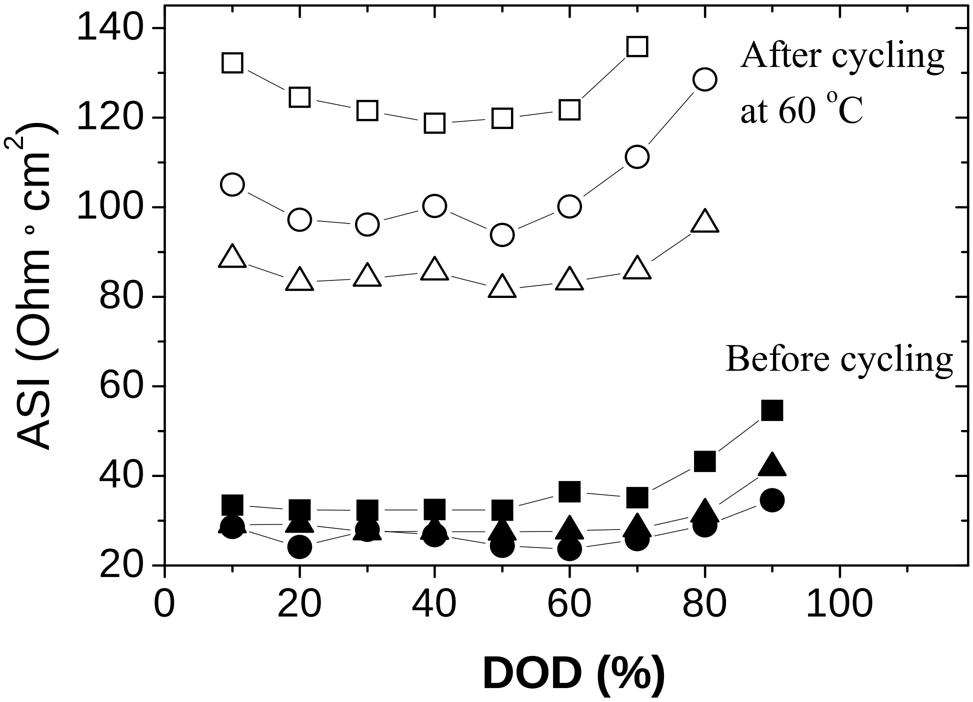

Figure 4.7 Area specific impedance (ASI) of $LiMn_{2-y-z}Li_yZn_zO_{4-\eta}F_\eta$ spinel cathodes as a function of depth of discharge (DOD) before and after 50 cycles at 60 °C. Closed and open symbols refer, respectively, to the cathodes before cycling and after cycling at 60 °C: (■) $LiMn_2O_4$, (●) $LiMn_{1.85}Li_{0.075}Zn_{0.075}O_4$, and (▲) $LiMn_{1.85}Li_{0.075}Zn_{0.075}O_{3.85}F_{0.15}$.

4.4 CONCLUSIONS

The electrochemical performances of the $LiMn_{2-y-z}Li_yZn_zO_{4-\eta}F_\eta$ spinel oxyfluoride cathodes have been compared with those of the oxide analogs $LiMn_{2-y-z}Li_yZn_zO_4$ as well as $LiMn_2O_4$. The oxyfluorides exhibit up to 10 mAh/g higher capacity than the corresponding oxide analogs due to a decrease in the initial manganese valence with an enhanced capacity retention. The better electrochemical performances of the $LiMn_{2-y-z}Li_yZn_zO_{4-\eta}F_\eta$ oxyfluoride cathodes are due to suppressed manganese dissolution and a smaller instantaneous volume change between the two cubic phases formed during the charge-discharge process. A large instantaneous volume change and high manganese dissolution are believed to cause interfacial strain and loss of crystallinity on cycling, which leads to impedance growth and capacity fade, for example, in the conventional $LiMn_2O_4$ spinel cathode. Optimized oxyfluoride compositions such as $LiMn_{1.85}Li_{0.075}Zn_{0.075}O_{3.85}F_{0.15}$ exhibit excellent capacity retention at elevated temperatures with capacities of over 100 mAh/g. Although fluorine substitution using ZnF_2 is more effective in controlling the volatility of fluorine during synthesis compared to fluorine incorporation using LiF as a fluorine source, the volatility of fluorine at high temperatures still remains to be solved.

CHAPTER 5

FLUORINE SUBSTITUTION WITH A LOW TEMPERATURE METHOD AND ELECTROCHEMICAL PERFORMANCES OF SPINEL OXYFLUORIDES

5.1 INTRODUCTION

To improve the electrochemical performances of spinel cathodes, extensive investigations such as cationic substitutions,[109-126] anionic substitutions,[135-146] and surface treatments[130–134] have been carried out. Among them, substituting lithium or other transition metals for manganese significantly improves the cyclability of spinel cathodes by reducing the manganese dissolution and suppressing the lattice parameter mismatch between the two cubic phases formed during the charge-discharge process. However, substitution of lower valent cations in spinel cathodes increases the average oxidation state of Mn and decreases the reversible capacity compared to the unsubstituted ones. In this regard, simultaneous cationic and anionic substitutions become attractive since replacement of the divalent oxygen ions by the monovalent fluorine ions can compensate for the capacity decrease caused by cationic substitutions.

Although the electrochemical performances of spinel cathodes could be improved by fluorine substitution using LiF or ZnF_2 as fluorine source as shown in the previous chapters, synthesis at high temperatures (800 ^{o}C) poses difficulties in controlling the fluorine contents incorporated into the spinel lattice due to the volatilization of fluorine, while the Zn ions located in tetrahedral sites of the spinel lattice degrade the rate capability of the spinel cathodes.

In this chapter, a low temperature procedure involving the firing of the already synthesized cation-substituted spinel oxides $LiMn_{2-y-z}Li_yM_zO_4$ with ammonium hydrogen fluoride (NH_4HF_2) at 450 °C is investigated systematically in order to maximize the fluorine content and identify the factors controlling the amount of fluorine that could be incorporated into the spinel lattice. An investigation of the electrochemical performance factors such as capacity retention at ambient and elevated temperatures, rate capability, storage characteristics, and irreversible capacity loss in the first cycle is presented. Furthermore, the relationships among capacity fade, manganese dissolution, and lattice mismatch between the two cubic phased formed during the charge-discharge process are discussed.

5.2 EXPERIMENTAL

The cation-substituted $LiMn_{2-y-z}Li_yM_zO_4$ (M = Ti and Ni) spinel oxides were synthesized by firing required amounts of Li_2CO_3 and Mn_2O_3 with TiO_2 or NiO at 800 °C for 48 h in air. The fluorine incorporation was achieved by firing the $LiMn_{2-y-z}Li_yM_zO_4$ spinel oxides with a required amount of NH_4HF_2 at 450 °C for 5 h in air to give the $LiMn_{2-y-z}Li_yM_zO_{4-\eta}F_\eta$ oxyfluorides. All the samples were characterized by X-ray diffraction (XRD). The lithium contents in the products and the average oxidation state of manganese were determined by atomic absorption spectroscopy (AAS) and a redox titration involving sodium oxalate and potassium permanganate. In order to assess the degree of lattice mismatch between the two cubic phases formed, lattice parameter determinations were carried out with the chemically delithiated samples by analyzing the XRD data with the Rietveld method.[149] The chemical delithiation was carried out by stirring the $LiMn_{2-y-z}Li_yM_zO_{4-\eta}F_\eta$ powder with an acetonitrile solution of the oxidizer NO_2BF_4 for 2 days under argon atmosphere, followed by washing the products with acetonitrile as given in chapter 2.[31] The degree of manganese dissolution was assessed by soaking the parent spinel sample powders in the electrolyte containing 1 M $LiPF_6$ in 1:1 ethylene carbonate (EC) and diethyl carbonate (DEC) at 55 °C for 7 days and determining the amount of manganese in the electrolyte with AAS. The cathodes for evaluating the electrochemical performances were prepared as described in chapter 2, and the electrochemical performance evaluations were carried out with CR 2032 coin cells.

5.3 RESULTS AND DISCUSSION

5.3.1 Crystal Chemistry

Since there is a possibility of volatilization of fluorine even at the low fluorination temperature of 450 °C, the fluorine contents in the synthesized samples were calculated based on the lithium contents and oxidation state of manganese values obtained, respectively, from the AAS and redox titration data by employing the charge neutrality principle and assuming the total anion (O + F) content to be 4.0. Table 5.1 summarizes the oxidation state values of manganese and the experimentally determined compositions. The fluorine incorporation leads to a decrease in the oxidation state of manganese, confirming the substitution of monovalent F^- ions for divalent O^{2-} ions. While the conventional high temperature (850 °C) synthesis with LiF[137,138,140] encounters a volatilization of fluorine and limits the fluorine contents, the low temperature approach employing NH_4HF_2 was found to overcome this difficulty, and we have been able to incorporate fluorine contents of up to η = 0.29 into the $LiMn_{1.8}Li_{0.1}Ni_{0.1}O_{3.71}F_{0.29}$ spinel lattice as seen in Table 5.1.

Figure 5.1 compares the XRD patterns of some spinel oxide and oxyfluoride compositions. While the incorporation of fluorine contents as little as 0.08 into $LiMn_2O_4$ results in the formation of the impurity phase Mn_5O_8, fluorine contents up to 0.29 could be achieved with the cation-substituted $LiMn_{1.8}Li_{0.1}Ni_{0.1}O_{4-\eta}F_\eta$ ($0 \leq \eta \leq 0.29$) without any impurity phases. Attempts to increase the fluorine content further in $LiMn_{1.8}Li_{0.1}Ni_{0.1}O_{4-\eta}F_\eta$ resulted in the formation of Mn_5O_8 impurity phase as seen in the case of $LiMn_{1.8}Li_{0.1}Ni_{0.1}O_{3.62}F_{0.38}$. The formation of impurity phase at higher fluorine contents could be related to the difficulty of lowering the oxidation state of Mn below about 3.5+ in the spinel lattice. This conclusion is supported by the fact that the Mn_5O_8 impurity phase is formed even at much lower fluorine contents of 0.08 in $LiMn_2O_{3.92}F_{0.08}$, 0.18 in $LiMn_{1.9}Ni_{0.1}O_{3.82}F_{0.18}$, and 0.2 in $LiMn_{1.9}Li_{0.05}Ni_{0.05}O_{3.8}F_{0.2}$ as the oxidation state of manganese is at or below 3.5+ in these cases. Table 5.1 also gives the lattice parameter values of the various spinel compositions synthesized.

With a given cationic substitution, the lattice parameter value increases with increasing fluorine substitution, confirming the reduction of the smaller Mn^{4+} ions into larger Mn^{3+} ions and a replacement of O^{2-} ions by F^{-} ions in the bulk spinel lattice. Scanning electron microscopy (SEM) revealed that all the spinel oxide and oxyfluoride samples synthesized have similar particle size and morphologies while XRD indicated crystallite sizes of 50 – 85 nm.

Table 5.1 Chemical, structural, and electrochemical characterization data of spinel manganese oxyfluorides.

Sample number	Composition[a]	Mn valence[b]	Lattice parameter (Å)	Initial capacity (mAh/g)	Capacity loss in 50 cycles (%)		IRC in first cycle[c] (mAh/g)	Mn dissolution[d] (%)
					25 °C	60 °C		
1	$LiMn_2O_4$	3.50	8.2451	119	35.2	53.5	12.1	3.2
2	$LiMn_2O_{3.92}F_{0.08}$	3.46	8.2497	119	29.4	43.3	11.5	2.6
3	$LiMn_{1.9}Ni_{0.1}O_4$	3.58	8.2265	117	10.8	16.1	7.0	2.0
4	$LiMn_{1.9}Ni_{0.1}O_{3.9}F_{0.1}$	3.53	8.2339	121	7.1	9.5	6.2	1.7
5	$LiMn_{1.9}Ni_{0.1}O_{3.82}F_{0.18}$	3.48	8.2395	-	-	-	-	-
6	$LiMn_{1.9}Li_{0.05}Ni_{0.05}O_4$	3.61	8.2197	111	5.9	11.3	5.1	1.8
7	$LiMn_{1.9}Li_{0.05}Ni_{0.05}O_{3.9}F_{0.1}$	3.55	8.2284	117	4.1	8.8	4.8	1.7
8	$LiMn_{1.9}Li_{0.05}Ni_{0.05}O_{3.8}F_{0.2}$	3.50	8.2362	-	-	-	-	-
9	$LiMn_{1.8}Li_{0.1}Ni_{0.1}O_4$	3.72	8.2091	82	1.1	2.6	2.4	1.1
10	$LiMn_{1.8}Li_{0.1}Ni_{0.1}O_{3.9}F_{0.1}$	3.67	8.2138	90	0.9	2.1	1.2	0.6
11	$LiMn_{1.8}Li_{0.1}Ni_{0.1}O_{3.8}F_{0.2}$	3.61	8.2252	104	0.9	1.9	0.9	0.8
12	$LiMn_{1.8}Li_{0.1}Ni_{0.1}O_{3.71}F_{0.29}$	3.56	8.2338	110	4.5	7.8	2.5	1.4
13	$LiMn_{1.8}Li_{0.1}Ni_{0.1}O_{3.62}F_{0.38}$	3.51	8.2391	-	-	-	-	-
14	$LiMn_{1.8}Li_{0.1}Ti_{0.1}O_4$	3.61	8.2142	103	19.2	28.5	6.7	2.5
15	$LiMn_{1.8}Li_{0.1}Ti_{0.1}O_{3.9}F_{0.1}$	3.56	8.2191	109	11.3	20.4	7.7	1.9

[a] The electrochemical and Mn dissolution data are not given for samples that contain the Mn_5O_8 impurity phase.

[b] Calculated by assuming Li^+, Ti^{4+}, Ni^{2+}, and F^-.

[c] Irreversible capacity loss between the first charge and discharge.

[d] % Mn dissolution in the two-phase region based on sample weight.

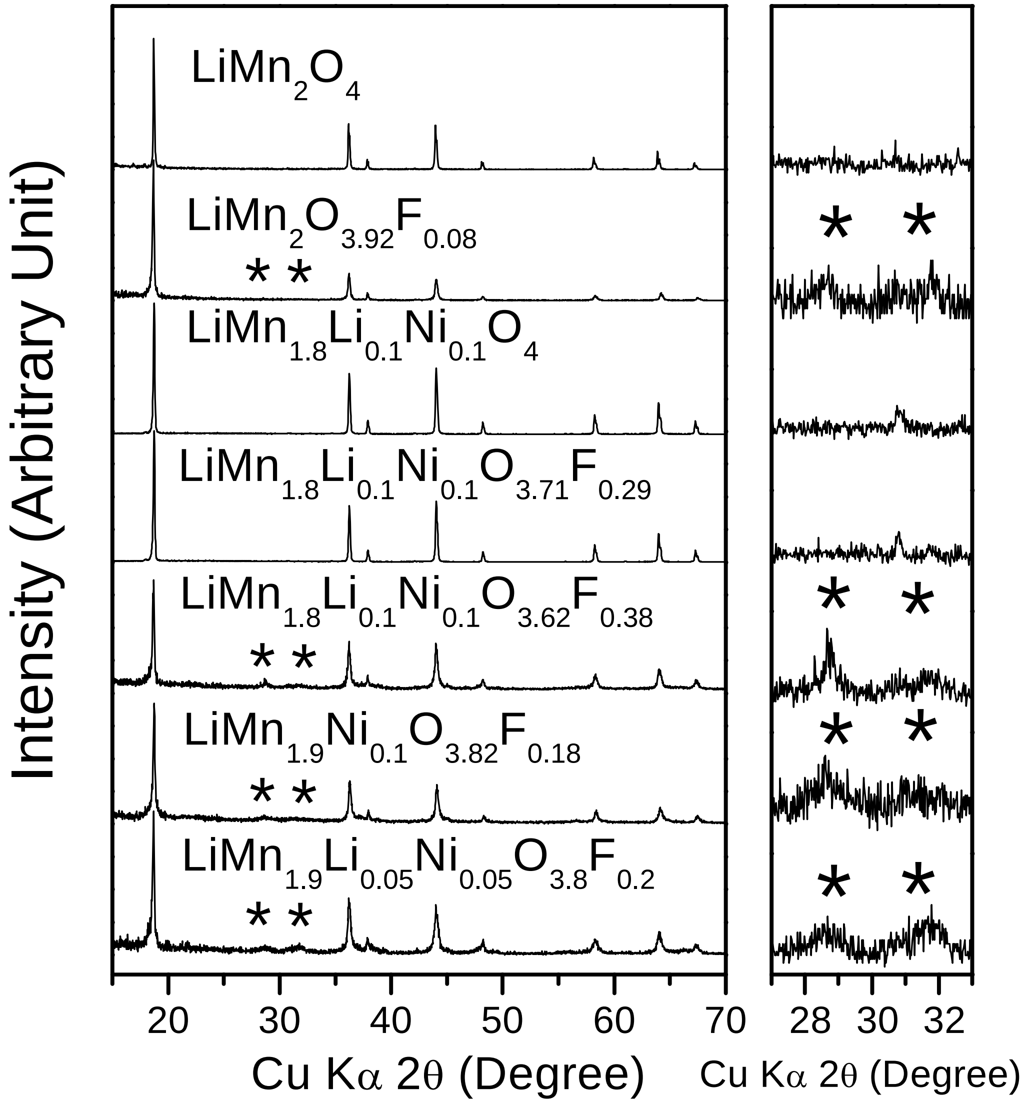

Figure 5.1 XRD patterns of the LiMn$_{2-y-z}$Li$_y$Ni$_z$O$_{4-\eta}$F$_\eta$ samples. The reflections marked with * refer to Mn$_5$O$_8$ impurity phase.

5.3.2 Cycling Performance

Figure 5.2 compares the cyclability data of the $LiMn_{2-y-z}Li_yNi_zO_{4-\eta}F_\eta$ cathodes at room temperature and 60 ^oC at C/5 rate. The initial capacity values and the % capacity loss after 50 cycles at 25 and 60 ^oC are summarized in Table 5.1. With a given cationic substitution, the initial capacity value increases with increasing fluorine substitution due to a lowering of the oxidation state of manganese. For example, an increase of 28 mAh/g could be achieved on going from $LiMn_{1.8}Li_{0.1}Ni_{0.1}O_4$ (82 mAh/g) to $LiMn_{1.8}Li_{0.1}Ni_{0.1}O_{3.71}F_{0.29}$ (110 mAh/g). Furthermore, the spinel oxyfluorides exhibit an improvement in capacity retention at both 25 and 60 ^oC compared to the oxide analogs and $LiMn_2O_4$. For example, $LiMn_{1.8}Li_{0.1}Ni_{0.1}O_4$ and $LiMn_{1.8}Li_{0.1}Ni_{0.1}O_{3.8}F_{0.2}$ exhibit capacity fades of, respectively, 2.6 and 1.9 % in 50 cycles at 60 ^oC compared to ~ 50 % fade for $LiMn_2O_4$. However, a further increase in fluorine content on going from $LiMn_{1.8}Li_{0.1}Ni_{0.1}O_{3.8}F_{0.2}$ to $LiMn_{1.8}Li_{0.1}Ni_{0.1}O_{3.71}F_{0.29}$ causes a significant increase in capacity fade from 1.9 to 7.8 % at 60 ^oC. The decline in capacity retention at much higher fluorine contents could be related to the decrease in the oxidation state of manganese close to 3.5+ and the consequent dynamic Jahn-Teller distortions over short atomic distances. Additionally, both $LiMn_{1.8}Li_{0.1}Ti_{0.1}O_4$ and $LiMn_{1.8}Li_{0.1}Ti_{0.1}O_{3.9}F_{0.1}$ exhibit higher capacity fade than, respectively, the analogous $LiMn_{1.8}Li_{0.1}Ni_{0.1}O_4$ and $LiMn_{1.8}Li_{0.1}Ni_{0.1}O_{3.9}F_{0.1}$ cathodes despite the same degree of cationic substitutions, illustrating the differences in the effectiveness of various substituents. The difference is due to a lower initial manganese valence in the former series arising from a substitution of Ti^{4+} vs Ni^{2+} and the accompanying differences in other parameters (see later).

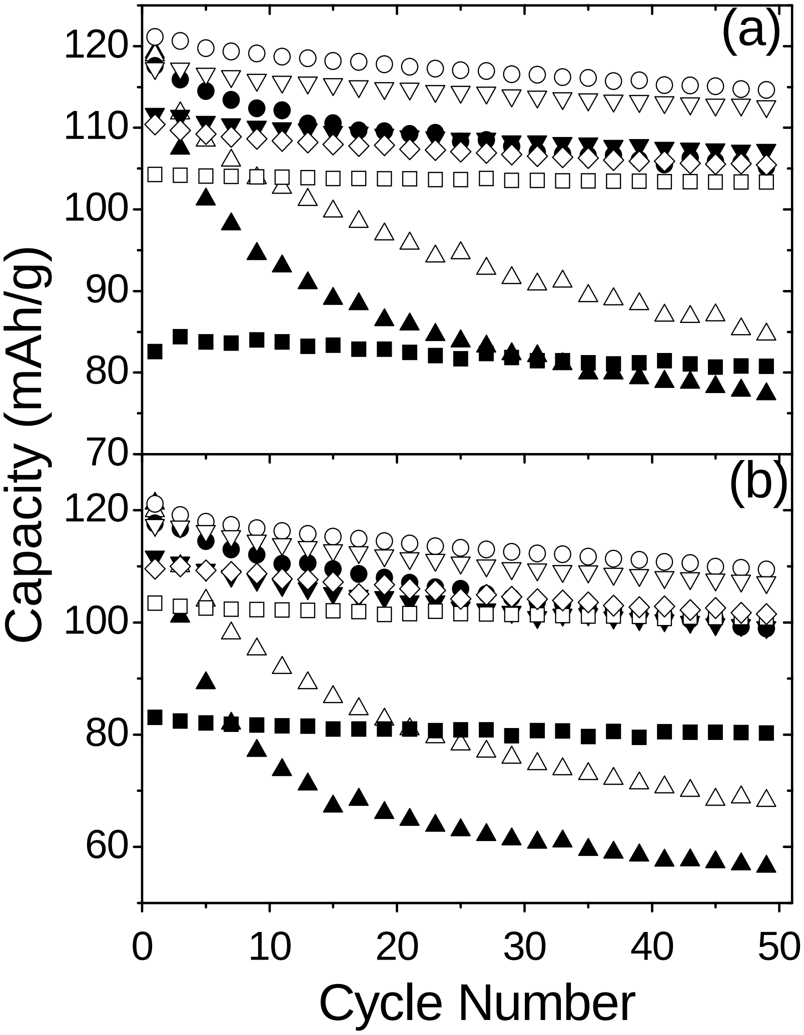

Figure 5.2 Comparison of the electrochemical cycling performances at (a) 25 °C and (b) 60 °C of $LiMn_{2-y-z}Li_yNi_zO_{4-\eta}F_\eta$: (▲) $LiMn_2O_4$, (△) $LiMn_2O_{3.92}F_{0.08}$, (●) $LiMn_{1.9}Ni_{0.1}O_4$, (○) $LiMn_{1.9}Ni_{0.1}O_{3.9}F_{0.1}$, (▼) $LiMn_{1.9}Li_{0.05}Ni_{0.05}O_4$, (▽) $LiMn_{1.9}Li_{0.05}Ni_{0.05}O_{3.9}F_{0.1}$, (■) $LiMn_{1.8}Li_{0.1}Ni_{0.1}O_4$, (□) $LiMn_{1.8}Li_{0.1}Ni_{0.1}O_{3.8}F_{0.2}$, and (◇) $LiMn_{1.8}Li_{0.1}Ni_{0.1}O_{3.71}F_{0.29}$.

5.3.3 Rate Capability

Figure 5.3 compares the discharge profiles of some selected spinel oxide and oxyfluorides compositions to illustrate the rate capability. The profiles were recorded by charging the cathodes at the same rate of C/10 and discharging at different rates of C/10 to 4C at room temperature. While all the cation-substituted samples exhibit better rate capabilities than $LiMn_2O_4$, for the same degree of cationic substitution, the doubly substituted $LiMn_{1.9}Li_{0.05}Ni_{0.05}O_4$ shows better rate capability than the singly substituted $LiMn_{1.9}Ni_{0.1}O_4$ as had been found before.[104] With a given cationic substitution, the fluorine substitution decreases the rate capability slightly, but it offers the important advantage of increasing the capacity. For example, while $LiMn_{1.8}Li_{0.1}Ni_{0.1}O_4$ retains 98 % of its capacity (82 mAh/g) on going from C/10 to 4C rate, $LiMn_{1.8}Li_{0.1}Ni_{0.1}O_{3.8}F_{0.2}$ retains 96 % of its capacity (104 mAh/g). However, further increase in fluorine content as in $LiMn_{1.8}Li_{0.1}Ni_{0.1}O_{3.71}F_{0.29}$ results in a much larger decline in rate capability, with a retention of only 85 % of its capacity (110 mAh/g) on going from C/10 to 4C rate. The decline in rate capability could also be related to a decrease in the initial Mn valence as seen in Table 5.1 and the consequent short range, dynamic Jahn-Teller distortions.

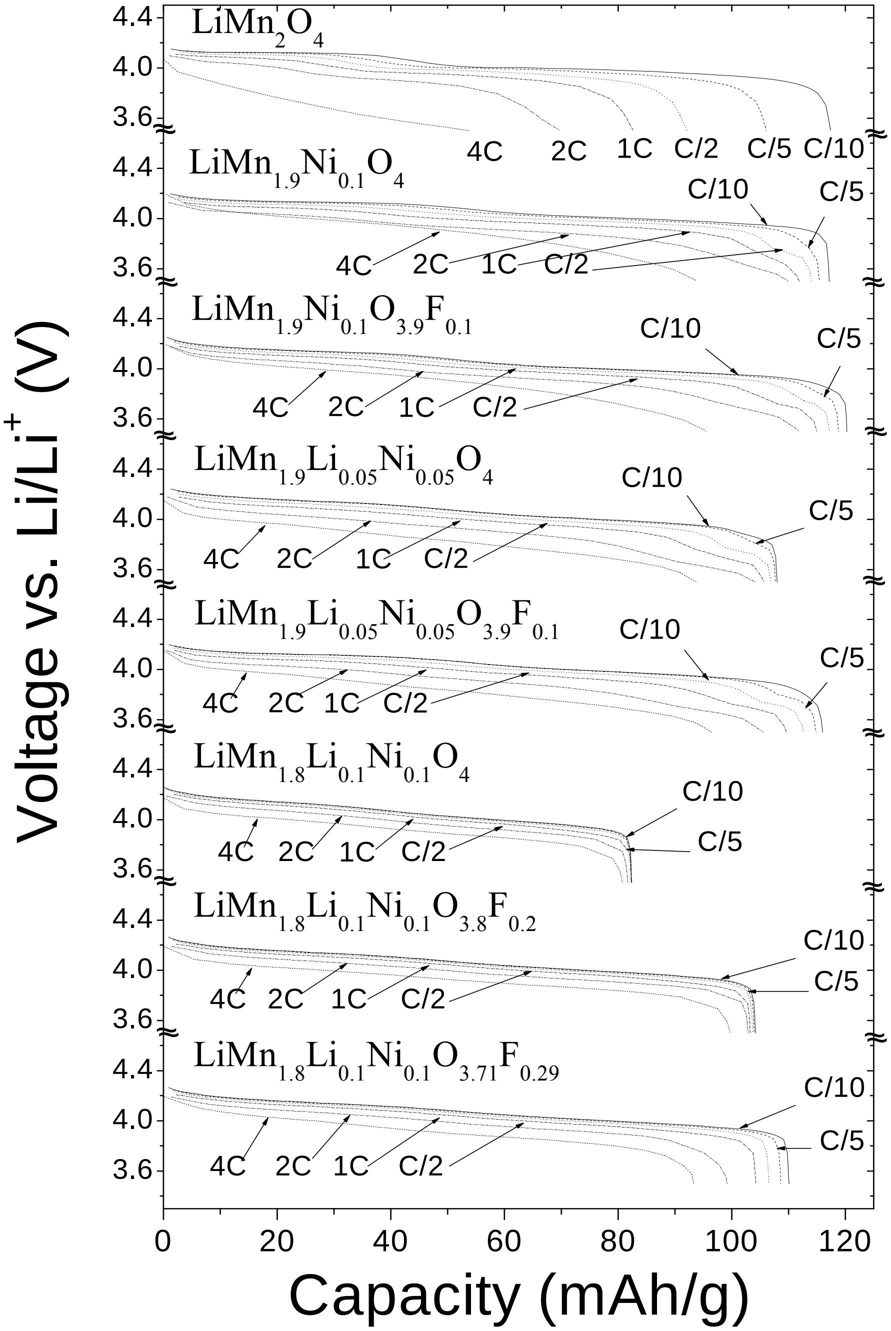

Figure 5.3 Comparison of the discharge profiles at various C rates, illustrating the rate capabilities of $LiMn_{2-y-z}Li_yNi_zO_{4-\eta}F_\eta$.

5.3.4 Storage Properties

Figure 5.4 compares the % capacity retention of the $LiMn_{2-y-z}Li_yM_zO_{4-\eta}F_\eta$ cathodes after storing at various depths of discharge (DOD). The storage performances were evaluated by subjecting the coin cells to one charge-discharge cycle at room temperature between 4.3 and 3.5 V, followed by discharging to various DOD in the second cycle, storing at 60 ^oC for 7 days at various DOD, completing the second discharge cycle after cooling to ambient temperature, and evaluating the full discharge capacity in the third cycle at room temperature. The % capacity retention in Fig. 5.4 was obtained as a ratio of the third discharge capacity to the first discharge capacity. Although $LiMn_2O_4$ loses a significant amount of capacity after storage (60-80% retention), the cation-substituted oxyfluoride $LiMn_{1.8}Li_{0.1}Ni_{0.1}O_{3.8}F_{0.2}$ retains > 97 % of its initial capacity, illustrating excellent storage characteristics. Similarly, the cation-substituted oxides $LiMn_{1.8}Li_{0.2}O_4$ and $LiMn_{1.8}Li_{0.1}Ni_{0.1}O_4$ and the oxyfluoride $LiMn_{1.8}Li_{0.2}O_{3.79}F_{0.21}$ also exhibit much better storage characteristics with > 93 % retention compared to $LiMn_2O_4$. In contrast, the cation-substituted oxide $LiMn_{1.8}Li_{0.1}Ti_{0.1}O_4$ and the oxyfluoride $LiMn_{1.8}Li_{0.1}Ti_{0.1}O_{3.9}F_{0.1}$ show only a moderate improvement (> 75 % retention) compared to $LiMn_2O_4$. Also, a much higher fluorine content in $LiMn_{1.8}Li_{0.1}Ni_{0.1}O_{3.71}F_{0.29}$ leads to a degradation in storage characteristics (> 90 % retention) compared to that in $LiMn_{1.8}Li_{0.1}Ni_{0.1}O_{3.8}F_{0.2}$ (> 97 % retention). The much less pronounced improvement in storage properties with the $LiMn_{1.8}Li_{0.1}Ti_{0.1}O_{4-\eta}F_\eta$ series and $LiMn_{1.8}Li_{0.1}Ni_{0.1}O_{3.71}F_{0.29}$ is due to a lower initial Mn valence and the accompanying differences in other parameters compared to that with the $LiMn_{1.8}Li_{0.1}Ni_{0.1}O_{4-\eta}F_{\eta}$ series (see later).

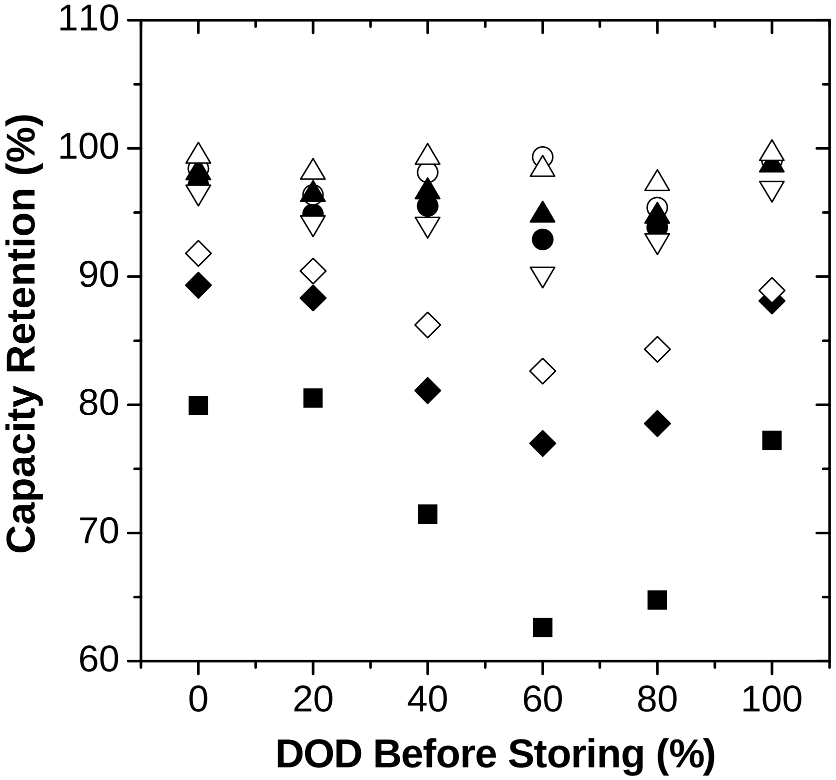

Figure 5.4 Comparison of the % capacity retention after storage at 60 °C for 7 days at different depth of discharge (DOD): (■) $LiMn_2O_4$, (●) $LiMn_{1.8}Li_{0.2}O_4$, (○) $LiMn_{1.8}Li_{0.2}O_{3.79}F_{0.21}$, (▲) $LiMn_{1.8}Li_{0.1}Ni_{0.1}O_4$, (△) $LiMn_{1.8}Li_{0.1}Ni_{0.1}O_{3.8}F_{0.2}$, (▽) $LiMn_{1.8}Li_{0.1}Ni_{0.1}O_{3.71}F_{0.29}$, (◆) $LiMn_{1.8}Li_{0.1}Ti_{0.1}O_4$, and (◇) $LiMn_{1.8}Li_{0.1}Ti_{0.1}O_{3.9}F_{0.1}$.

5.3.5 Irreversible Capacity in the First Cycle

Additionally, the irreversible capacity (IRC) loss between the first charge and discharge cycles is also an important performance factor since only the reversible capacity can be utilized in rechargeable batteries. Table 5.1 gives the IRC values, and Fig. 5.5 shows the relationship between IRC loss and capacity fade. The cation- and anion-substituted spinel cathodes show much lower IRC values compared to $LiMn_2O_4$, and the IRC value decreases with decreasing capacity fade. Thus, the oxyfluoride cathodes with optimum compositions offer a combination of excellent cyclability, rate capability, and storage characteristics along with low IRC values.

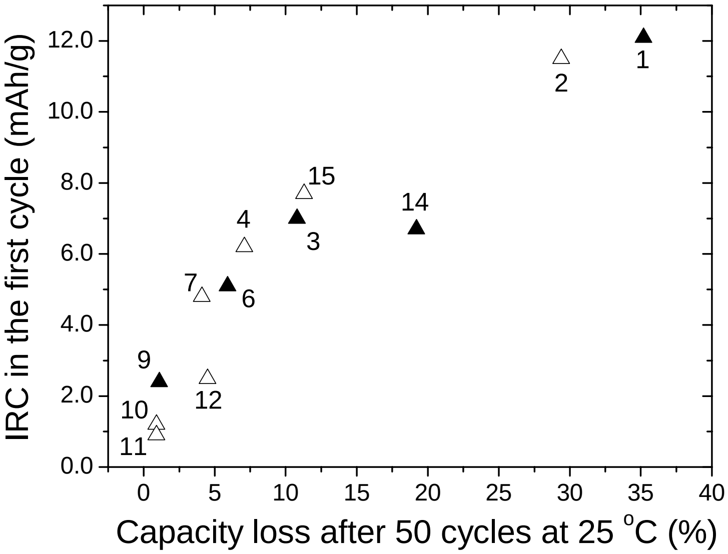

Figure 5.5 Comparison of the irreversible capacity in the first cycle with the % capacity loss in 50 cycles at room temperature. The numbers refer to the sample numbers in Table 5.1.

5.3.6 Initial Manganese Valence, Lattice Parameter Mismatch, and Manganese Dissolution

Figure 5.6a relates the initial manganese valence to the capacity fade after 50 cycles at room temperature. The capacity fade decreases with increasing manganese valence, and the samples with an initial manganese valence of above about 3.6+ exhibit excellent capacity retention. Figure 5.7 compares the XRD patterns of the $Li_{1-x}Mn_{2-y-z}Li_yNi_zO_{4-\eta}F_\eta$ ($0.34 \leq (1-x) \leq 0.41$) samples in the two-phase region that were obtained by chemical delithiation with an acetonitrile solution of NO_2BF_4. While $Li_{0.37}Mn_2O_4$ shows a clear splitting of the reflections due to a large lattice parameter difference Δa between the two cubic phases formed, the cation- and anion-substituted samples show a reduced separation between the reflections of the two cubic phases. Although a very small Δa results in a merger of the two reflections into a broad, single peak in cases like $Li_{1-x}Mn_{1.8}Li_{0.1}Ni_{0.1}O_{3.8}F_{0.2}$, the lattice parameters for the two cubic phases could be obtained by resolving the broad reflections using Rietveld analysis. Figures 5.6b and 5.6c correlate the lattice parameter difference Δa and the corresponding % volume change ΔV to the capacity fade after 50 cycles at room temperature. The capacity fade decreases with decreasing Δa and ΔV, demonstrating that a large lattice mismatch and the consequent interfacial strain lead to an increase in capacity fade. The instantaneous volume change of about 3 % on going from one cubic phase to another cubic phase in the case of $LiMn_2O_4$ is too large to maintain inter-particle contact during the charge-discharge cycle, resulting in severe capacity fade.

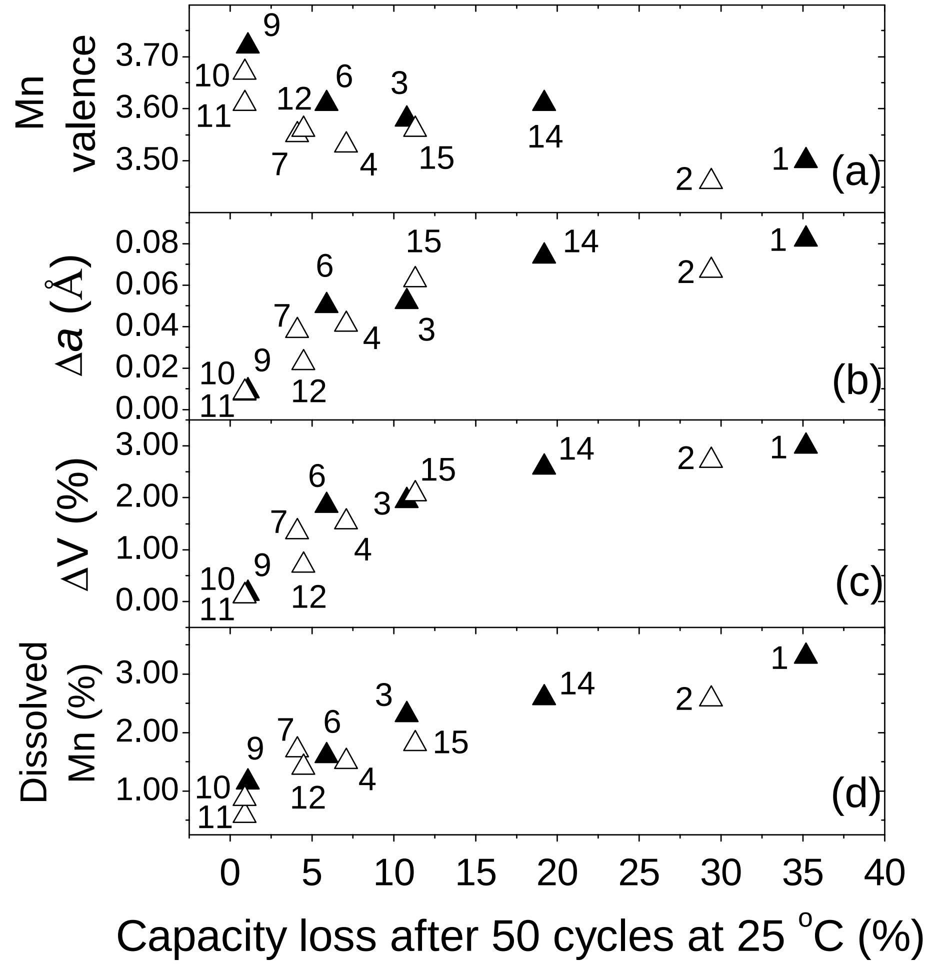

Figure 5.6 Correlation of the % capacity loss after 50 cycles at room temperature to the (a) initial Mn valence, (b) maximum lattice parameter difference Δ*a* between the two cubic phases formed during the charge-discharge process, (c) corresponding volume change ΔV calculated from Δ*a*, and (d) amount of Mn dissolution in the two-phase region. Closed and open triangles refer to, respectively, the oxide and oxyfluoride spinel cathodes. The numbers refer to the sample numbers in Table 5.1.

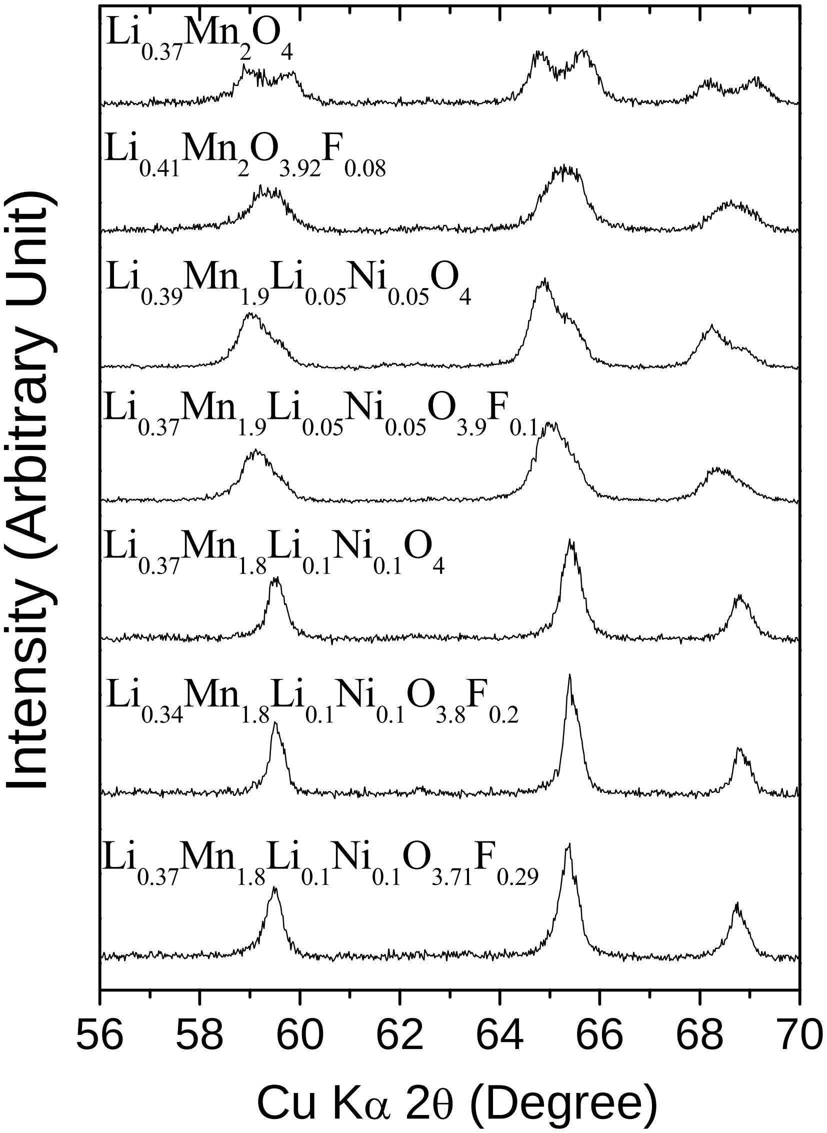

Figure 5.7 XRD patterns of the $Li_{1-x}Mn_{2-y-z}Li_yNi_zO_{4-\eta}F_\eta$ samples in the two-phase region consisting of two cubic phases. The samples were obtained by chemically extracting lithium with NO_2BF_4.

5.3.7 Relationship between Manganese Dissolution and Lattice Parameter Mismatch in the Two Phase Region

Figure 5.8 shows the relationship between Δa and Mn dissolution from the lattice in the two-phase region. Interestingly, the amount of Mn dissolution, which has been considered as a predominant source of capacity fade in spinel cathodes, decreases with decreasing Δa. Accordingly, the capacity fade decreases with both decreasing Mn dissolution and Δa as seen in Fig. 5.6. Figure 5.8 also shows the relationship between initial Mn valence and Δa. Above an initial Mn valence of about 3.6+, the Δa value remains small, resulting in excellent capacity retention, while the Δa value becomes large as the initial Mn valence decreases below 3.6+. The correlations in Figs. 5.6 and 5.8 also reveal that the inferior electrochemical performance (*e.g.* higher capacity fade and worse storage characteristics) of $LiMn_{1.8}Li_{0.1}Ti_{0.1}O_{4-\eta}F_{\eta}$ compared to the $LiMn_{1.8}Li_{0.1}Ni_{0.1}O_{4-\eta}F_{\eta}$ analog is due to a lower initial Mn valence and the consequent larger Δa (or lattice mismatch) and higher Mn dissolution. The correlations also illustrate that the larger capacity fade of $LiMn_{1.8}Li_{0.1}Ni_{0.1}O_{3.71}F_{0.29}$ compared to that of $LiMn_{1.8}Li_{0.1}Ni_{0.1}O_{3.8}F_{0.2}$ is due to a larger Δa and Mn dissolution.

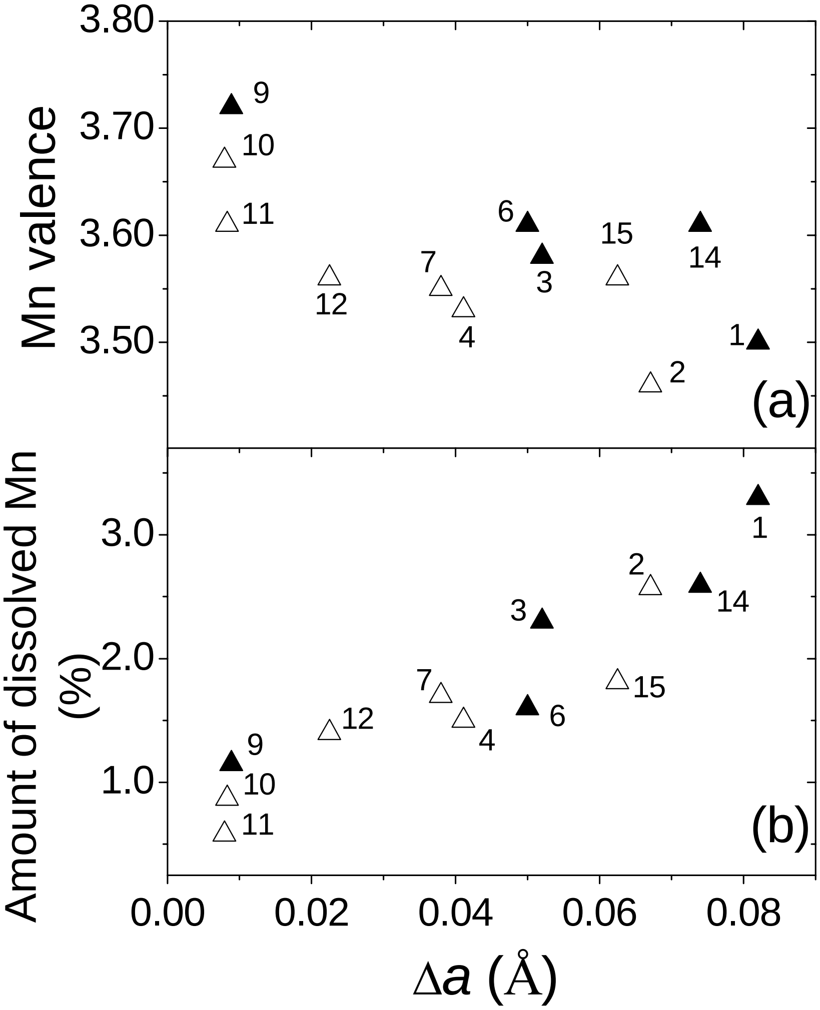

Figure 5.8 Correlation of the lattice parameter difference Δa between the two cubic phases formed during the charge-discharge process to the (a) initial Mn valence and (b) amount of manganese dissolution in the two-phase region. Closed and open triangles refer to, respectively, the oxide and oxyfluoride spinel cathodes. The numbers refer to the sample numbers in Table 5.1.

5.3.8 Loss of Crystallinity

Figure 5.9 compares the XRD patterns of $LiMn_2O_4$, $LiMn_{1.8}Li_{0.1}Ni_{0.1}O_4$, and $LiMn_{1.8}Li_{0.1}Ni_{0.1}O_{3.8}F_{0.2}$ cathodes after 50 cycles at 60 ^oC. While the $LiMn_2O_4$ electrode experiences a significant broadening of the diffraction peaks after 50 cycles, the $LiMn_{1.8}Li_{0.1}Ni_{0.1}O_{3.8}F_{0.2}$ electrode maintains sharp reflections even after cycling. The behavior of $LiMn_{1.8}Li_{0.1}Ni_{0.1}O_4$ is in between those of $LiMn_2O_4$ and $LiMn_{1.8}Li_{0.1}Ni_{0.1}O_{3.8}F_{0.2}$. The broadening of the diffraction peaks after cycling could be related to the large amount of Mn dissolution and the consequent loss of crystallinity in the case of $LiMn_2O_4$. Additionally, the large interfacial strain arising from a large Δa and lattice mismatch could also cause a broadening of the reflections. The crystallinity of the electrodes is an important factor, and the decrease in crystallinity could perturb or hinder the three-dimensional diffusion of lithium ions with a consequent impedance growth in the spinel lattice.[100,130]

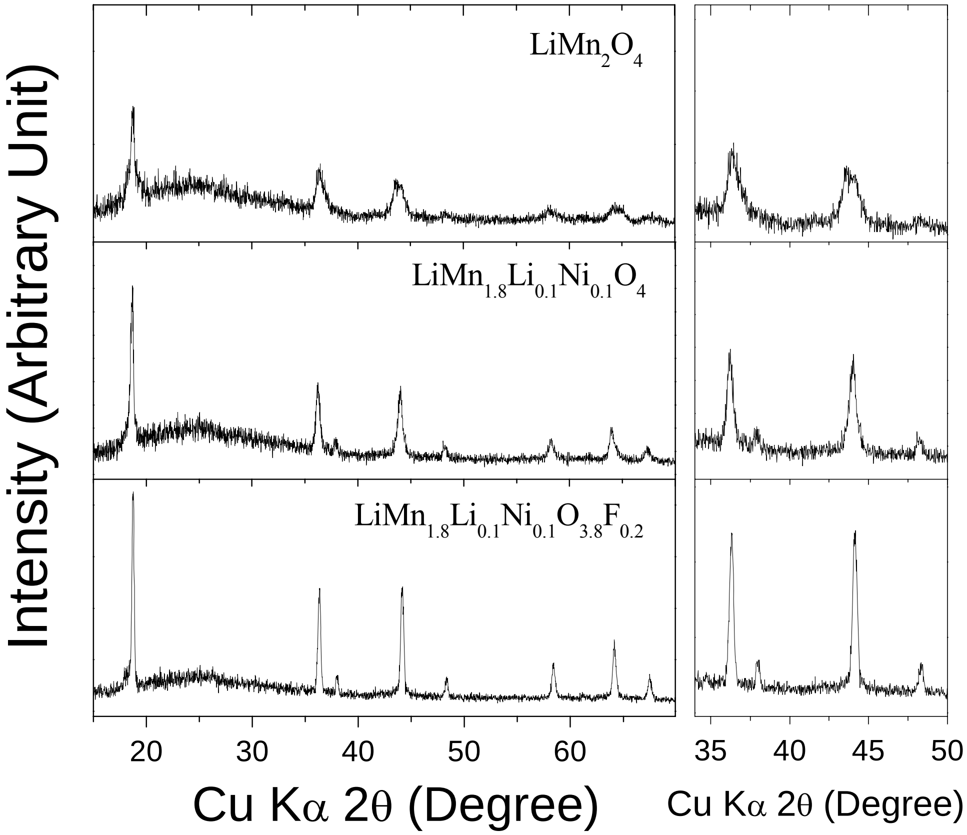

Figure 5.9 Comparison of the XRD patterns of the LiMn$_{2-y-z}$Li$_y$Ni$_z$O$_{4-\eta}$F$_\eta$ spinel cathodes after 50 cycles at 60 °C.

5.3.9 Area Specific Impedance

Area specific impedance (ASI) of the $LiMn_2O_4$, $LiMn_{1.8}Li_{0.1}Ni_{0.1}O_4$, and $LiMn_{1.8}Li_{0.1}Ni_{0.1}O_{3.8}F_{0.2}$ cathodes were evaluated before and after 50 cycles at 60 °C to assess the feasibility of utilizing the spinel oxyfluoride cathodes for EV or HEV applications. The ASI values were obtained at room temperature by adopting the PNGV L-HPPC test procedure.[160] After the first charge, the cell was subjected to an 18-s pulse discharge at 5C rate and 2-s pulse charge at 3.75C rate to obtain the ASI values at every 10 % DOD. This is termed as ASI values before cycling in Fig. 5.10. The cell was then cycled at 60 °C for 50 cycles, and the ASI values were determined at various DOD at room temperature following the procedure adopted before cycling. This is termed as ASI values after cycling in Fig. 5.10. While all the three samples were found to have a similar ASI values of 25-40 $\Omega\cdot cm^2$ at 50 % DOD before cycling, $LiMn_2O_4$ exhibits higher ASI values of around 120 $\Omega\cdot cm^2$ compared to 80-90 $\Omega\cdot cm^2$ for the $LiMn_{1.8}Li_{0.1}Ni_{0.1}O_4$ and $LiMn_{1.8}Li_{0.1}Ni_{0.1}O_{3.8}F_{0.2}$ cathodes after cycling at 60 °C. Although lithium ion cells employing the spinel cathode and carbon anode are known to experience the reduction of the dissolved manganese ions at the graphite/electrolyte interface and subsequent impedance rise,[162] the data in Figs. 5.9 and 5.10 suggest that the degradation of crystallinity as well as the manganese dissolution and lattice mismatch at the cathode itself could also result in impedance growth.

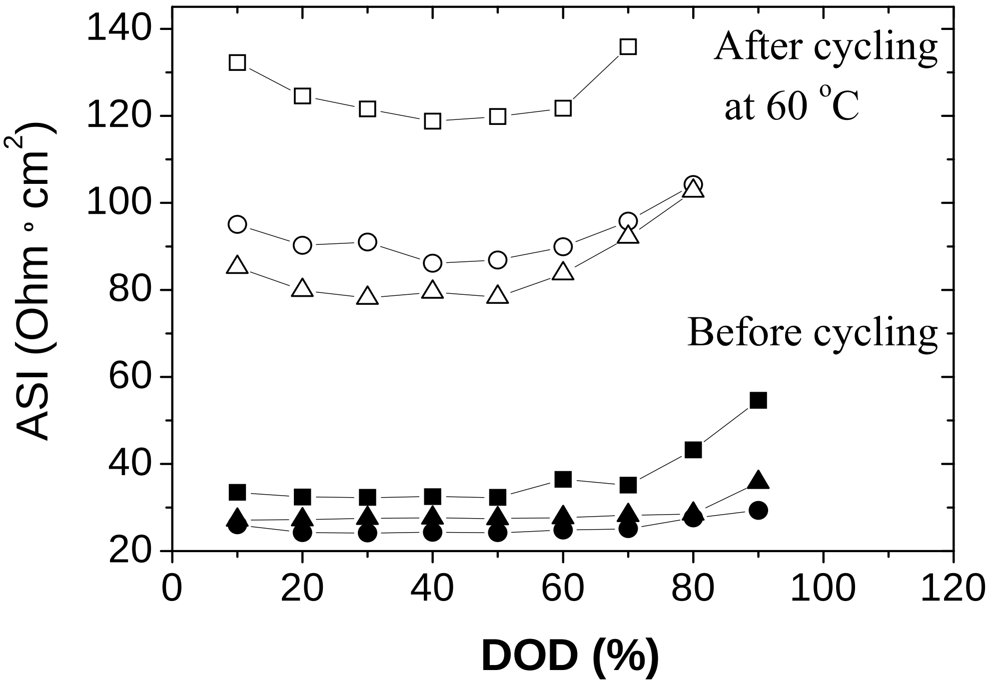

Figure 5.10 Area specific impedance (ASI) of the $LiMn_{2-y-z}Li_yNi_zO_{4-\eta}F_\eta$ spinel cathodes as a function of the depth of discharge (DOD) before and after 50 cycles at 60 ^{o}C. Closed and open symbols refer to, respectively, before and after cycling the cathodes at 60 ^{o}C: (■) $LiMn_2O_4$, (●) $LiMn_{1.8}Li_{0.1}Ni_{0.1}O_4$, and (▲) $LiMn_{1.8}Li_{0.1}Ni_{0.1}O_{3.8}F_{0.2}$.

5.3.10 Cycling Performance in Lithium Ion Battery

In addition to the electrochemical evaluation with metallic lithium anode, the performance of the spinel cathodes in lithium ion cells with carbon anode is critical to fully assess the benefits of cationic and anionic substitutions. Accordingly, lithium ion cells fabricated with the spinel $LiMn_{1.8}Li_{0.1}Ni_{0.1}O_{4-\eta}F_\eta$ cathodes and commercial carbon anodes were evaluated at 60 ^{o}C (Fig. 5.11). While the $LiMn_2O_4$/C lithium ion cell shows a severe capacity fade of 42 % with a continuous decline in capacity to 30 cycles at 60 °C, the $LiMn_{1.8}Li_{0.1}Ni_{0.1}O_4$/C and $LiMn_{1.8}Li_{0.1}Ni_{0.1}O_{3.8}F_{0.2}$/C cells exhibit better cyclability with a capacity fade of, respectively, 20 and 17 % after 30 cycles. After a small capacity fade during the first few cycles (< 10 cycles), the capacity value becomes stable with cycling for the cation-substituted oxyfluoride $LiMn_{1.8}Li_{0.1}Ni_{0.1}O_{3.8}F_{0.2}$. The results demonstrate the superior performance of the cation-substituted oxyfluoride cathodes in lithium ion cells with carbon anode compared to the conventional $LiMn_2O_4$ cathode.

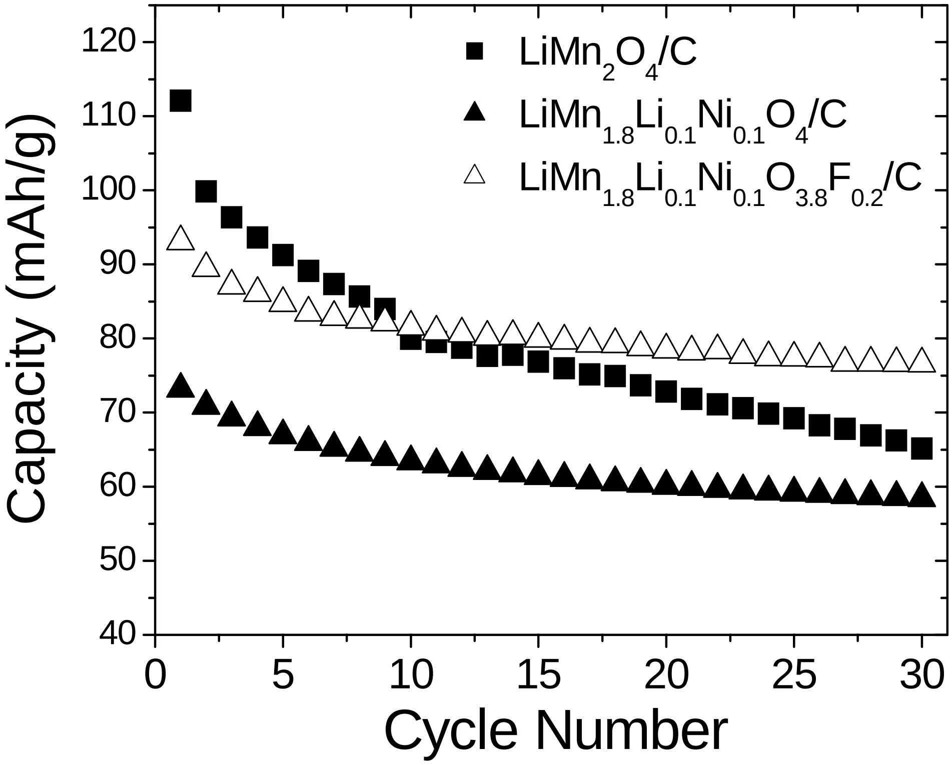

Figure 5.11 Cyclability of lithium ion cells fabricated with the spinel cathodes and carbon anode at 60 °C and C/5 rate.

5.4 CONCLUSIONS

Cation-substituted oxyfluoride spinel cathodes $LiMn_{2-y-z}Li_yNi_zO_{4-\eta}F_\eta$ have been found to exhibit much better capacity retention, rate capability, and storage characteristics along with low irreversible capacity loss in the first cycle compared to $LiMn_2O_4$. The amount of fluorine that could be incorporated into the spinel lattice depends on the Mn valence above 3.5+. The superior electrochemical performance of optimized spinel compositions such as $LiMn_{1.8}Li_{0.1}Ni_{0.1}O_{3.8}F_{0.2}$ with a capacity of over 100 mAh/g is found to be due to a significant suppression of the lattice mismatch between the two cubic phases formed during the charge-discharge process, much lower Mn dissolution, and maintenance of better crystallinity during cycling. However, a much higher fluorine content as in $LiMn_{1.8}Li_{0.1}Ni_{0.1}O_{3.71}F_{0.29}$ leads to a degradation in electrochemical performance due to a lower initial Mn valence and a consequent larger lattice mismatch and Mn dissolution. The results suggest that initial Mn valence is a key parameter in suppressing the lattice mismatch, Mn dissolution, and dynamic, short-range Jahn-Teller distortions and thereby to improve the electrochemical performance. The excellent electrochemical performance along with the low cost of the optimized oxyfluoride spinel cathodes may make them attractive for EV and HEV applications.

CHAPTER 6

ELECTROCHEMICAL PERFORMANCE OF SPINEL-LAYERED OXIDE COMPOSITE CATHODES

6.1 INTRODUCTION

In the previous chapters, it was shown that the Mn dissolution can be decreased drastically and the capacity retention could be improved significantly by increasing the initial Mn valence and reducing the lattice mismatch between the two cubic phases formed during the charge-discharge process via appropriate cationic and anionic substitutions, including the adoption of a low temperature fluorination of the spinel oxide precursors with NH_4HF_2. In this chapter, another strategy is presented to reduce the manganese dissolution and improve the electrochemical performance further by trapping the trace amounts of protons present in the electrolyte into a layered oxide cathode lattice during the first charge.

Through a systematic chemical and structural characterization of a number of chemically delithiated lithium ion battery cathodes, our group showed recently that certain layered oxide cathode compositions such as $Li_{1-x}CoO_2$ and $Li_{1-x}Mn_{1/3}Ni_{1/3}Co_{1/3}O_2$ incorporate protons into the lattice at deep chemical delithiation with an oxidizer NO_2BF_4 in acetonitrile medium.[163] On the other hand, layered oxides like $Li_{1-x}NiO_2$, orthorhombic $Li_{1-x}MnO_2$, spinel $Li_{1-x}Mn_2O_4$, and olivine $Li_{1-x}FePO_4$ do not incorporate protons under similar conditions of chemical delithiation with

NO_2BF_4. The incorporation of protons into layered $Li_{1-x}CoO_2$ and $Li_{1-x}Mn_{1/3}Ni_{1/3}Co_{1/3}O_2$ is to relieve the chemical instability arising from a significant overlap of the $Co^{3+/4+}$:3d band with the top of the O^{2-}:2p band, and it occurs via an ion exchange of Li^+ ions by the H^+ ions that may be generated in the chemical delithiation medium under the highly oxidizing conditions. Recognizing that layered $Li_{1-x}CoO_2$ at low lithium contents (< 0.5) could act as an effective scavenger for protons, the strategy in this chapter involves (i) addition of a moderate amount of layered $LiCoO_2$ to an optimized cation-substituted oxyfluoride spinel $LiMn_{1.8}Li_{0.1}Ni_{0.1}O_{3.8}F_{0.2}$, (ii) charging the spinel + layered oxide mixture to high enough voltages (4.7 V) in the first cycle to trap the trace amounts of protons present in the electrolyte within the layered oxide lattice and thereby suppress the disproportionation of Mn^{3+} and Mn dissolution, and (iii) cycling the mixture in the normal voltage range of 4.3 - 3.5 V in the subsequent discharge-charge cycles. The strategy helps not only to overcome the capacity fading problems of spinel cathodes by suppressing the Mn dissolution, but also to increase the capacity as the layered oxides offer higher capacities than the spinel cathodes. A comparison of the cyclabilities of the spinel and the spinel + layered composite cathodes with graphite anodes at 60 °C, Mn dissolution, storage characteristics, and rate capability are presented in this chapter.

6.2 EXPERIMENTAL

$LiMn_2O_4$ and the cation-substituted $LiMn_{1.8}Li_{0.1}Ni_{0.1}O_4$ spinel oxides were synthesized by firing required amounts of Li_2CO_3, Mn_2O_3, and NiO at 800 °C for 48 h in air. Fluorine substituted $LiMn_{1.8}Li_{0.1}Ni_{0.1}O_{3.8}F_{0.2}$ was prepared by firing the $LiMn_{1.8}Li_{0.1}Ni_{0.1}O_4$ spinel oxide with a required amount of NH_4HF_2 at 450 ^{o}C for 5 h in air as described in chapter 5. $LiCoO_2$ was synthesized by firing the required amount of Li_2CO_3 and Co_3O_4 at 900 ^{o}C for 24 h in air. $LiNi_{0.85}Co_{0.15}O_2$ was prepared by firing coprecipitated hydroxides of Ni and Co with lithium hydroxide in O_2 atmosphere at 750 ^{o}C for 24 h. The lithium contents were analyzed by atomic absorption spectroscopy (AAS) and the average oxidation state of manganese was determined by a redox titration involving sodium oxalate and potassium permanganate as described in chapter 2.

The cathodes were prepared by mixing the spinel and/or layered oxide powders with 20 wt. % conductive carbon and 5 wt. % PTFE binder, rolling the mixture into thin sheets, and cutting into circular electrodes of 0.64 cm^2 area. Electrochemical performances were evaluated with CR2032 coin cells fabricated with the cathodes, 1 M $LiPF_6$ in 1:1 EC and DEC electrolyte, Celgard polypropylene separator, and graphite or metallic lithium anode. While the cyclability data were collected with lithium ion cells fabricated with graphite anode, the Mn dissolution, rate capability, and storage property data were collected with cells fabricated with lithium anode.

The degree of manganese dissolution was evaluated by storing the coin cells fabricated with metallic lithium anode for 7 days at 60 ^{o}C and washing the coin cell components with deionized water and propylene carbonate at room temperature, followed by analyzing the manganese content by AAS.

6.3 RESULTS AND DISCUSSION

6.3.1 Cycling Performance

Figure 6.1 compares the cycling performances of lithium ion coin cells fabricated with spinel $LiMn_2O_4$, a mixture of spinel $LiMn_2O_4$ and layered $LiCoO_2$ (70:30), spinel $LiMn_{1.8}Li_{0.1}Ni_{0.1}O_{3.8}F_{0.2}$, and a mixture of spinel $LiMn_{1.8}Li_{0.1}Ni_{0.1}O_{3.8}F_{0.2}$ and layered $LiCoO_2$ (70:30) cathodes and graphite anode at 60 ^{o}C at C/5 rate while Table 6.1 gives the initial capacity values and the % capacity loss after 30 cycles at 60 ^{o}C. While the $LiMn_2O_4$ cathode both in the absence and presence of layered $LiCoO_2$ shows severe capacity fade after 30 cycles in Fig. 6.1a, the $LiMn_{1.8}Li_{0.1}Ni_{0.1}O_{3.8}F_{0.2}$ spinel cathode exhibits better cycling performance in Fig. 6.1b due to a suppression of the lattice mismatch between the two cubic phases formed during charge-discharge and Mn dissolution as discussed in chapter 5. With both $LiMn_2O_4$ and $LiMn_{1.8}Li_{0.1}Ni_{0.1}O_{3.8}F_{0.2}$, the addition of layered $LiCoO_2$ results in slightly higher capacity values as layered $LiCoO_2$ is known to offer higher capacity than the spinel cathodes. Interestingly, while the $LiMn_2O_4$ spinel alone cathode in Fig. 6.1a shows similar capacity retention irrespective of the first charge voltage (4.3 or 4.7 V), the spinel $LiMn_2O_4$ + layered $LiCoO_2$ mixture exhibits much better capacity retention on charging up to 4.7 V and holding for 2 h in the first cycle compared to charging up to 4.3 V in the first cycle. A similar observation can also be found on comparing the $LiMn_{1.8}Li_{0.1}Ni_{0.1}O_{3.8}F_{0.2}$ spinel alone cathode and the spinel

$LiMn_{1.8}Li_{0.1}Ni_{0.1}O_{3.8}F_{0.2}$ + layered $LiCoO_2$ mixture in Fig. 6.1b; charging the spinel $LiMn_{1.8}Li_{0.1}Ni_{0.1}O_{3.8}F_{0.2}$ + layered $LiCoO_2$ mixture to 4.7 V in the first cycle offers better capacity retention than charging up to 4.3 V although the difference between charging up to 4.7 and 4.3 V is small compared to that found with the spinel $LiMn_2O_4$ + layered $LiCoO_2$ mixture in Fig. 6.1a as the $LiMn_{1.8}Li_{0.1}Ni_{0.1}O_{3.8}F_{0.2}$ spinel alone already exhibits better capacity retention due to low Mn dissolution.

For a comparison, Fig. 6.2 displays similar data collected under identical conditions by employing layered $LiNi_{0.85}Co_{0.15}O_2$ instead of layered $LiCoO_2$. In contrast to the observations in Fig. 6.1, the addition of layered $LiNi_{0.85}Co_{0.15}O_2$ and charging up to 4.7 V in the first cycle does not lead to any improvement in capacity retention. This is because $LiNi_{0.85}Co_{0.15}O_2$ is known not to incorporate any proton into the lattice at deep lithium extraction unlike $LiCoO_2$ as revealed by chemical delithiation experiments.[163] Comparison of the data in Figs. 6.1 and 6.2 reveals that initial charging (first cycle) up to 4.7 V with layered oxides such as $LiCoO_2$ that trap protons can be utilized effectively to improve the capacity retention of spinel cathodes.

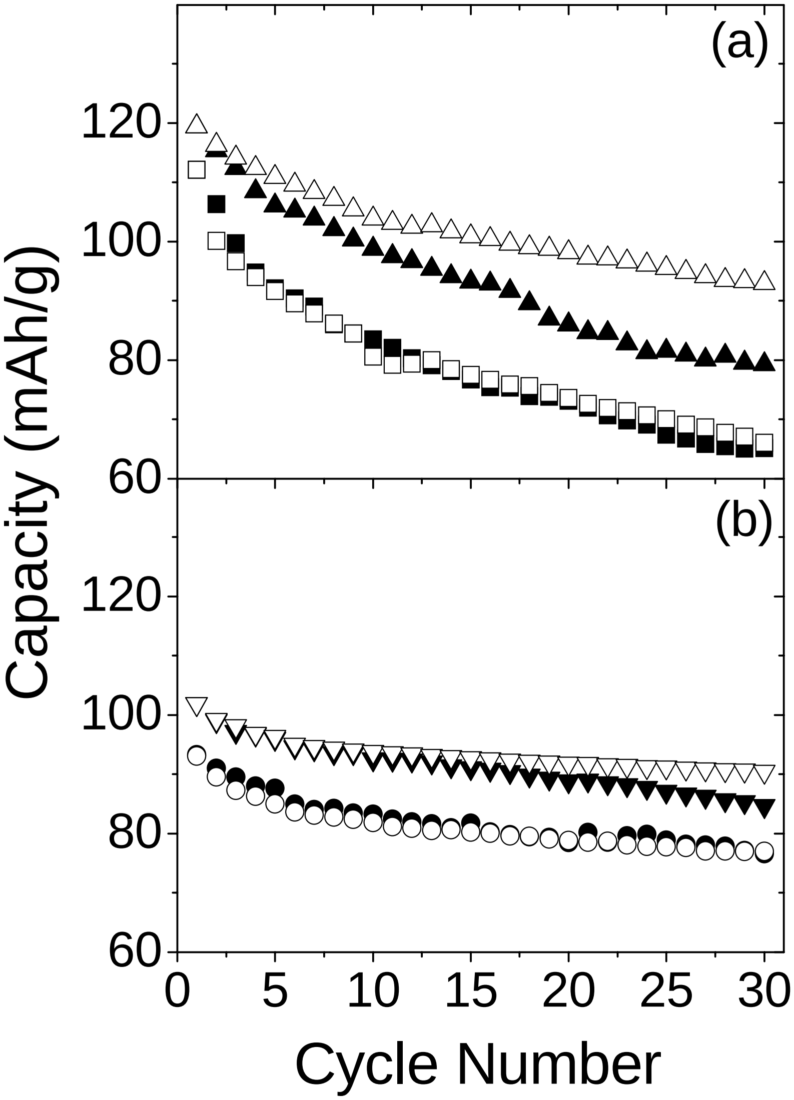

Figure 6.1 Cycling performance of lithium ion cells fabricated with graphite anode: (a) (■) $LiMn_2O_4$ between 3.5 and 4.3 V, (□) $LiMn_2O_4$ between 3.5 and 4.3 V after charging up to 4.7 V during first charge, (▲) 70 wt% $LiMn_2O_4$ + 30 wt% $LiCoO_2$ between 3.5 and 4.3 V, and (△) 70 wt% $LiMn_2O_4$ + 30 wt% $LiCoO_2$ between 3.5 and 4.3 V after charging up to 4.7 V during first charge, (b) (●) $LiMn_{1.8}Li_{0.1}Ni_{0.1}O_{3.8}F_{0.2}$ between 3.5 and 4.3 V, (○) $LiMn_{1.8}Li_{0.1}Ni_{0.1}O_{3.8}F_{0.2}$ between 3.5 and 4.3 V after charging up to 4.7 V during first charge, (▼) 70 wt% $LiMn_{1.8}Li_{0.1}Ni_{0.1}O_{3.8}F_{0.2}$ + 30 wt% $LiCoO_2$ between 3.5 and 4.3 V, and (▽) 70 wt% $LiMn_{1.8}Li_{0.1}Ni_{0.1}O_{3.8}F_{0.2}$ + 30 wt% $LiCoO_2$ between 3.5 and 4.3 V after charging up to 4.7 V during first charge. The discharge capacity values in the first cycle are not included in the plot as they can vary depending upon whether the cell is charged to 4.3 or 4.7 V during first charge.

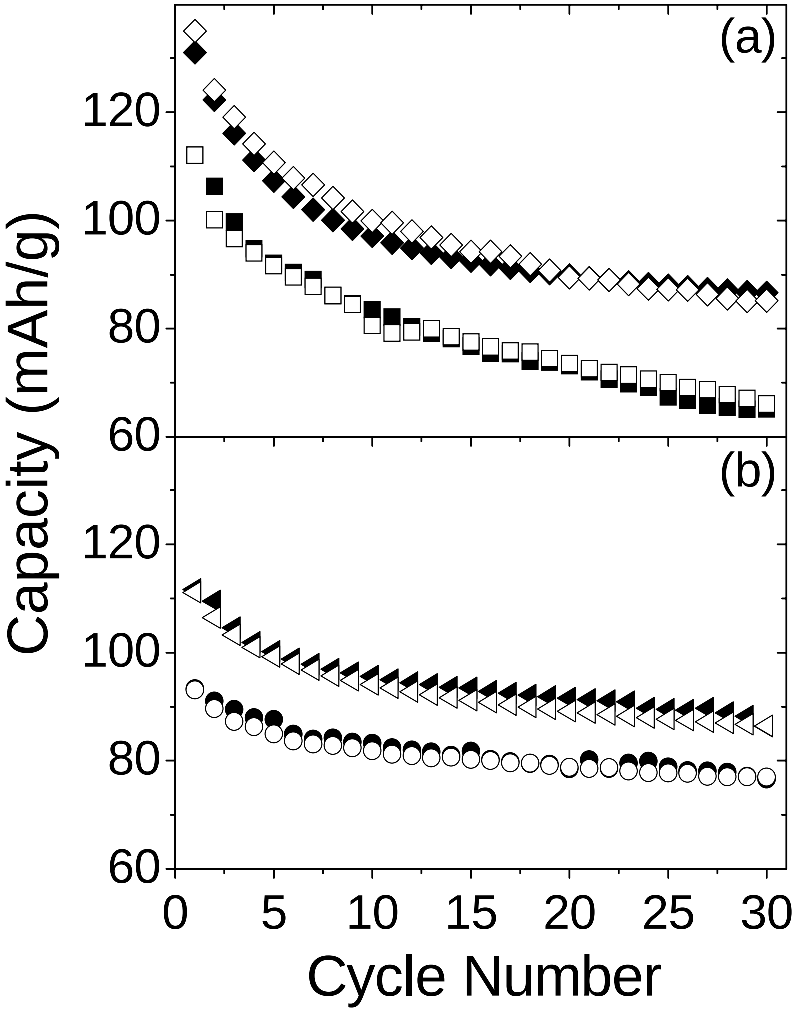

Figure 6.2 Cycling performance of lithium ion cells: (a) (■) $LiMn_2O_4$ between 3.5 and 4.3 V, (□) $LiMn_2O_4$ between 3.5 and 4.3 V after charging up to 4.7 V during first charge, (◆) 70 wt% $LiMn_2O_4$ + 30 wt% $LiNi_{0.85}Co_{0.15}O_2$ between 3.5 and 4.3 V, and (◇) 70 wt% $LiMn_2O_4$ + 30 wt% $LiNi_{0.85}Co_{0.15}O_2$ between 3.5 and 4.3 V after charging up to 4.7 V during first charge, (b) (●) $LiMn_{1.8}Li_{0.1}Ni_{0.1}O_{3.8}F_{0.2}$ between 3.5 and 4.3 V, (○) $LiMn_{1.8}Li_{0.1}Ni_{0.1}O_{3.8}F_{0.2}$ between 3.5 and 4.3 V after charging up to 4.7 V during first charge, (◀) 70 wt% $LiMn_{1.8}Li_{0.1}Ni_{0.1}O_{3.8}F_{0.2}$ + 30 wt% $LiNi_{0.85}Co_{0.15}O_2$ between 3.5 and 4.3 V, and (◁) 70 wt% $LiMn_{1.8}Li_{0.1}Ni_{0.1}O_{3.8}F_{0.2}$ + 30 wt% $LiNi_{0.85}Co_{0.15}O_2$ between 3.5 and 4.3 V after charging up to 4.7 V during first charge. The discharge capacity values in the first cycle are not included in the plot as they can vary depending upon whether the cell is charged to 4.3 or 4.7 V during first charge.

Table 6.1 Capacity fade and manganese dissolution data collected with spinel alone and spinel + layered oxide composite cathodes.

Cathode composition	Initial capacity[a] (mAh/g)	Capacity loss[b] (%)	Capacity loss[c] (%)	Mn dissolution[d] (%)	Mn dissolution[e] (%)	Mn dissolution[f] (%)
$LiMn_2O_4$	112.1	41.9	41.1	0.93	0.83	0.88
$LiMn_{1.8}Li_{0.1}Ni_{0.1}O_{3.8}F_{0.2}$	93.1	17.7	17.3	0.30	0.27	0.27
$LiCoO_2$	132.2	12.1	11.3	-	-	-
$LiNi_{0.85}Co_{0.15}O_2$	162.2	21.1	21.4	-	-	-
$LiMn_2O_4$ + $LiCoO_2$ (70:30)	119.4	33.6	22.3	0.88	0.59	0.41
$LiMn_2O_4$ + $LiNi_{0.85}Co_{0.15}O_2$ (70:30)	133.4	35.0	36.1	0.93	0.89	0.89
$LiMn_{1.8}Li_{0.1}Ni_{0.1}O_{3.8}F_{0.2}$ + $LiCoO_2$ (70:30)	101.9	16.9	11.2	0.28	0.11	0.08
$LiMn_{1.8}Li_{0.1}Ni_{0.1}O_{3.8}F_{0.2}$ + $LiNi_{0.85}Co_{0.15}O_2$ (70:30)	111.7	22.1	22.7	0.31	0.31	0.29

[a] Refers to the discharge capacity in the second cycle between 4.3 and 3.5 V since the first discharge capacity can be different depending on whether the cell is charged to 4.3 or 4.7 V during first charge.

[b] % capacity loss after 30 cycles in lithium ion cells fabricated with graphite anode and cycled between 3.5 and 4.3 V at 60 °C.

[c] % capacity loss after 30 cycles in lithium ion cells fabricated with graphite anode, charged up to 4.7 V in the first cycle, held for 2 h, and then cycled between 4.3 and 3.5 V at 60 °C.

[d] % dissolution based on Mn weight after storing at 60 °C for 7 days without any charge-discharge the coin cells fabricated with lithium anode.

[e] % dissolution based on Mn weight after storing at 60 °C for 7 days at the end of first charge to 4.7 V the coin cells fabricated with lithium anode.

[f] % dissolution based on Mn weight after storing at 60 °C for 7 days at the end of first charge to 4.7 V followed by first discharge to 3.5 V the coin cells fabricated with lithium anode.

6.3.2 Manganese Dissolution

The degree of manganese dissolution after storing at different stages for 7 days at 60 ^{o}C the coin cells fabricated with metallic lithium anode was evaluated and the data are given in Table 6.1 to understand the role of initial charging to 4.7 V on the electrochemical performance. $LiMn_2O_4$ spinel alone cathode exhibits a higher Mn dissolution of ~ 0.9 % compared to ~ 0.3 % for the $LiMn_{1.8}Li_{0.1}Ni_{0.1}O_{3.8}F_{0.2}$ spinel alone cathode. The Mn dissolution values remain nearly the same irrespective of whether or not the cell is charged to 4.7 V with these spinel alone cathodes. Similar observations can also be found with both the spinel $LiMn_2O_4$ + layered $LiNi_{0.85}Co_{0.15}O_2$ and spinel $LiMn_{1.8}Li_{0.1}Ni_{0.1}O_{3.8}F_{0.2}$ + layered $LiNi_{0.85}Co_{0.15}O_2$ composite cathodes. In other words, the addition of layered $LiNi_{0.85}Co_{0.15}O_2$ to the spinel does not change the Mn dissolution values irrespective of whether or not the cell is charged to 4.7 V. In contrast, the spinel $LiMn_2O_4$ + layered $LiCoO_2$ cathode shows a drastic decrease in Mn dissolution in both the charged (0.59 %) and discharged (0.41 %) states after charging to 4.7 V compared to the value (0.88 %) found without subjecting to a 4.7 V charge. Similarly, spinel $LiMn_{1.8}Li_{0.1}Ni_{0.1}O_{3.8}F_{0.2}$ + layered $LiCoO_2$ composite cathode shows a decrease in Mn dissolution in both the charged (0.11 %) and discharged (0.08 %) states after charging to 4.7 V compared to the value (0.28 %) found without subjecting to the 4.7 V charge. The data in Table 6.1 demonstrate that layered oxides such as $Li_{1-x}CoO_2$ that trap protons within the layered lattice at low lithium contents (or in the over-charged state) as indicated by previous chemical delithiation experiments[163] can effectively suppress the disproportionation reaction of Mn^{3+} and thereby the amount of Mn dissolution.

6.3.3 Storage Properties

Figure 6.3 compares the storage characteristics of coin cells fabricated with metallic lithium anode and spinel alone or spinel + layered oxide cathodes. The storage performances were evaluated by charging the coin cells to 4.3 V or 4.7 V and holding for 2 h before discharging to 3.5 V at room temperature in the first cycle, followed by a charge-discharge cycle between 3.5 and 4.3 V at room temperature in the second cycle, discharging to various DOD in the third cycle, storing at 60 °C for 7 days at various DOD, completing the third discharge cycle after cooling to room temperature, and evaluating the full discharge capacity in the fourth cycle at room temperature. The % capacity retention in Fig. 6.3 was obtained as a ratio of the fourth discharge capacity to the second discharge capacity. Both the $LiMn_{1.8}Li_{0.1}Ni_{0.1}O_{3.8}F_{0.2}$ spinel alone cathode as well as the spinel $LiMn_{1.8}Li_{0.1}Ni_{0.1}O_{3.8}F_{0.2}$ + layered $LiCoO_2$ mixture cathode retain > 97 % of their initial capacities, indicating excellent storage characteristics. Although the spinel $LiMn_2O_4$ cathode loses a significant amount of capacity after storage (60 % retention at 60 % DOD) regardless of the initial charging up to 4.7 V, the spinel $LiMn_2O_4$ + layered $LiCoO_2$ cathode shows an improvement with a retention of 70 % (at 60 % DOD) without first charge to 4.7 V and a retention of 77 % (at 60 % DOD) with a first charge to 4.7 V due to a trapping of protons within the layered oxide lattice and a consequent reduction in Mn dissolution.

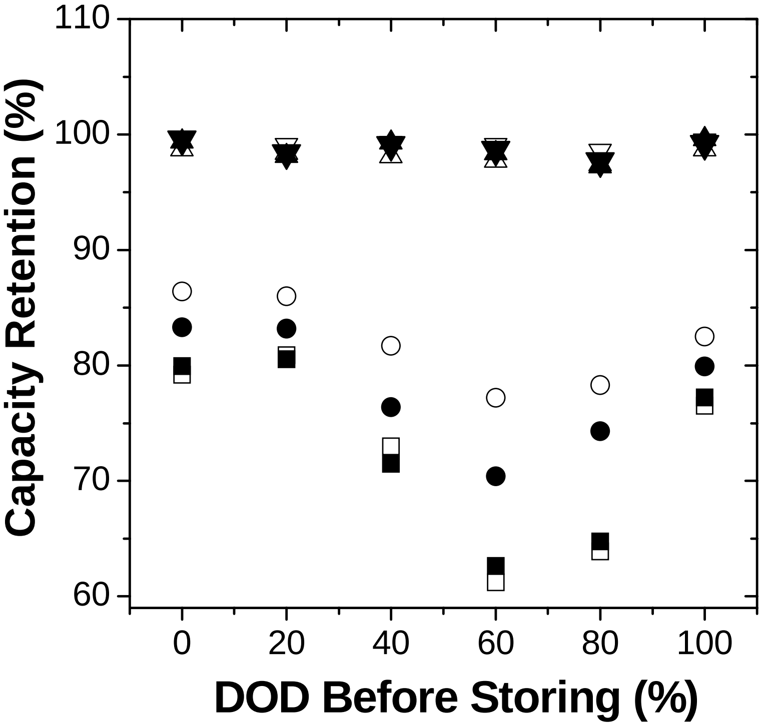

Figure 6.3 Comparison of the percentage capacity retention after storing at 60 °C for 7 days at different depth of discharge (DOD) the coin cells fabricated with metallic lithium anode: (■) $LiMn_2O_4$ between 3.5 and 4.3 V, (□) $LiMn_2O_4$ between 3.5 and 4.3 V after charging up to 4.7 V during first charge, (●) 70 wt% $LiMn_2O_4$ + 30 wt% $LiCoO_2$ between 3.5 and 4.3 V, (○) 70 wt% $LiMn_2O_4$ + 30 wt% $LiCoO_2$ between 3.5 and 4.3 V after charging up to 4.7 V during first charge, (▲) $LiMn_{1.8}Li_{0.1}Ni_{0.1}O_{3.8}F_{0.2}$ between 3.5 and 4.3 V, (△) $LiMn_{1.8}Li_{0.1}Ni_{0.1}O_{3.8}F_{0.2}$ between 3.5 and 4.3 V after charging up to 4.7 V during first charge, (▼) 70 wt% $LiMn_{1.8}Li_{0.1}Ni_{0.1}O_{3.8}F_{0.2}$ + 30 wt% $LiCoO_2$ between 3.5 and 4.3 V, and (▽) 70 wt% $LiMn_{1.8}Li_{0.1}Ni_{0.1}O_{3.8}F_{0.2}$ + 30 wt% $LiCoO_2$ between 3.5 and 4.3 V after charging up to 4.7 V during first charge.

6.3.4 Rate Capability

Figure 6.4 compares the discharge profiles of the spinel alone and the spinel + layered oxide composite cathodes to illustrate the rate capability and assess the feasibility for high power applications such as HEV and EV. All the cells were made with metallic lithium anode, charged up to 4.7 V at C/20 rate in the first cycle, held for 2 h, discharged to 3.5 V at C/10 rate in the first cycle, charged at the same rate of C/10 in the second cycle, and then subjected to different discharge rates of C/10 to 4C as shown in Fig. 6.4 to assess the rate capability. The spinel $LiMn_{1.8}Li_{0.1}Ni_{0.1}O_{3.8}F_{0.2}$ cathode exhibits superior rate capability with a retention of 96 % of its capacity ongoing from C/10 to 4C rate compared to 46 % retention for $LiMn_2O_4$ due to a much smaller lattice mismatch between the two cubic phases formed during the charge-discharge process as well as due to a higher initial Mn valence and the consequent suppression of short range, dynamic Jahn-Teller distortions as discussed in previous chapters. Although the addition of layered $LiCoO_2$ to $LiMn_2O_4$ spinel helps to increase the rate capability slightly as $LiMn_2O_4$ alone has a poor rate capability, the addition of layered $LiCoO_2$ to $LiMn_{1.8}Li_{0.1}Ni_{0.1}O_{3.8}F_{0.2}$ spinel decreases the rate capability slightly as the $LiMn_{1.8}Li_{0.1}Ni_{0.1}O_{3.8}F_{0.2}$ spinel alone has much better rate capability than layered $LiCoO_2$ alone. Despite the slight decrease in rate capability, the addition of layered $LiCoO_2$ to $LiMn_{1.8}Li_{0.1}Ni_{0.1}O_{3.8}F_{0.2}$ spinel provides the important advantage of suppressing the Mn dissolution and improving the cyclability at elevated temperatures while also increasing the capacity values.

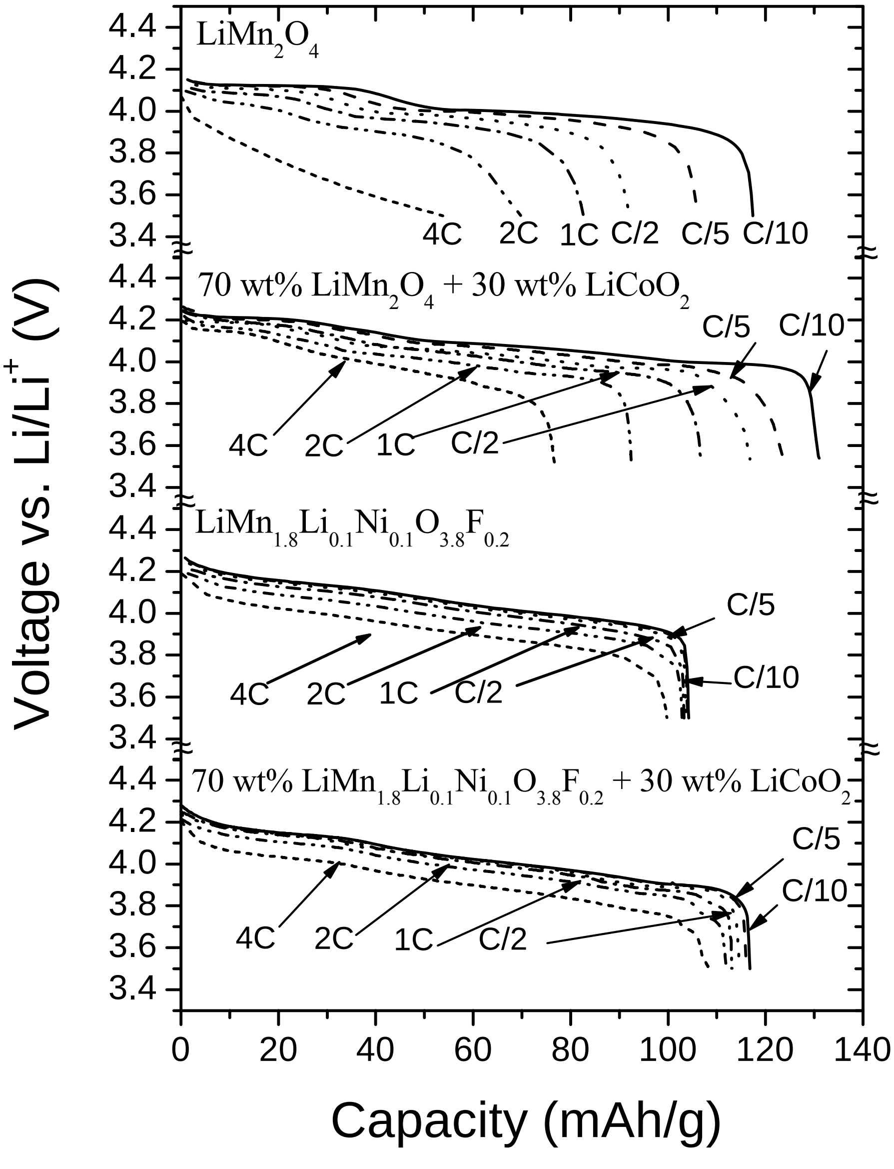

Figure 6.4 Comparison of the discharge profiles at various C rates of coin cells fabricated with metallic lithium anode, illustrating the rate capabilities of $LiMn_2O_4$, 70 wt% $LiMn_2O_4$ + 30 wt% $LiCoO_2$, $LiMn_{1.8}Li_{0.1}Ni_{0.1}O_{3.8}F_{0.2}$, and 70 wt% $LiMn_{1.8}Li_{0.1}Ni_{0.1}O_{3.8}F_{0.2}$ + 30 wt% $LiCoO_2$. See the text for the procedure adopted.

6.4 CONCLUSIONS

In this chapter, a strategy to suppress Mn dissolution and improve the capacity retention of spinel oxide cathodes at elevated temperatures was demonstrated. It involves the trapping within a layered oxide cathode lattice the trace amounts of protons that could be present in the electrolyte by charging a composite cathode consisting of spinel and layered oxide to 4.7 V during first charge. Although the addition of layered oxide decreases the rate capability slightly, optimizing the distribution and amounts of and the interface between the spinel and layered oxide particles can minimize the influence on rate capability.

CHAPTER 7

FLUORINE SUBSTITUTION USING LiF AND ELECTROCHEMICAL PERFORMANCE OF 3 V SPINEL $Li_4Mn_5O_{12-\eta}F_\eta$ CATHODES

7.1 INTRODUCTION

Lithium manganese oxides crystallizing in the spinel structure have been widely studied as cathode materials for lithium batteries as Mn is inexpensive and environmentally benign. For example, spinel $LiMn_2O_4$ involving the extraction/insertion of lithium from/into the 8a tetrahedral sites in the 4 V region has been investigated extensively in the literature.[102-105,120-129] In addition to the above process, $LiMn_2O_4$ is known to reversibly insert an extra lithium into the 16c octahedral sites in the 3 V region, but this process involves a drastic capacity fade due to the occurrence of Jahn-Teller distortion[55-57] arising from a decrease in the oxidation state of manganese below 3.5+ during cycling. However, the Jahn-Teller distortion could be suppressed by a substitution of lower valent Li^+ for Mn^{3+} in $Li_{1+x}Mn_{2-x}O_4$ and the consequent increase in the average oxidation state of Mn. In this regard, spinel $Li_4Mn_5O_{12}$ (or $Li[Mn_{1.67}Li_{0.33}]O_4$), which is the end member of the $Li_{1+x}Mn_{2-x}O_4$ solid solution with x = 0.33 and an oxidation state of 4+ for Mn, has become an attractive candidate for 3 V cells. It has been found that the cubic symmetry can be preserved in the 3 V region without Jahn-Teller distortion over a wide compositional range of up to x = 2.5 in $Li_{1+x}Mn_5O_{12}$.[62,63]

However, the synthesis of spinel $Li_4Mn_5O_{12}$ containing all Mn^{4+} is tedious as it tends to disproportionate into $LiMn_2O_4$ and Li_2MnO_3 during synthesis at T > 500 °C or the solid state reaction could become incomplete at T < 500 °C.[62,164-167] In this regard, solution-based oxidation reactions followed by firing at or below 500 °C have been found to give single phase $Li_4Mn_5O_{12}$.[61] Another strategy to suppress the disproportionation reaction is to lower the oxidation state of Mn in $Li_4Mn_5O_{12}$ through an anionic substitution of F^- for O^{2-}. Substitution of F^- for O^{2-} ions in the layered as well as 4 V spinel oxide cathodes have been found to improve the electrochemical performances.[137,138,157,158] In this chapter, the synthesis of spinel oxyfluorides $Li_4Mn_5O_{12-\eta}F_\eta$ ($0 \leq \eta \leq 0.2$) by utilizing LiF as a fluorine source and a comparison of the electrochemical properties with those of the analogous spinel oxide cathode $Li_4Mn_5O_{12}$ are presented.

7.2 EXPERIMENTAL

Spinel $Li_4Mn_5O_{12-\eta}F_\eta$ ($0 \leq \eta \leq 0.2$) oxyfluorides were synthesized by firing manganese hydroxide with LiOH and LiF for 3 days in air at 500 or 600 °C; manganese hydroxide was obtained by adding a required amount of Mn^{2+}solution into LiOH solution, followed by filtering and washing. All the samples were characterized by X-ray diffraction (XRD). The lithium contents were determined by atomic absorption spectroscopy (AAS) and the oxidation state of manganese was determined by a redox titration involving sodium oxalate and potassium permanganate.

Electrochemical performances of the cathodes were evaluated with CR2032 coin cells fabricated with metallic lithium anode, Celgard polypropylene separator, and 1 M $LiClO_4$ in 1:1 propylene carbonate (PC) and dimethoxyethane (DME) or 1 M $LiPF_6$ in 1:1 ethylene carbonate (EC) and diethyl carbonate (DEC) electrolyte. The cathodes were prepared by mixing 75 wt. % $Li_4Mn_5O_{12-\eta}F_\eta$ powder with 20 wt. % acetylene black and 5 wt. % polytetrafluoroethylene (PTFE) binder, rolling the mixture into thin sheets, and punching circular electrodes of 0.64 cm^2 area. Cycle tests were carried out between 3.3 and 2.4 V at both room temperature and 60 ^oC at C/5 rate. The degree of manganese dissolution was evaluated by storing the coin cells in the fully discharged state (after the first discharge) at 60 ^oC for 7 days, followed by washing the coin cell components with deionized water at room temperature and analyzing the manganese content by AAS.

7.3 RESULTS AND DISCUSSION

7.3.1 Crystal Chemistry

The average oxidation state values of manganese determined by the redox titration are given in Table 7.1. The manganese oxidation state was found to be 3.98+ and 3.97+, respectively, in the oxide samples synthesized at 500 and 600 ^oC due to the difficulty of achieving all Mn^{4+} as had been found in the literature before.[14,17] The $Li_4Mn_5O_{12-\eta}F_\eta$ oxyfluoride samples show lower oxidation state values compared to the corresponding oxide analogs, confirming the bulk substitution of F^- for O^{2-} and the consequent reduction of Mn^{4+} to Mn^{3+} in the lattice. The oxygen content values in the formula given in Table 1 were obtained based on the experimentally determined lithium contents and oxidation state values by employing the charge neutrality principle. Although high temperature syntheses around 850 °C with LiF are known to encounter volatilization of fluorine,[137,138,140] the synthesis at moderate temperatures here suppresses such volatilization problems.

Figure 7.1 compares the XRD patterns of the $Li_4Mn_5O_{12-\eta}F_\eta$ samples synthesized at 500 and 600 °C, and an enlargement of the patterns over a small 2θ range are given in Fig. 7.2. In the case of the oxide samples, the spinel reflections move to slightly lower 2θ values with the appearance of weak reflections corresponding to Li_2MnO_3 as the synthesis temperature increases from 500 °C to 600 °C, confirming the disproportionation of $Li_4Mn_5O_{12}$ to a lithium-rich spinel containing Mn^{3+} ($Li_{1+x}Mn_{2-x}O_4$ with $x < 0.33$) and Li_2MnO_3 (all Mn^{4+}). Interestingly, the substitution of fluorine suppresses the formation of the impurity phase Li_2MnO_3 and causes a slight shift of the spinel reflections to lower 2θ values compared to that in the oxide analogs for the samples synthesized at 600 °C, confirming the suppression of the disproportionation reaction to give Li_2MnO_3 due to a decreased oxidation state of manganese in the lattice. For example, the $Li_4Mn_5O_{11.73}F_{0.2}$ sample synthesized at 600 ^{o}C does not show any reflections corresponding to Li_2MnO_3, suggesting that fluorine incorporation may be an effective way to obtain phase pure samples.

Table 7.1 Chemical and electrochemical characterization data of spinel $Li_4Mn_5O_{12-\eta}F_\eta$ cathodes.

Composition	Synthesis temperature (°C)	Lithium content	Mn valence[a]	$LiClO_4$			$LiPF_6$			Dissolved Mn[b] in $LiClO_4$ (%)	Dissolved Mn[b] in $LiPF_6$ (%)
				Initial capacity (mAh/g)	25 °C capacity loss[a] (%)	60 °C capacity loss[a] (%)	Initial capacity (mAh/g)	25 °C capacity loss[a] (%)	60 °C capacity loss[a] (%)		
$Li_4Mn_5O_{11.95}$	500	4.00	3.98	151	5.1	7.7	148	5.5	15.7	0.11	0.97
$Li_4Mn_5O_{11.85}F_{0.1}$	500	4.00	3.96	158	2.9	3.9	160	2.8	6.9	0.11	0.62
$Li_4Mn_5O_{11.92}$	600	3.99	3.97	139	4.7	6.5	135	6.4	18.3	0.13	0.87
$Li_4Mn_5O_{11.85}F_{0.1}$	600	3.99	3.96	150	3.8	5.7	148	4.9	12.1	0.11	0.68
$Li_4Mn_5O_{11.73}F_{0.2}$	600	4.00	3.93	152	8.4	9.6	150	8.8	21.1	0.11	0.84

[a] % capacity loss after 50 cycles.

[b] % dissolution after storing the coin cells for 7 days at 60 °C in the fully discharged state after the first discharge.

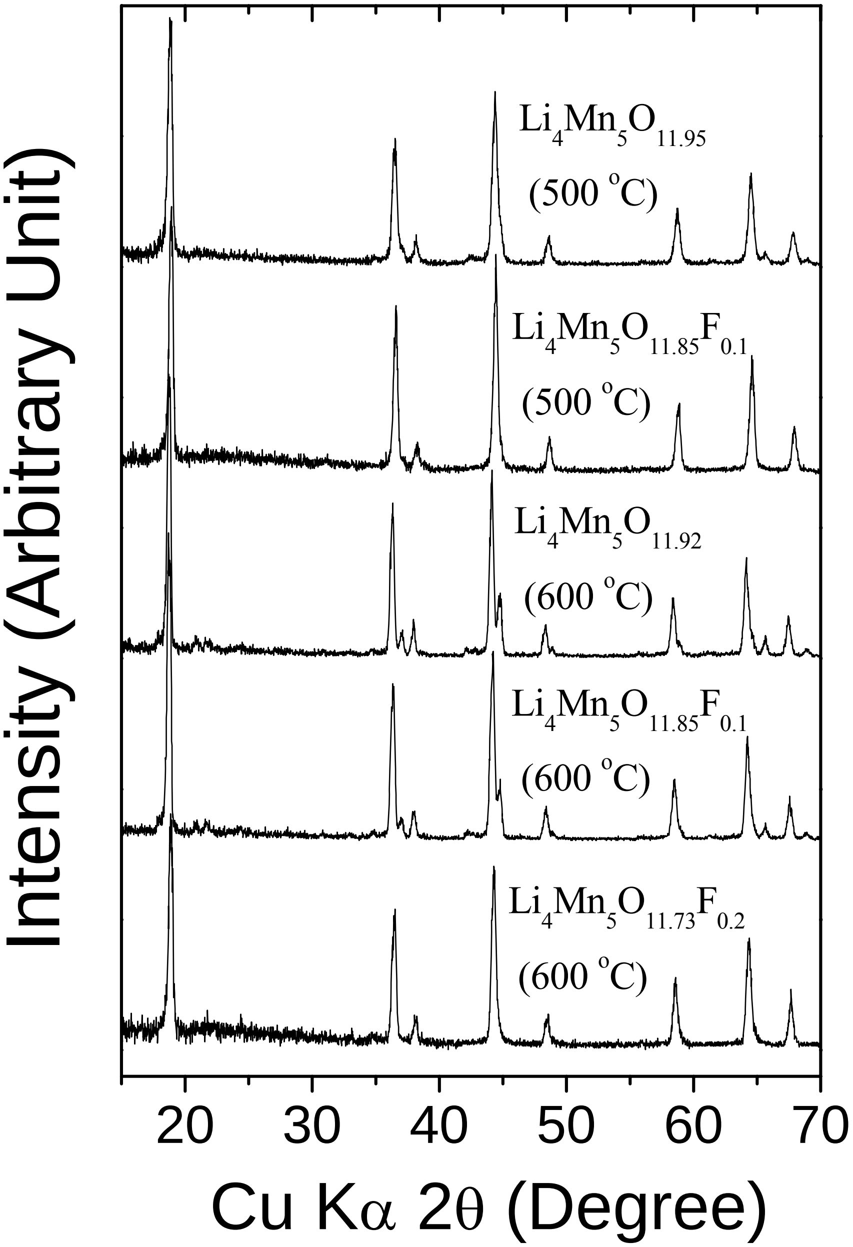

Figure 7.1 XRD patterns of the spinel $Li_4Mn_5O_{12-\eta}F_\eta$ samples synthesized at 500 and 600 ^oC.

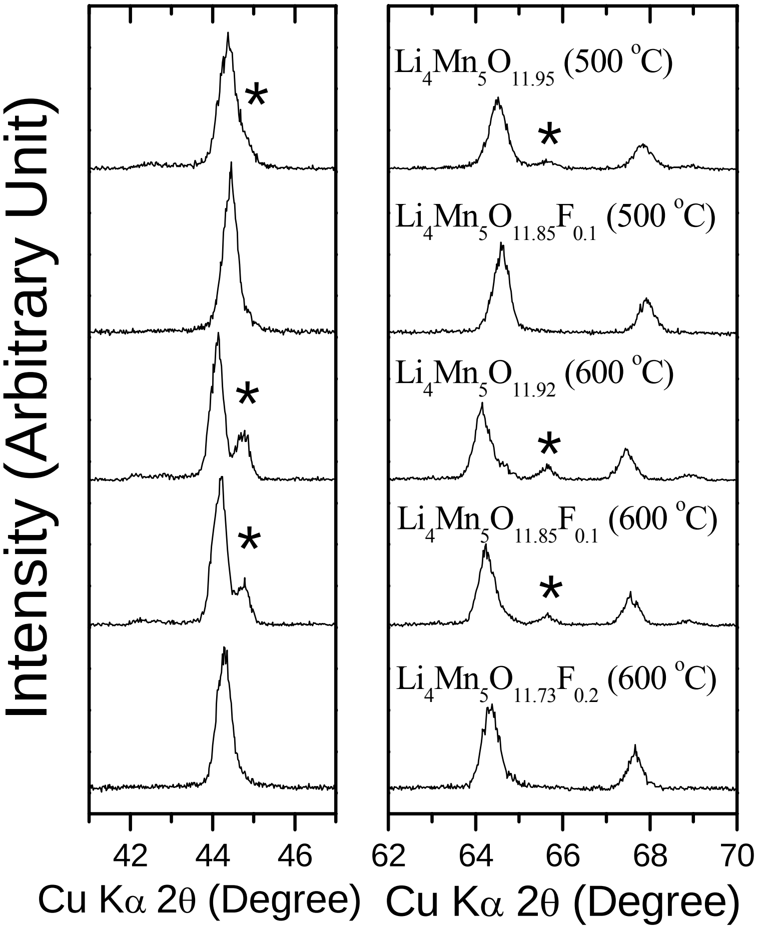

Figure 7.2 XRD patterns of the $Li_4Mn_5O_{12-\eta}F_\eta$ samples over a small 2θ range. The reflections marked with * refer to the Li_2MnO_3 phase while others refer to the cubic spinel phase.

7.3.2 Cycling Performance in the $LiClO_4$ Electrolyte System

Figure 7.3 compares the discharge curves of the oxide and oxyfluoride cathodes synthesized at 500 °C. The data were collected at room temperature in the range of 3.3 – 2.4 V with 1 M $LiClO_4$ in 1:1 PC and DME electrolyte at C/5 rate, and the initial capacity values and the % capacity loss after 50 cycles are given in Table 7.1. The $Li_4Mn_5O_{11.85}F_{0.1}$ oxyfluoride sample shows slightly higher capacity and improved capacity retention compared to the $Li_4Mn_5O_{11.95}$ oxide sample. For example, $Li_4Mn_5O_{11.85}F_{0.1}$ exhibits an initial capacity of 158 mAh/g with a capacity fade of 2.9 % in 50 cycles compared to 151 mAh/g and 5.1 % fade for $Li_4Mn_5O_{11.95}$. Similar trends could be found for the oxide and oxyfluoride samples synthesized at 600 ^{o}C as seen in Fig. 7.4 and Table 7.1. For example, $Li_4Mn_5O_{11.85}F_{0.1}$ synthesized at 600 ^{o}C exhibits 150 mAh/g with a capacity fade of 3.8 % in 50 cycles compared to 139 mAh/g and 4.7 % fade for $Li_4Mn_5O_{11.92}$ synthesized at 600 ^{o}C due to the suppression of the electrochemically inactive phase Li_2MnO_3. However, a further increase in fluorine content as in $Li_4Mn_5O_{11.73}F_{0.2}$ results in a significant increase in capacity fade (8.4 % in 50 cycles), possibly due to a decreased initial Mn valence and the occurrence of Jahn-Teller distortion towards the end of discharge.

Figure 7.5 compares the XRD patterns of $Li_4Mn_5O_{11.95}$ and $Li_4Mn_5O_{11.85}F_{0.1}$ cathodes synthesized at 500 ^{o}C after 50 cycles at room temperature. Compared to the data in Figs. 7.1 and 7.2, the reflections corresponding to the Li_2MnO_3 phase become much more prominent after the electrochemical cycling, particularly in the oxide sample $Li_4Mn_5O_{11.95}$. The intensity of the Li_2MnO_3 reflection is smaller in the oxyfluoride sample $Li_4Mn_5O_{11.85}F_{0.1}$ compared to that in the oxide sample

$Li_4Mn_5O_{11.95}$ in Fig.7.5. The suppression of the development of the Li_2MnO_3 phase during cycling leads to better capacity retention for the oxyfluoride sample.

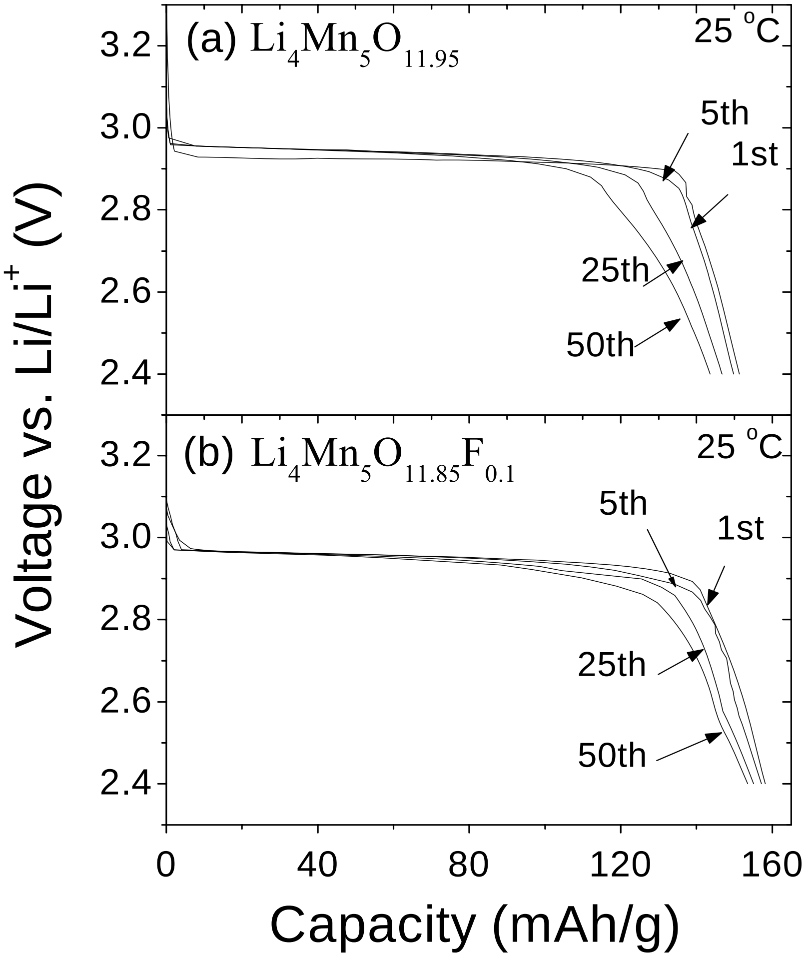

Figure 7.3 Discharge curves of the $Li_4Mn_5O_{12-\eta}F_\eta$ cathodes synthesized at 500 °C. The data were collected in 1 M $LiClO_4$ in 1:1 PC and DME electrolyte between 3.3 and 2.4 V at room temperature.

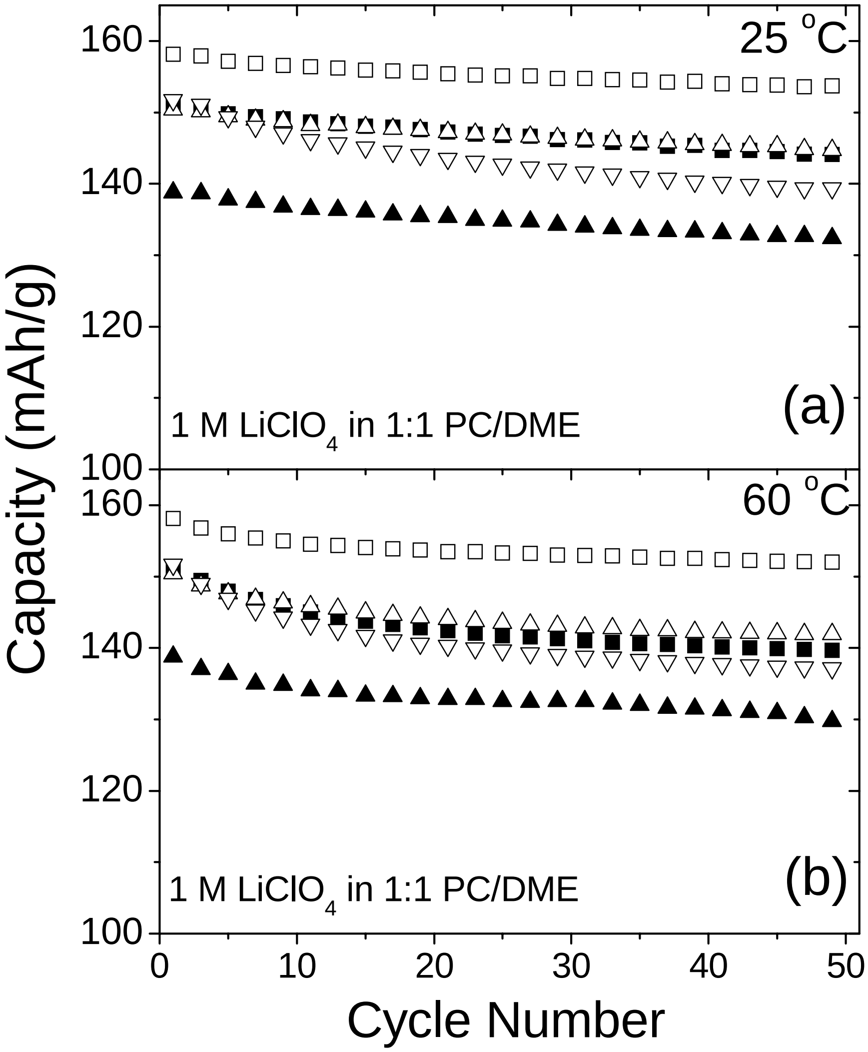

Figure 7.4 Comparison of the electrochemical cycling performances at (a) 25 °C and (b) 60 °C of $Li_4Mn_5O_{12-\eta}F_\eta$ in 1 M $LiClO_4$ in 1:1 PC and DME electrolyte: (■) $Li_4Mn_5O_{11.95}$ synthesized at 500 °C, (□) $Li_4Mn_5O_{11.85}F_{0.1}$ synthesized at 500 °C, (▲) $Li_4Mn_5O_{11.92}$ synthesized at 600 °C, (△) $Li_4Mn_5O_{11.85}F_{0.1}$ synthesized at 600 °C, and (▽) $Li_4Mn_5O_{11.73}F_{0.2}$ synthesized at 600 °C.

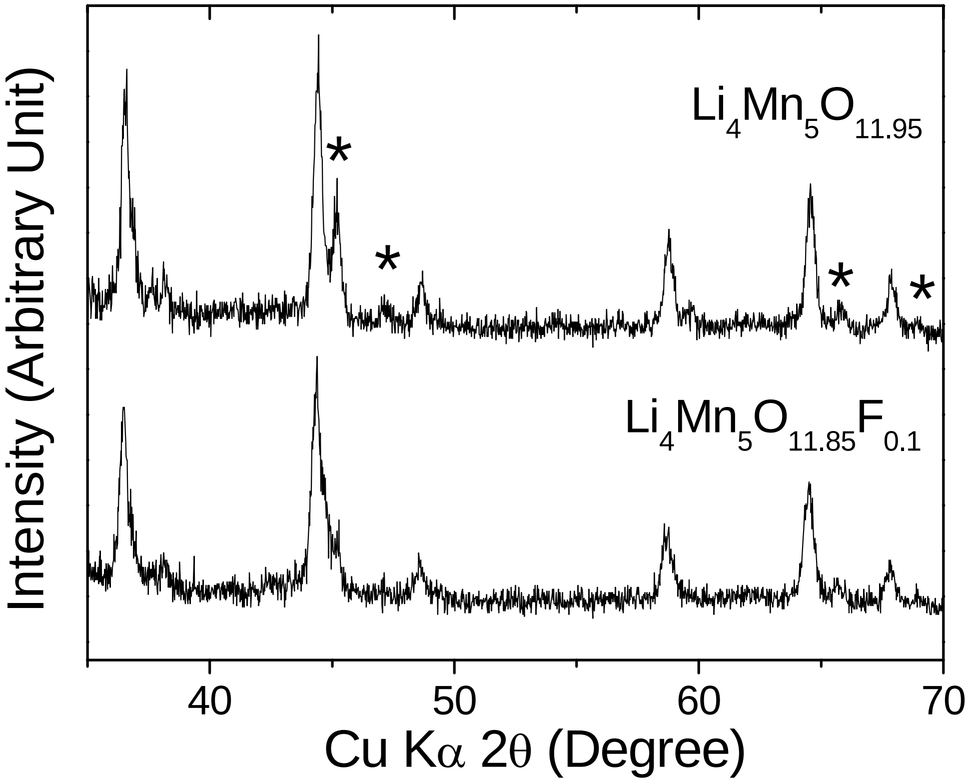

Figure 7.5 XRD patterns of the $Li_4Mn_5O_{12-\eta}F_\eta$ cathodes in the fully charged state after 50 cycles at room temperature in 1 M $LiClO_4$ in 1:1 PC and DME electrolyte.

7.3.3 Cycling Performance in the $LiPF_6$ Electrolyte System

Lithium ion cells generally employ the $LiPF_6$ in EC and DEC electrolyte, but the trace amount of HF formed by a reaction of $LiPF_6$ with the trace amount of water present in the electrolyte is known to enhance the manganese dissolution through a disproportionation of Mn^{3+} into Mn^{2+} and Mn^{4+}.[24] In order to assess the impact of such dissolution, electrochemical evaluation with the $LiPF_6$-based electrolyte at both room and elevated temperatures were carried out. Figure 7.6 compares the cycling performances of the $Li_4Mn_5O_{12-\eta}F_\eta$ oxyfluoride cathodes at 25 and 60 °C at C/5 rate with the $LiPF_6$ in 1:1 EC and DEC electrolyte, while Table 1 gives the initial capacity values and the % capacity loss after 50 cycles. Figure 7.7 compares the cycling performances of selected $Li_4Mn_5O_{12-\eta}F_\eta$ cathodes in $LiClO_4$- and $LiPF_6$-based electrolytes at 25 and 60 °C at C/5 rate. The oxyfluoride cathodes exhibit higher capacity and better capacity retention (at low fluorine contents) compared to the oxide analogs at both 25 and 60 °C in the $LiPF_6$-based electrolyte also similar to that found with the $LiClO_4$-based electrolyte in Figs. 7.3 and 7.4. For example, $Li_4Mn_5O_{11.85}F_{0.1}$ synthesized at 600 °C exhibits a capacity fade of 12.1 % in 50 cycles at 60 °C compared to 18.3 % for the corresponding oxide $Li_4Mn_5O_{11.92}$, although $Li_4Mn_5O_{11.85}F_{0.2}$ with a higher fluorine content exhibits a significantly higher fade of 21.1 % due to a lower initial oxidation state of manganese and the possible occurrence of Jahn-Teller distortion towards the end of discharge.

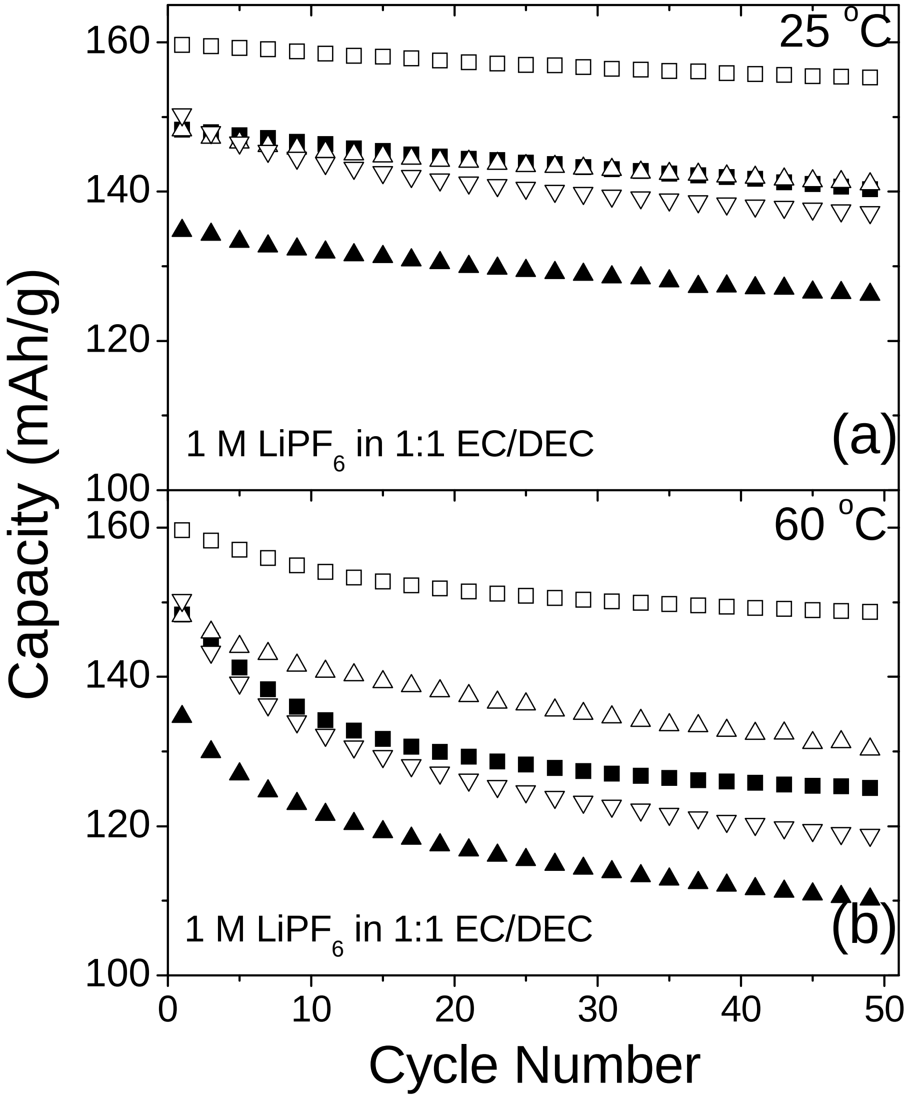

Figure 7.6 Comparison of the electrochemical cycling performances at (a) 25 °C and (b) 60 °C of $Li_4Mn_5O_{12-\eta}F_\eta$ in 1 M $LiPF_6$ in 1:1 EC and DEC electrolyte: (■) $Li_4Mn_5O_{11.95}$ synthesized at 500 °C, (□) $Li_4Mn_5O_{11.85}F_{0.1}$ synthesized at 500 °C, (▲) $Li_4Mn_5O_{11.92}$ synthesized at 600 °C, (△) $Li_4Mn_5O_{11.85}F_{0.1}$ synthesized at 600 °C, and (▽) $Li_4Mn_5O_{11.73}F_{0.2}$ synthesized at 600 °C.

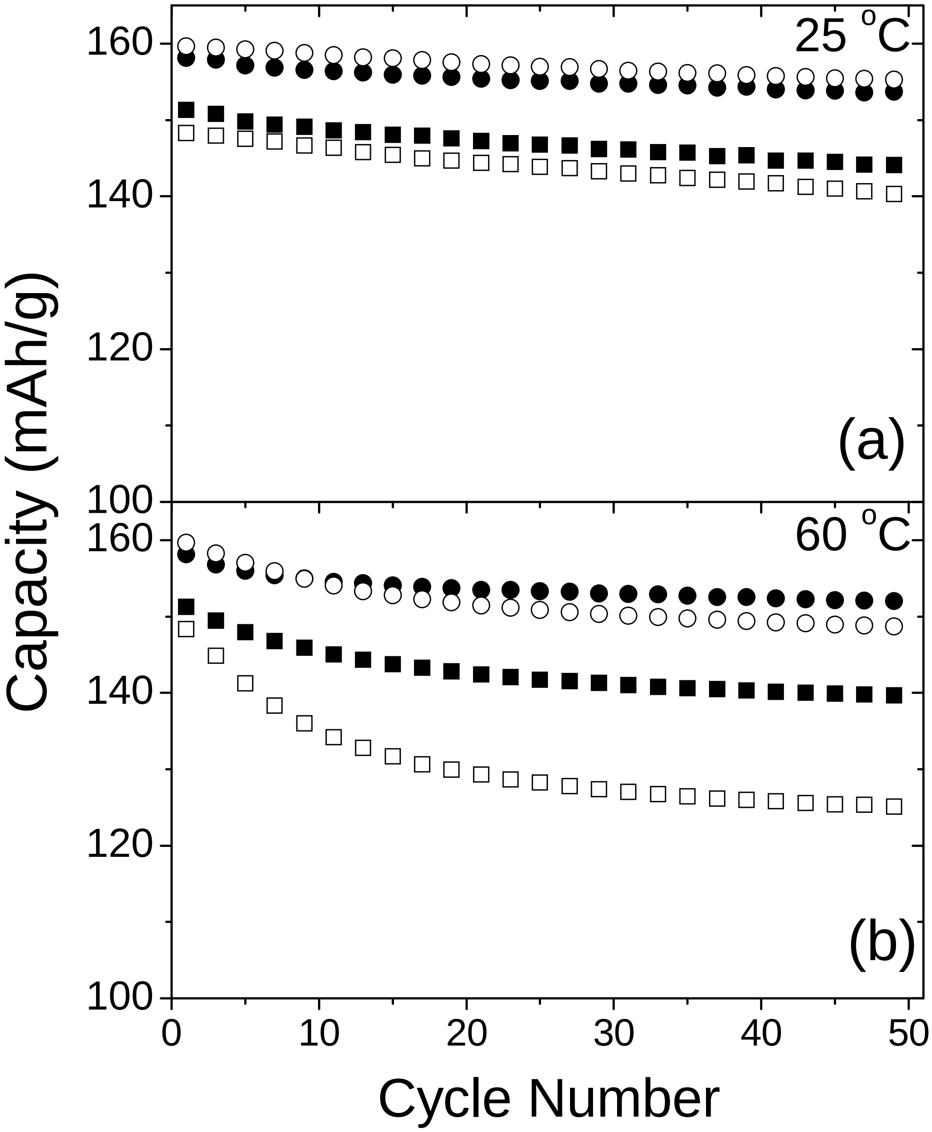

Figure 7.7 Comparison of the electrochemical cycling performances at (a) 25 °C and (b) 60 °C of $Li_4Mn_5O_{12-\eta}F_\eta$ in $LiClO_4$ and $LiPF_6$ electrolytes: (■) $Li_4Mn_5O_{11.95}$ synthesized at 500 °C in $LiClO_4$ electrolyte, (□) $Li_4Mn_5O_{11.95}$ synthesized at 500 °C in $LiPF_6$ electrolyte, (●) $Li_4Mn_5O_{11.85}F_{0.1}$ synthesized at 500 °C in $LiClO_4$ electrolyte, and (○) $Li_4Mn_5O_{11.85}F_{0.1}$ synthesized at 500 °C in $LiPF_6$ electrolyte.

7.3.4 Manganese Dissolution

The degree of manganese dissolution was evaluated after storing the coin cells fabricated with metallic lithium anode at the fully discharged state after the first discharge for 7 days at 60 ^{o}C, and the data are given in Table 7.1. While the Mn dissolution values are very small and remain nearly the same (~ 0.11 %) in the $LiClO_4$ electrolyte, the Mn dissolution values are higher (up to 0.97 %) in the $LiPF_6$ electrolyte. Interestingly, the oxyfluorides exhibit a lower Mn dissolution compared to the oxide analogs in the $LiPF_6$ electrolyte. However, the Mn dissolution increases on going from $Li_4Mn_5O_{11.85}F_{0.1}$ (synthesized at 600 ^{o}C) to $Li_4Mn_5O_{11.73}F_{0.2}$ due to a decrease in the initial Mn valence. These observations of decrease in Mn dissolution with fluorine substitution are consistent with those found with the 4 V spinel oxyfluoride cathodes as well.[157,158]

7.4 CONCLUSIONS

The substitution of a small amount of F^- ions for O^{2-} ions in the spinel $Li_4Mn_5O_{12}$ is found to suppress the disproportionation of $Li_4Mn_5O_{12}$ into $Li_{1+x}Mn_{2-x}O_4$ ($x < 0.33$) and Li_2MnO_3 during synthesis at 500 and 600 ^oC. The $Li_4Mn_5O_{12-\eta}F_\eta$ oxyfluoride cathodes exhibit higher capacity and better capacity retention at both 25 and 60 ^oC compared to the oxide analogs due to the suppression of the Li_2MnO_3 phase and reduced Mn dissolution from the lattice. The findings are consistent with the increased capacity and improved capacity retention found before with the 4 V $LiMn_2O_4$ spinel system.[157,158] However, the capacity fade increase at higher fluorine contents due to a lowering of the Mn oxidation state and the possible occurrence of Jahn-Teller distortion towards the end of discharge.

CHAPTER 8

SUMMARY

With an aim to develop a firm understanding of the factors that control and limit the electrochemical performance properties such as the reversible capacity, cyclability, and rate capability of the spinel cathodes, various spinel $LiMn_{2-y-z}Li_yM_zO_{4-\eta}F_\eta$ (M = Al, Ti, Ni, Cu, Zn, and F) cathodes have been investigated.

A systematic investigation of the transition metal ion dissolutions from layered, orthorhombic $LiMnO_2$, 4 V spinel, 5 V spinel, and olivine $LiFePO_4$ cathodes reveal that a larger amount of manganese dissolution occurs in the case of cathodes containing Mn^{3+} while other cathodes such as oxides containing Mn^{4+}, $LiCoO_2$ and $LiFePO_4$ exhibit negligible amount of total metal ion dissolution. Although the Mn^{3+}-containing spinel cathodes show large manganese dissolution, this could be reduced significantly through cationic and anionic substitutions. The reduced manganese dissolution leads to excellent capacity retention at elevated temperatures for cathode compositions such as $LiMn_{2-y-z}Li_yM_zO_{4-\eta}F_\eta$. Also, the reduction of manganese dissolution in such $LiMn_{2-y-z}Li_yM_zO_{4-\eta}F_\eta$ spinels is accompanied by a much smaller lattice parameter difference Δa between the two cubic phases formed during the charge-discharge process, exhibiting a clear relationship between the manganese dissolution and Δa. Although anionic (fluorine) substitutions employing LiF as a fluorine source lead to a significant improvement in the electrochemical performance, a systematic investigation of other fluorine sources or lower temperature approaches is desirable due to the volatilization of fluorine at high synthesis temperatures.

With an aim to increase the fluorine content incorporated into the spinel lattice, fluorine substitution employing ZnF_2 has been pursed. The electrochemical characterization of the $LiMn_{2-y-z}Li_yZn_zO_{4-\eta}F_\eta$ ($0 \leq y \leq 0.1$, $0 \leq z \leq 0.1$, and $0 \leq \eta \leq 0.18$) spinel oxyfluoride cathodes synthesized at 800 ^{o}C employing ZnF_2 indicates that the oxyfluorides exhibit up to 10 mAh/g higher capacity than the corresponding oxide analogs due to a decrease in the initial manganese valence with an enhanced capacity retention. Excellent capacity retention at elevated temperatures with capacities of over 100 mAh/g was found in the optimized oxyfluoride compositions such as $LiMn_{1.85}Li_{0.075}Zn_{0.075}O_{3.85}F_{0.15}$. Evaluation of the Mn dissolution and chemical delithiation data reveal that the improved reversible capacity and capacity retention of the $LiMn_{2-y-z}Li_yZn_zO_{4-\eta}F_\eta$ oxyfluoride cathodes is due to suppressed manganese dissolution and a smaller instantaneous volume change between the two cubic phases formed during the charge-discharge process. Instantaneous volume change and manganese dissolution in the spinel cathode could be related to the interfacial strain and loss of crystallinity on cycling, leading to impedance growth and capacity fade. Fluorine incorporation using ZnF_2 suppresses the volatilization of fluorine during synthesis compared to the conventional methods of employing LiF although fluorine loss is still found with ZnF_2 due to the high temperature synthesis.

In an effort to maximize the substitution of fluoride for oxide ion in the spinel lattice, a low temperature approach has then been pursed. Spinel $LiMn_{2-y-z}Li_yNi_zO_{4-\eta}F_\eta$ (M = Ti, and Ni, $0 \leq \eta \leq 0.29$) oxyfluorides cathodes synthesized by firing the cation-substituted $LiMn_{2-y-z}Li_yNi_zO_4$ oxide analogs with the fluorinating agent NH_4HF_2 at a moderate temperature of 450 ^oC have been found to exhibit an increase in the reversible capacity, much better capacity retention, rate capability, and storage characteristics as well as low irreversible capacity loss in the first cycle compared to $LiMn_2O_4$. X-ray diffraction and chemical analysis reveal that the amount of fluorine that could be incorporated into the spinel lattice depends on the Mn valence above 3.5+. A significant suppression of the lattice mismatch between the two cubic phases formed during the charge-discharge process, much lower Mn dissolution, and maintenance of better crystallinity during cycling were found to be the reason for the improvement in the electrochemical performances of the oxyfluoride cathodes thus prepared. Optimized spinel compositions such as $LiMn_{1.8}Li_{0.1}Ni_{0.1}O_{3.8}F_{0.2}$ exhibit superior electrochemical properties with capacities of over 100 mAh/g. However, a further increase in fluorine content as in $LiMn_{1.8}Li_{0.1}Ni_{0.1}O_{3.71}F_{0.29}$ degrades the electrochemical performance due to a lowering of initial Mn valence and a larger lattice mismatch and Mn dissolution.

Electrochemical characterization of spinel and layered oxide composite cathodes has been pursed to suppress Mn dissolution and improve the capacity retention of spinel cathodes further. The addition of a moderate amount of a layered oxide like $LiCoO_2$ to an optimized spinel oxyfluoride composition like $LiMn_{1.8}Li_{0.1}Ni_{0.1}O_{3.8}F_{0.2}$

followed by charging to high enough voltages (4.7 V) during first charge leads to superior capacity retention at 60 ^{o}C in lithium ion cells fabricated with graphite anode. Evaluation of Mn dissolution reveals that the trapping of trace amounts of protons that may be present in the electrolyte within the layered oxide lattice during the first charge to 4.7 V suppresses the Mn dissolution and improves the electrochemical performance significantly.

Utilizing the knowledge gained with the 4 V spinel oxyfluoride system, 3 V $Li_4Mn_5O_{12-\eta}F_\eta$ $(0 \leq \eta \leq 0.2)$ cathodes have been synthesized employing LiF. X-ray diffraction analysis reveals that fluorine substitution leads to a suppression of the disproportionation of $Li_4Mn_5O_{12}$ oxide samples into lithium-rich spinel $Li_{1+x}Mn_{2-x}O_4$ and Li_2MnO_3 during synthesis. Electrochemical characterization reveals that the fluorine substituted cathodes exhibit an increase in initial capacity and improved capacity retention with the $LiClO_4$ electrolyte system compared to the corresponding oxide analogs due to a reduction in the amount of the Li_2MnO_3 phase and a suppression of the development of the Li_2MnO_3 phase during cycling. Electrochemical performance data collected with the $LiPF_6$ electrolyte system reveals that fluorine incorporation into 3 V $Li_4Mn_5O_{12-\eta}F_\eta$ spinel cathodes also leads to a reduction in Mn dissolution and consequent improvement in capacity retention, exhibiting a tendency similar to that of 4 V $LiMn_{2-y-z}Li_yM_zO_{4-\eta}F_\eta$ spinel cathodes.

Overall, the electrochemical performances of the spinel cathodes are controlled by manganese dissolution and the lattice parameter mismatch during charge-discharge process as well as initial Mn valence, and the problems can be minimized through appropriate cationic and anionic substitutions. Especially, fluorine substitution is found to be effective as it improves the capacity retention and compensates for the capacity values sacrificed by the cationic substitutions, and the spinel-layered oxide composite cathodes improve the electrochemical performance of spinel cathodes further. Considering these findings, development of further optimized oxyfluoride compositions may make them attractive for HEV and EV applications. Future experiments could focus on optimization of the microstructure with novel synthesis and processing as well as on a systematic investigation of the spinel-layered oxide composite cathodes to improve the electrochemical performances of the spinel cathodes further.

REFERENCES

1. J. O. Besenhard, Editor, *Handbook of battery Materials*, Wiley-VCH, Weinheim (1999).
2. D. Linden and T. B. Reddy, Editors, *Handbook of Batteries*, 3rd Ed. McGraw-Hill, New York (2001).
3. http://www.rcbatteryclinic.com/seminar.htm
4. http://en.wikipedia.org
5. http://www.toyota.com
6. T. Nagaura, M. Nagamine, I. Tanabe, and N. Miyamoto, *Prog. Batt. Solar Cells*, **8**, 84 (1989).
7. T. Nagaura and K. Tozawa, *Prog. Batt. Solar Cells*, **9**, 209 (1990).
8. K. Mizushima, P. C. Jones, P. J. Wiseman, and J. B. Goodenough, *Mat. Res. Bull.*, **15**, 783 (1980).
9. J. O. Besenhard, *Carbon*, **14**, 93 (1976).
10. F. Orsini, A. du Pasquier, B. Beaudouin, J. M. Tarascon, M. Trentin, N. Langenhuizen, E. de Beer, and P. Notten, *J. Power Sources*, **81**, 918 (1999).
11. J. M. Tarascon and D. Guymard, *J. Electrochem. Soc.*, **138**, 2864 (1991).
12. J. R. Dahn, U. von Sacken, M. W. Juzkow, and H. Al-Janaby, *J. Electrochem. Soc.*, **138**, 2207 (1991).

13. K. Ozawa, *Solid State Ionics*, **69**, 212 (1994).

14. J. R. Dahn, U. von Sacken, and C. A. Michal, *Solid State Ionics*, **44**, 87 (1990).

15. R. J. Gummow and M. M. Thackery, *Solid State Ionics*, **53-56**, 681 (1992).

16. E. Rossen, C. W. Jones, and J. R. Dahn, *Solid State Ionics*, **57**, 311 (1992).

17. C. Delmas, I. Saadoune, and A. Rougier, *J. Power Sources*, **43-44**, 595 (1993).

18. T. Ohzuku, A. Ueda, M. Nagayama, Y. Iwakoshi and H. Komori, *Electochem. Acta.*, **38**, 1159 (1993).

19. E. Zhecheva and R. Stoyanova, *Solid State Ionics*, **66**, 143 (1993).

20. M. Yoshio, H. Noguchi, J. Itoh, M. Okada, and Y. Mouri, *J. Power Sources*, **90**, 176 (2000).

21. T. Ohzuku and Y. Makimura, *Chem. Lett.*, **8**, 744 (2001).

22. T. Ohzuku and Y. Makimura, *Chem. Lett.*, **7**, 642 (2001).

23. A. K. Padhi, K. S. Nanjundaswamy, and J. B. Goodenough, *J. Electrochem. Soc.*, **144**, 1188 (1997).

24. A. Yamada, S. C. Chung, and K. Hinokuma, *J. Electrochem. Soc.*, **148**, A224 (2001).

25. M. M. Thackery, W. I. F. David, P. G. Bruce, and J. B. Goodenough, *Mater. Res. Bull.*, **18**, 461 (1983).

26. D. H. Jang, Y. J. Shin, and S. M. Oh, *J. Electrochem. Soc.*, **143**, 2204 (1996).

27. E. J. Wu, P. D. Tepesch, and G. Ceder, *Philosophical Magazine B*, **77**, 1039 (1998).

28. J. N. Reimers and J. R. Dahn, *J. Electrochem. Soc.*, **131**, 2091 (1992).

29. G. G. Amatucci, J. M. Tarascon, and L. C. Klein, *J. Electrochem. Soc.*, **143**, 1114 (1996).

30. R. V. Chebiam, A. M. Kannan, F. Prado and A. Manthiram, Electrochem. Commun., **3**, 624 (2001).

31. R. V. Chebiam, F. Prado and A. Manthiram, *Chem. Mater.*, **13**, 2951 (2001).

32. J. Choi and A. Manthiram, *J. Electrochem. Soc.*, **152**, A1714 (2005).

33. J. Choi and A. Manthiram, , *Solid State Ionics*, **176**, 2251 (2005).

34. J. Morales, C. Perez-Vincente, and J. L. Tirado, *Mat. Res. Bull.*, **25**, 623 (1990).

35. M. S. Whittingham, U. S. Patent 4049887 (1996).

36. A. H. Thompson and M. S. Whittingham, *Mater. Res. Bull.*, **12**, 741 (1977).

37. A. J. Jacobson and M. S. Whittingham, U. S. Patent 4143213 (1978).

38. M. S. Whittingham, *Prog. Solid State Chem.*, **12**, 41 (1978).

39. N. Ravet, J. B. Goodenough, S. Besner, M. Simoneau, P. Hovington, and M. Armand, *Electrochem. Soc. Abstr.*, 99-2, 127 (1999).

40. N. Ravet, S. Besner, M. Simoneau, A. Vallee, M. Armand, and J.-F.Magnan, European Patent 1049182A2 (2000).

41. H. Huang, S. -C. Yin, and L. F. Nazar, *Electrochem. Solid State Lett.*, **4**, A170 (2001).

42. L. J. Fu, H. Liu, C. Li, Y. P. Wu, E. Rahm, R. Holze, and H. Q. Wu, *Solid State Sciences*, **8**, 113 (2006).

43. D. W. Murphy, M. Greenblatt, S. M. Zahurak, R. J. Cava, J. V. Waszczak, G. W. Hull, and R. S. Hutton, *Rev. Chim. Miner.*, **19**, 441 (1982).

44. P. P. Prosini, R. Mancini, L. Petrucci, V. Contini, and P. Villano, *Solid State Ionics*, **144**, 185 (2001).

45. H. Morimoto, M. Nakai, M. Tatsumisago, and T. Minami, *J. Electrochem. Soc.*, **146**, 3970 (1999).

46. N. P. Yao, L. A. heredy, and R. C. Saunders, *J. Electrochem. Soc.*, **118**, 1039 (1971).

47. C. J. Wen, B. A. Boukamp, R. A. Huggins, and W. Weppener, *J. Electrochem. Soc.*, **126**, 2258 (1979).

48. C. J. Wen and R. A. Huggins, *J. Solid State Chem.*, **37**, 271 (1981).

49. J.-J. Zhang and Y.-Y. Xia, *J. Electrochem. Soc.*, **153**, A1466 (2006).

50. http://www.physorg.com/news3061.html

51. R. A. Huggins, *Solid State Ionics*, **152**, 61 (2002).

52. M. Wakihara and O. Yamamoto, Editors, *Lithium Ion Batteries Fundamentals and Performance*, Wiley-VCH, Weinheim (1998).

53. http://berc.lbl.gov/BATT.html.

54. http://www.shinkobe-denki.co.jp/100.en/

55. G. Pistoia, and D. Wang, *Solid State Ionics,* **66**, 135 (1993).

56. M. M. Thackeray, *J. Electrochem. Soc.,* **142**, 2558 (1995).

57. M. M. Thackeray, Y. Shao-Horn, A. J. Kahaian, K. D. Kepler, E. Skinner, J. T. Vaugney, and S. A. Hackney, *Electrochem. Solid-State Lett.*, **1**, 7 (1998**)**.

58. A. de Kock, M. H. Rossouw, L. A. de Picciotto, M. M. Thackeray, W. I. F. David, and R. M. Ibberson, *Mat. Res. Bull.*, **25**, 657 (1990).

59. M. H. Rossouw, A. de Kock, L. A. de Picciotto, M. M. Thackeray, W. I. F. David, and R. M. Ibberson, *Mat. Res. Bull.*, **25**, 173 (1990).

60. S. Choi and A. Manthiram, *J. Electrochem. Soc.*, **147**, 1623 (2000).

61. J. Kim and A. Manthiram, *J. Electrochem. Soc.*, **145**, L53 (1998).

62. M. M. Thackeray, A. de Kock, M. H. Rossouw, D. C. Liles, D. Hoge, and R. Bittihn, *J. Electrochem. Soc.*, **139**, 363 (1992).

63. Y. Shao-Horn, S. A. Hackney, C. S. Johnson, A. J. Kahaian, and M. M. Thackeray, *J. Solid State Chem.*, **140**, 116 (1998).

64. M. M. Obrovac, Y. Gao, and J. R. Dahn, *Phys. Rev. B,* **57**, 5728 (1998).

65. C. Sigala, D. Guyomard, A. Verbaere, Y. Diffard, and M. Tournoux, *Solid State Ionics*, **81**, 167 (1995).

66. H. Kawai, M. Nagata, M. Tabuchi, H. Tukamoto, and A. R. West, *Chem. Mater*., **10**, 3266 (1998).

67. Y. Gao, K. Myrtle, M. Zhang, J. N. Reimers, and J. R. Dahn, *Phys. Rev. B,* **54**, 16670 (1996).

68. Q. Zhong, A Banakdarpour, M. Zhang, Y. Gao, and J. R. Dahn, *J. Electrochem. Soc.*, **144**, 205 (1997).

69. Y. Ein-Eli and W. F. Howard, Jr., *J. Electrochem. Soc.*, **144**, L205 (1997).

70. Y. Ein-Eli, W. F. Howard, Jr., S. H. Lu, S. Mukerjee, J. McBreen, J. T. Vaughey, and M. M. Thackeray, *J. Electrochem. Soc.*, **145**, 1238 (1998).

71. Y. Ein-Eli, J. T. Vaughey, M. M. Thackeray, S. Mukerjee, X. Q. Yang, and J. McBreen, *J. Electrochem. Soc.*, **146**, 908 (1999).

72. H. Kawai, M. Nagata, H. Tukamoto, H. Kageyama, and A. R. West, *Electrochim. Acta*, **45**, 315 (1999).
73. H. Kawai, M. Nagata, H. Tukamoto, and A. R. West, *J. Power Sources*, **81-82**, 67 (1999).
74. T. Ohzuku, S. Takeda, and M. Iwanaga, *J. Power Sources*, **81-82**, 90 (1999).
75. H. Shigemura, H. Sakaebe, H. Kageyama, H. Kobayashi, A. R. West, R. Kanno, S. Morimoto, S. Nasu, and M. Tabuchi, *J. Electrochem. Soc.*, **148**, A730 (2001).
76. Y. Idemoto, H. Narai, and N. Koura, *J. Power Sources*, **119-121**, 125 (2003).
77. A. Eftekhari, *J. Power Sources*, **124**, 182 (2003).
78. J. M. Lloris, B. León, C. P. Vicente, J. L. Tirado, M. Womes, J. O. Fourcade, and J. C. Jumas, *J. Solid State Electochem.*, **8**, 521 (2004).
79. R. Alcántara, M. Jaraba, P. Lavela, and J. L. Tirado, *J. Electrochem. Soc.*, **151**, A53 (2004).
80. S.-W. Oh, S.-H. Park, J.-H Kim, Y.-C. Bae, and Y.-K. Sun, *J. Power Sources*, **119-121**, 125 (2003).
81. S.-C. Park, Y.-S. Han, Y.-S. Kang, P.-S. Lee, S. Ahn, H.-M. Lee, and J.-Y. Lee, *J. Electrochem. Soc.*, **148**, A680 (2001).
82. Y. Xia, Y. Zhou, and M. Yoshio, *J. Electrochem. Soc.*, **144**, 2593 (1997).
83. T. Inoue and M. Sano, *J. Electrochem. Soc.*, **145**, 3704 (1998).
84. H. Yamane, T. Inoue, M. Fujita, and M. Sano, *J. Power Sources*, **99**, 60 (2001).
85. T. Aoshima, K. Okahara, C. Kiyohara, and K. Shizuka, *J. Power Sources*, **97-98**, 377 (2001).

86. Z. Liu, H. Wang, L. Fang, J. Y. Lee, and L. M. Gam, *J. Power Sources*, **104**, 101 (2002).

87. S. Komaba, N. Kumagai, T. Sasaki, and Y. Miki, *Electrochemistry*, **69**, 787 (2001).

88. H. Tsunekawa, S. Tanimoto, R. Marubayashi, M. Fujita, K. Kifune, and M. Sano, *J. Electrochem. Soc.*, **149**, A1326 (2002).

89. L.-F. Wang, C.-C. Ou, K. A. Striebel, and J.-S. Chen, *J. Electrochem. Soc.*, **150**, A905 (2003).

90. S. Komaba, B. Kaplan, T. Ohtsuka, Y. Kataoka, N. Kumagai, and H. Groult, *J. Power Sources*, **119-121**, 378 (2003).

91. M. Saitoh, M. Sano, M. Fujita, M. Sakata, M. Takata, and E. Nishibori, *J. Electrochem. Soc.*, **151**, A17 (2004).

92. M.-S. Wu, P.-C. J. Chiang, and J.-C. Lin, *J. Electrochem. Soc.*, **152**, A1041 (2005).

93. L.-F. Wang, B.-J. Fang, and J.-S. Chen, *J. Power Sources*, **150**, 1 (2005).

94. J. C. Hunter, *J. Solid State Chem.*, **39**, 142 (1981).

95. M. M. Thackeray, *J. Am. Ceram. Soc.*, **82**, 3347 (1999).

96. T. Ohzuku, M. Kitagawa, and T. Hirai, *J. Electrochem. Soc.*, **137**, 769 (1990).

97. J. Cho and M. Thackeray, *J. Electrochem. Soc.*, **146**, 3577 (1999).

98. M. D. Levi, K. Gamolsky, D. Aurbach, U. Heider, and R. Oesten, *J. Electrochem. Soc.*, **147**, 25 (2000).

99. Y.-K. Sun, C. S. Yoon, C. K. Kim, S. G. Youn, Y.-S. Lee, M. Yoshio, and I. H. Oh, *J. Mater. Chem.*, **11**, 2519 (2001).

100. H. Huang, C. A. Vincent, and P. G. Bruce, P. G. *J. Electrochem. Soc.*, **146**, 3649 (1999).

101. D. Aurbach, M. D. Levi, K. Gamulski, B. Markovsky, G. Salitra, E. Levi, U. Heider, L. Heider, and R. Oesten, *J. Power Sources*, **81**, 472 (1999).

102. Y. Shin, and A. Manthiram, *Electrochem. Solid-State Lett.*, **5**, A55 (2002).

103. Y. Shin, and A. Manthiram, *Electrochem. Solid-State Lett.*, **6**, A34 (2003).

104. Y. Shin, and A. Manthiram, *Chem. Mater.*, **15**, 2954 (2003).

105. Y. Shin, and A. Manthiram, *J. Electrochem. Soc.*, **151**, A204 (2004).

106. A. Yamada, K. Miura, K. Hinokuma, and M. Tanaka, *J. Electrochem. Soc.*, **142**, 2149 (1995).

107. Y. Xia, and M. Yoshio, *J. Power Sources*, **66**, 129 (1997).

108. J. H. Lee, J. K. Hong, D. H. Jang, Y. K. Sun, and S. M. Oh, *J. Power Sources*, **89**, 7 (2000).

109. R. J. Gummow, A. de Kock, and M. M. Thackeray, *Solid State Ionics*, **69**, 59 (1994).

110. X. Sun, X. Q. Yang, M. Balasubramanian, J. McBreen, Y. Xia, and T. Sakai, *J. Electrochem. Soc.*, **149**, A842 (2002).

111. G. Pistoia, A. Antonini, R. Rosati, C. Bellitto, and G. M. Ingo, *Chem. Mater.*, **9**, 1443 (1997).

112. A. de Kock, E. Ferg, and R. J. Gummow, *J. Power Sources*, **70**, 247 (1998).

113. L. Hernan, J. Morales, L. Sanchez, and J. Santos, *Solid State Ionics*, **118**, 179 (1999).

114. Y.-S. Lee, N. Kumada, and M. Yoshio, *J. Power Sources*, **96**, 376 (2001).

115. B. J. Hwang, R. Santhanam, and S. G. Hu, *J. Power Sources*, **108**, 250 (2002).

116. M. Okada, Y.-S. Lee, and M. Yoshio, *J. Power. Sources*, **90**, 196 (2000).

117. H. J. Bang, V. S. Donepudi, and J. Prakash, *Electrochim. Acta*, **48**, 443 (2002).

118. Y.-S. Hong, C.-H. Han, K. Kim, C.-W. Kwon, G. Campet, and J.-H. Choy, *Solid State Ionics*, **139**, 75 (2001).

119. A. D. Robertson, S. H. Lu, and W. F. Howard, Jr., *J. Electrochem. Soc.*, **144**, 3505 (1997).

120. J.-S. Kim, J. T. Vaughey, C. S. Johnson, and M. M. Thackeray, *J. Electrochem. Soc.*, **150**, A1498 (2003).

121. S.-H. Park, S.-W. Oh, S.-T. Myung, and Y.-K. Sun, *Electrochem. Solid-State Lett.*, **7**, A451 (2004).

122. F. Zhou, X. Zhao, H. Zheng, Z. Zhang, and M. Ji, *Materials Letters*, **58**, 3720 (2004).

123. S. Nieto, S. B. Majumder, and R. S. Katiyar, *J. Power. Sources*, **136**, 88 (2004).

124. H. Zhan and Y. Zhou, *Materials Letters*, **58**, 3276 (2004).

125. K. Y. Chung, W.-S. Yoon, H. S. Lee, X.-Q. Yang, J. McBreen, B. H. Deng, X. Q. Wang, M. Yoshio, R. Wang, J. Gui, and M. Okada, *J. Power. Sources*, **146**, 226 (2005).

126. Z. Chen and K. Amine, *J. Electrochem. Soc.*, **153**, A316 (2006).

127. B. J. Hwang, R. Santhanam, D. G. Liu, and Y. W. Tsai, *J. Power. Sources*, **102**, 326 (2001).
128. J.-F. Lee, Y.-W. Tsai, R. Santhanam, B. J. Hwang, M.-H. Yang, and D.-G. Liu, *J. Power. Sources*, **119-121**, 721 (2003).
129. C. J. Curtis, J. Wang, and D. L. Schulz, *J. Electrochem. Soc.*, **151**, A590 (2004).
130. A. M. Kannan and A. Manthiram, *Electrochem. Solid-State Lett.*, **5**, A167 (2002).
131. J. Cho, G. B. Kim, H. S. Lim, C. S. Kim, and S. I. Yoo, *Electrochem. Solid-State Lett.*, **2**, 607 (1999).
132. Y. K. Sun, K.-J. Hong, and J. Prakash, *J. Electrochem. Soc.*, **150**, A970 (2003).
133. S.-W. Lee, K.-S. Kim, H.-S. Moon, J.-P. Lee, H.-J. Kim, B.-W. Cho, W.-I. Cho, and J.-W. Park, *J. Power. Sources*, **130**, 227 (2004).
134. J.-S. Kim, C. S. Johnson, J. T. Vaughey, S. A. Hackney, K. A. Walz, W. A. Zeltner, M. A. Anderson, and M. M. Thackeray, *J. Electrochem. Soc.*, **151**, A1755 (2004).
135. P. Strobel, M. Anne, Y. Chabre, M. R. Palacín, L. Seguin, G. Vaughan, G. Amatucci, and J. M. Tarascon, *J. Power. Sources*, **81-82**, 458 (1999).
136. M. R. Palacín, F. Le Cras, L. Seguin, M. Anne, Y. Chabre, J. M. Tarascon, G. Amatucci, G. Vaughan, and P. Strobel, *J. Solid State Chem.*, **144**, 361 (1999).
137. G. G. Amatucci, N. Pereira, T. Zheng, I. Plitz, and J. M. Tarascon, *J. Power. Sources*, **81-82**, 39 (1999).
138. G. Amatucci, A. Du Pasquier, A. Blyr, T. Zheng, and J.-M. Tarascon, *Electrochim. Acta*, **45**, 255 (1999).

139. P. S. Whitfield and I. J. Davidson, *J. Electrochem. Soc.*, **147**, 4476 (2000).
140. G. G. Amatucci, N. Pereira, T. Zheng, and J.-M. Tarascon, *J. Electrochem. Soc.*, **148**, A171 (2001).
141. G. Amatucci and J.-M. Tarascon, *J. Electrochem. Soc.*, **149**, K31 (2002).
142. C. Wu, F. Wu, L. Chen, and X. Huang, *Solid State Ionics*, **152**, 327 (2002).
143. M. M. Doeff, J. Hollingsworth, J. Shim, Y. J. Lee, K. Striebel, J. A. Reimer, and E. J. Cairns, *J. Electrochem. Soc.*, **150**, A1060 (2003).
144. B.-L. He, S.-J. Bao, Y.-Y. Liang, W.-J. Zhou, H. Li, and H.-L. Li, S.-J. Bao, Y.-Y. Liang, W.-J. Zhou, B.-L. He, and H.-L. Li, *J. Solid State Chem.*, **178**, 897 (2005).
145. Y. J. Kang, J.-H. Kim, and Y.-K. Sun, *J. Power. Sources*, **146**, 237 (2005).
146. J.-M. Han, S.-T. Myung, and Y.-K. Sun, *J. Electrochem. Soc.*, **153**, A1290 (2006).
147. A. Du Pasquier, A. Blyr, P. Courjal, D. Larcher. G. Amatucci, B. Gerand, and J. M. Tarascon, *J. Electrochem. Soc.*, **146**, 428 (1999).
148. R. A. Young, A. Shakthivel, T. S. Moss, and C. O. P. Santos, *J. Appl. Crystallogr.* **28**, 366 (1995).
149. R. A. Young, *The Rietveld Method*, Oxford University Press, New York, (1993).
150. M. J. Katz, R. C. Clarke, and W. F. Nye, *Anal. Chem.*, **28**, 507 (1956).
151. G. Pistoia, A. Antonini, R. Rosati, and D. Zane, *Electrochim. Acta*, **41**, 2683 (1996).
152. A. Antonini, C. Bellitto, M. Pasquali, and G. Pistoia, *J. Electrochem. Soc.*, **145**, 2726 (1998).

153. J. M. Tarascon, F. Coowar, T. N. Bowmer, G. Amatucci, and D. Guyomard, *J. Electrochem. Soc.*, **141**, 1421 (1994).

154. X. Wang, H. Nakamura, and M. Yoshio, *J. Power Source*s, **110**, 19 (2002).

155. S. Choi, and A. Manthiram, *J. Electrochem. Soc.*, **149**, A1157 (2002).

156. T. A. Arunkumar, and A. Manthiram, *Electrochem. Solid-State Lett.*, **8**, A403 (2005).

157. W. Choi and A. Manthiram, *Electrochem. Solid-State Lett.*, **9**, A245 (2006).

158. W. Choi and A. Manthiram, *J. Electrochem. Soc.*, **153**, A1760 (2006).

159. B. D. Cullity, *Elements of X-ray Diffraction*, Addison-Wesley, New York (1978).

160. PNGV Battery Test Manual, Revision 3, DOE/ID-10597, February (2001).

161. Q. Wu, W. Lu, and J. Prakash, *J. Power Sources*, **88**, 237 (1999).

162. K. Amine, J. Liu, S. Kang, I. Belharouak, Y. Hyung, D. Vissers, G. Henriksen, *J. Power Sources*, **129**, 14 (2004).

163. J. Choi, E. Alvarez, T. A. Arunkumar, and A. Manthiram, *Electrochem. Solid-State Lett.* **9**, A241 (2006).

164. M. M. Thackeray, M. F. Mansuetto, D. W. Dees, and D. R. Vissers, *Mater. Res. Bull.*, **31**, 133 (1996).

165. T. Takada, H. Hayakawa, and E. Akiba, *J. Solid State Chem.*, **115**, 420 (1995).

166. Y. Gao and J. R. Dahn, *J. Electrochem. Soc.*, **143**, 1783 (1996).

167. M. M. Thackeray, M. F. Mansuetto, and C. S. Johnson, *J. Solid State Chem.*, **125**, 274 (1996).

VITA

Wonchang Choi was born as the eldest son of Kyu Suk Choi and Hye Sook Kim, on September 27, 1975, in Seoul, Republic of Korea. He earned his B.S. and M.S. degrees in Materials Science and Engineering from Korea University in Seoul, Republic of Korea, respectively, in August, 2000 and August, 2002. He worked at the Korea Institute of Science and Technology (KIST) as a research scientist from September, 2002 to June, 2003. He entered the graduate school of The University of Texas at Austin in August, 2003.

List of Publications:

1. Won Chang Choi, Dongjin Byun, Joong Kee Lee, Byung Won Cho, "Electrochemical Characteristics of silver- and nickel-coated synthetic graphite prepared by a gas suspension spray coating method for the anode of lithium secondary batteries," *Electrochimica Acta*, **50**, 2, 523 (2004).
2. W. Choi and A. Manthiram, "Superior Capacity Retention Spinel Oxyfluoride Cathodes for Lithium Ion Batteries," *Electrochemical and Solid State Letters*, **9**, A245 (2006).
3. W. Choi and A. Manthiram, "Comparison of Metal Ion Dissolution from Lithium Ion Battery Cathodes," *Journal of the Electrochemical Society*, **153**, A1760 (2006).
4. A. Manthiram, J. Choi, and W. Choi, "Factors limiting the electrochemical performance of oxide cathodes," *Solid State Ionics*, **177**, 2629 (2006).
5. W. Choi and A. Manthiram, "Influence of Fluorine on the Electrochemical Performance of Spinel $LiMn_{2-y-z}Li_yZn_zO_{4-\eta}F_\eta$ Cathodes," *Journal of the Electrochemical Society* (in press).

6. W. Choi and A. Manthiram, “Factors Controlling the Fluorine Content and the Electrochemical Performance of Spinel Oxyfluoride Cathodes,” *Journal of the Electrochemical Society* (submitted).
7. A. Manthiram and W. Choi, “Suppression of Mn Dissolution in Spinel Cathodes by Trapping the Protons within Layered Oxide Cathodes,” *Electrochemical and Solid State Letters* (submitted).
8. W. Choi and A. Manthiram, “Influence of Fluorine Substitution on the Electrochemical Performance of 3 V Spinel $Li_4Mn_5O_{12-\eta}F_\eta$ Cathodes” (in preparation).

Permanent address: 113-601 Chunggu Apt, Hansolmaul, Jungja Dong, Bundang-Gu, Seongnam-Si, Keongki-Do, Republic of Korea 134-032

This dissertation was typed by the author.